UNIVERSITY OF CALIFORNIA, MERCED

Photophysical Properties of Indium Phosphide Quantum Dots

A Dissertation submitted in partial satisfaction of the requirements
for the degree Doctor of Philosophy

in

Chemistry and Chemical Biology

by

Paul Cavanaugh

Dissertation Committee:

Professor Aurora Pribram-Jones, Chair
Professor Anne Myers Kelley, Advisor
Professor David F. Kelley, Advisor
Professor Tao Ye
Professor Jay Sharping

2023

Copyright page

The Dissertation of Paul Cavanaugh is approved, and it is acceptable in quality and form for publication on microfilm and electronically:

Professor Anne Myers Kelley

Professor David F. Kelley

Professor Jay Sharping

Professor Tao Ye

Professor Aurora Pribram-Jones Chair

University of California, Merced

Table of Contents

Acknowledgements

None of this work would have been possible without the continuous guidance and deep scientific understanding of Prof. David Kelley's and Prof. Anne Myers Kelley. They have proposed many interesting questions and clean experimental methods to address those questions. Both were always willing to discuss any question for as long as was needed for me to understand. In particular I am grateful for Anne Myers Kelley who gave me the second chance I needed to succeed in graduate school.

I would like to thank Ahn Nguyen and Haochen Sun who in their roles as post-doctoral researchers taught me so much about good experimental technique. They were both food mentors and good friends.

I would like to thank my collaborators Ilan Jen-La Plante, Christian Ippen, Xudong Wang, Maria Bautista, and Ruiqing Ma for their outstanding work synthesizing the particles that this study was based on. They have set a high bar for quality collaboration, and I hope that they would say the same of the us.

I would like to thank Arun Ashokan Fernanda Pilla Bardella Hlousk for their camaraderie and work ethic. While we have yet to publish anything together, I have no doubt your work will come to fruition.

I would like to thank my friends and family outside of UC Merced who have provided support for me over these last few years. They helped to make graduate school an enjoyable experience.

Finally, I would like to thank my fiancé Abigayle Dirdak for convincing me that I could in fact go to graduate school.

Curriculum Vitae

EDUCATION

Fresno State **2014-2018**
B.S. Chemistry *Fresno, CA*
- Minor in Physics

University of California Merced **2019-Present**
Ph.D. *Chemistry - In Progress (*expected completion fall 2023*)* *Merced, CA*
- P.I. - David F. Kelley and Anne Myers Kelley
- Completed Qualifying Exam
- Advanced to Candidacy August 2022

PUBLISHED PAPERS (In Order of Publication) Paul Cavanaugh - Google Scholar

1. **Resonance Raman Study of Shell Morphology in InP/ZnSe/ZnS Core/Shell/Shell Nanocrystals**
   Paul Cavanaugh, Ilan Jen-La Plante, Christian Ippen, Ruiqing Ma, David F. Kelley, and Anne Myers Kelley The Journal of Physical Chemistry C 2021 *125* (19), 10549-10557 DOI: 10.1021/acs.jpcc.1c02616
2. **Auger Dynamics in InP/ZnSe/ZnS Quantum Dots Having Pure and Doped Shells**
   Anh T. Nguyen, Paul Cavanaugh, Ilan Jen-La Plante, Christian Ippen, Ruiqing Ma, and David F. Kelley The Journal of Physical Chemistry C 2021 *125* (28), 15405-15414 DOI: 10.1021/acs.jpcc.1c03015
3. **Radiative dynamics and delayed emission in pure and doped InP/ZnSe/ZnS quantum dots**
   Paul Cavanaugh, Haochen Sun, Ilan Jen-La Plante, Maria J. Bautista, Christian Ippen, Ruiqing Ma, Anne Myers Kelley, and David F. Kelley J. Chem. Phys. 155, 244705 (2021) DOI: 10.1063/5.0077327
4. **Biexciton and Trion Dynamics in InP/ZnSe/ZnS Quantum Dots.**
   Haochen Sun, Paul Cavanaugh, Ilan Jen-La Plante, Christian Ippen, Maria Bautista, Ruiqing Ma, and David F. Kelley J. Chem. Phys. 156, 054703 (2022) DOI: 10.1063/5.0082223
5. **Reversible Interfacial Charge Transfer and Delayed Emission in InP/ZnSe/ZnS Quantum Dots with Hexadecanethiol.**
   Haochen Sun, Paul Cavanaugh, Ilan Jen-La Plante, Maria Bautista, Ruiqing Ma, and David F. Kelley The Journal of Physical Chemistry C 2022, *126*, 47, 20065–20073 DOI: 10.1021/acs.jpcc.2c06203
6. **Identity of the reversible hole traps in InP/ZnSe core/shell quantum dots**
   Anne Myers Kelley, Paul Cavanaugh, Haochen Sun, Xudong Wang, Maria Bautista, Ilan Jen-La Plante, Christian Ippen, and David F. Kelley J. Chem. Phys. 157, 174701 (2022) DOI: 10.1063/5.0123956

7. **Spectral Widths and Stokes Shifts in InP-based Quantum Dots**
   Paul Cavanaugh, Xudong Wang, Maria Bautista, Ilan Jen-La Plante, and David F. Kelley (In Print, Expected Fall 2023)

THESIS AND DISERTATION

- **Paul Cavanaugh.** Photophysical Properties of Indium Phosphide Quantum Dots, Ph. D. Dissertation (Fall 2023 Expected)

PRESENTATIONS GIVEN (In Order of Presentation)

1. **UC Merced Seminar 2022**
   Exploring Novel Photophysics in Indium Phosphide/Zinc Selenide Quantum Dots
   Paul Cavanaugh, Haochen Sun, Anh T. Nguyen, Ilan Jen-La Plante, Christian Ippen, Ruiqing Ma, David F. Kelley, and Anne Myers Kelley
2. **MRS Spring Meeting Spring 2023**
   The Dynamics of Reversible Hole Trapping in InP/ZnSe/ZnS Quantum Dots
   Paul Cavanaugh, Haochen Sun, Anh T. Nguyen, Ilan Jen-La Plante, Xudong Wang, Marie Bautista, Christian Ippen, Ruiqing Ma, Anne Myers Kelley, and David F. Kelley

INSTRUMENTAL TECHNIQUE PROFICIENCIES

- Time Correlated Photon Counting (TCPC/TRPL)
- Resonance Raman Spectroscopy
- Transient Absorbance Spectroscopy (TA)
- Photoluminescence Excitation Spectroscopy (PLE)
- Proton Nuclear Magnetic Resonance (Hnmr) Spectroscopy
- C-13 Nuclear Magnetic Resonance (Cnmr) Spectroscopy
- IR/UV-VIS Spectrometry
- Gas Chromatography
- Mass Spectrometry
- Experience working with samples in the 5-100 mg range
- Basic understanding of Python coding language

Honors and Awards

- CBC Summer Research Fellowship 2022
- CBC Graduate Research Excellence Award 2022
- CBC Travel Fellowship 2023

WORK EXPERIENCE

Walmart **June 2015 – 2018**
Electronics Sales Associate *Clovis, CA*

- Provided fast and friendly customer service.

- Register Trained
- Stocked freight.
- Reduced shrink.
- Retail experience in a variety of sales areas

DEMONSTRATION OF CAPABILITIES PERFORMED

EPA method 2320B

- Alkalinity determination (Metrohm 809 Titrando, 809 Dosino)

EPA method 2510B

- Conductivity determination (712 Conductometer, and the Titrando 809 Auto Sampler)

EPA method 4500HB

- PH determination (Metrohm 809 Titrando with Dosino 800 and Tiamo software)

EPA method 6010

- Analysis of total metals by Inductively Coupled Plasma Spectroscopy (Perkin Elmer Optima 4300DV/5300DV - Inductively coupled argon plasma emission spectrometer)

EPA method 7470A

- Analysis of mercury by cold vapor atomic absorption spectroscopy (Perkin-Elmer FIMS 400 mercury analyzer)

EPA method 8081

- Analysis of organochlorine pesticides by gas chromatography (Agilent 6890 gas chromatograph equipped with 7683A autosampler and Electron capture micro detector using environquant software for results)

EPA method 8260

- Analysis of volatile organic compounds by GC-MS MS (Agilent 7890A GC equipped with an Agilent 5975C Mass spectrometer detector)

EPA method 9056

- Analysis of inorganic anions by liquid chromatography using an ion exchange column (Dionex ICS-5000+ DC)

CERTIFICATIONS

- **Fundamentals for TAs in Higher Education** **2019**
  University of California, Merced Center for Engaged teaching and Learning
- **Mental Health First Aid** **2019**
  National Council for Behavioral Health

VOLUNTEER EXPERIENCE

Fresno Fencing Academy **December 2015- 2016**
Teacher and Coach *Fresno, CA*

- Taught students the basics of fencing
- Worked both in groups and one on one to make sure every student was successful.

Physics Outreach **January 2018- June 2018**

Student Teacher *Fresno, CA*

- Taught an introductory class for physics. The target audience was students ranging from first to sixth grade.
- Average class sizes ranged from 80 to 150 students
- Used demos and other teaching tools to relate physics to daily life.

Chem 106s (Service Learning) **August 2018- December 2018**

Student *Fresno, CA*

- Worked in an EPA certified lab using their SOPs
- Worked with lab grade instruments

List of Figures

Abstract of Dissertation

Title: Photophysical Properties of Indium Phosphide Quantum Dots
Name: Paul Cavanaugh
Degree: Doctor of Philosophy
Institution: University of California, Merced
Committee Chair: Aurora Pribram-Jones

Various semiconductor nanocrystals are currently being studied for their potential in optoelectronic devices such as photovoltaics, lasers, and lighting. Indium phosphide (InP) nanocrystals are particularly noteworthy due to their reduced toxicity and increased environmental sustainability as compared to other semiconductor nanocrystals. Indium phosphide nanocrystals are defect prone but can be passivated with a shell material such as zinc selenide (ZnSe) to mitigate this property and create stable highly luminescent QDs. Due to indium phosphide's relatively small band gap and the aforementioned stability, InP/ZnSe QDs can be used to make efficient green, red, and near IR emitters.

Chapter 1 of this work will begin with an exploration of the structure of indium phosphide zinc selenide quantum dots (QDs). The crystal and electronic structure of InP will be used to form a framework for the interpretation of the absorption and emission properties of InP/ZnSe QDs. This will be done by considering the existing literature on cadmium selenide (CdSe) QD nanocrystals. These two semiconductor nanocrystals share a zinc-blende crystal structure, and both have band structures with two degenerate valence bands at the band edge. In semiconductor QDs charge carriers can be described using an effective mass approximation determined by the curvature of these bands. This will lead to a discussion of envelope functions and fine structure states within those envelope functions. Finally, chapter 1 will include a shortened synthesis of three variations of InP/ZnSe nanoparticles that will be discussed in future chapters.

Using the framework created in Chapter 1, Chapter 2 will relate these envelope functions and fine structure states to the absorption and emission of the corresponding transitions. This interpretation will discuss the factors that contribute to the line widths of these particles and will introduce the concept of homogeneous and inhomogeneous distributions in ensemble measurements. This will be explored through the use of the photoluminescence excitation spectrum (PLE) and polarization resolved PLE. In order to fully explain the width of the excitation spectra it will be necessary to recognize and characterize two forms of inhomogeneous broadening, size inhomogeneity and interfacial inhomogeneity. This interfacial inhomogeneity leads to an inhomogeneity in the band offsets of InP and ZnSe which complicates the spectroscopy of these QDs.

Chapter 3 will introduce time resolved spectroscopies. Direct comparison with time resolved photoluminescence (TRPL) experiments with radiative lifetimes calculated using the Einstein relations will show that a thermal Boltzmann distribution between the non-emissive, and emissive states are required to relate the two values, as is predicted by

the fine structure discussed in chapter 1. Furthermore, the observed radiative lifetime varies across the emission band as predicted by the Einstein relations. This property can be used to determine the extent of aggregation in samples by looking at deviations in radiative lifetime due to Förster resonant energy transfer (FRET).

If during the shelling of InP/ZnSe QDs, the presence of indium is not carefully controlled, excess indium can become incorporated into the ZnSe shell. This leads to the formation of indium-based transient traps in the shell. Indeed, most published synthesis do not control for this variable, and thus these traps contribute significantly to the photoluminescent properties of published InP/ZnSe QDs. The indium-based shell transient traps are positioned between the valence band of the InP core, and the ZnSe shell valence band. This has the effect of trapping holes in the shell until they can tunnel into the valence band. Trapped holes have very small overlap with the electron wavefunction, and therefore do not contribute directly to the absorption or emission. Instead, they provide a reservoir state in thermal equilibrium with the emissive bright state, leading to delayed band edge emission. This increases the observed radiative lifetime by up to 30% for larger QDs. The equilibrium formed by process has a larger ratio of holes in the core to shell as opposed to the system short times after the cooling process, which has comparatively more holes in the shell.

In higher fluence conditions the InP/ZnSe QDs can absorb a second photon either simultaneously or sequentially. When this happens a biexciton forms. Biexcitons primarily recombine by Auger recombination. Auger recombination is when instead of a biexciton recombining radiatively, two carriers recombine and transfer their momentum to the two remaining carriers. This can create very high energy or “Hot” carriers. These hot carriers are of great interest because they are known to be able to perform chemical reactions that can lead to the degradation and quenching of photoluminescence in QDs. Minimizing or controlling these “hot” carriers is of utmost importance to increasing the stability of InP/ZnSe QDs at high fluences. Biexciton measurements can be measured in TRPL, but the increased time resolution of Transient Absorbance (TA) makes for easier and more accurate measurements. TRPL and TA biexciton measurements will be compared to extract information about the energetic position of the biexciton emitting state as compared to the single exciton emitting state.

As mentioned above, trapped holes exhibit minimal overlap with the electron wavefunction, and also interact weakly with the valence band. When two excitons are created if one of the holes cools into a trap state, it will be unable to efficiently undergo Auger recombination. This creates a pseudo-trion, where there are two electrons in the conduction band and a single hole in the valence band. The trapped hole, now held in a trap away from the core, induces an electric field across the QD that decreases the electron-hole interaction and slows the observed radiative lifetime compared to that of the analogous trion. This pseudo trion state that will be referred to as an XT state has an observed radiative lifetime that is a factor of four longer than the biexciton state, enabling precise determination of these rates through the comparison of both time-resolved photoluminescence (TRPL) and transient absorption (TA) measurements.

Chapter 4 will consider numerous possibilities regarding the chemical/structural identity of the indium-based transient traps. It will be shown that a zinc vacancy being charge compensated by a substitutional In^{3+} ion is the most likely candidate. Raman spectroscopy will be used to probe the structural characteristics of the QD and to elucidate the position of excess indium in the QD. This discussion on hole core equilibriums will be expanded to coupled thiols, which can function as hole acceptors, which can trap off holes for extended periods of time, up to hundreds of nanoseconds.

InP/ZnSe QDs hold great promise for the development of optoelectronic devices with enhanced environmental sustainability and reduced toxicity compared to other semiconductors. However, the presence of indium-based traps has significant implications for the photophysics and working lifetime of devices making use of InP/ZnSe QDs. Current literature on these particles is naïve to the contributions of these traps and the fingerprints of these traps can be seen in many key papers. This work, and the work it is based on, seeks to carefully disentangle the properties of the InP/ZnSe QD from those contributed by the traps in order to allow for accurate assignments.

Chapter 1. Introduction to Semiconductor Nanocrystals

1.1 Introduction

To make meaningful interpretations of complex spectroscopic measurements, it is essential to have a firm grasp of the underlying theory governing the photophysical processes. This chapter aims to elucidate how the photophysical processes within indium phosphide zinc selenide (InP/ZnSe) quantum dots (QDs) originate from the crystal structure and how they can be related to similar systems like cadmium selenide (CdSe). Additionally, it will introduce key characteristics of these QDs that will be explored throughout this work. For example, fine structure will be a focal point of discussion in all of the following chapters, as it plays a pivotal role in interpreting band edge processes within these QDs. This chapter will also include a simplified version of the synthesis of InP/ZnSe QDs. Small variations to this synthesis will be shown to have significant implications for the photophysics of these particles, and so the QDs in this study will have names reflecting their synthesis method.

1.2 Crystal and Electronic Structure of Indium Phosphide

Indium phosphide (InP) quantum dots (QDs) belong to the III-V semiconductors, named as such because they consist of elements from Group III (e.g., aluminum, gallium, and indium) and Group V (e.g., nitrogen, phosphorus, arsenic, and antimony) of the periodic table. The combination of different III-V semiconductors allows for the customization of their electronic and optical properties to suit specific applications. Indium phosphide is widely utilized in optoelectronic devices due to its capability to absorb and emit light across a broad range from infrared to visible wavelengths.

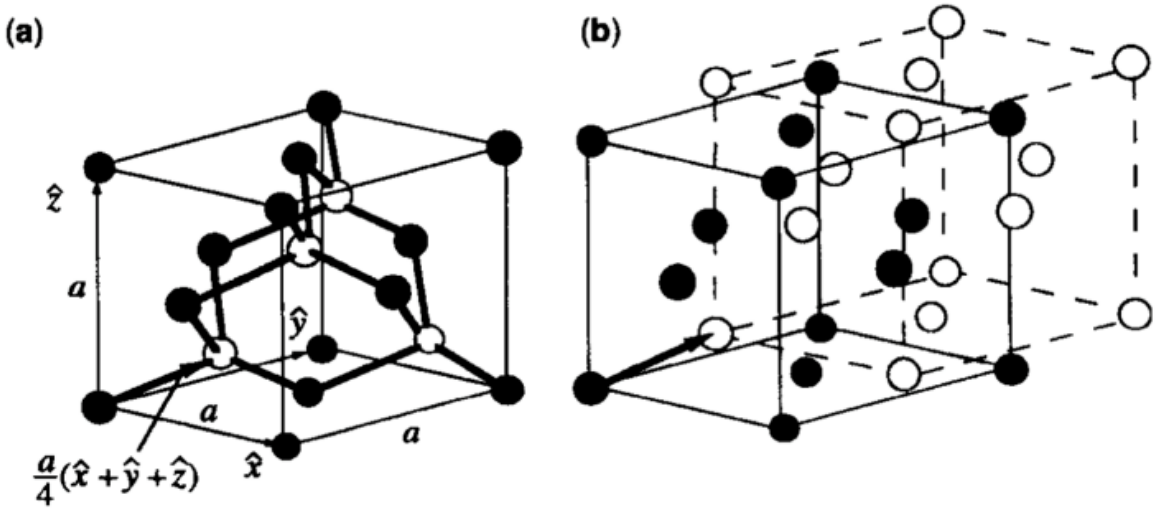

Figure 1.1: A) Zincblende crystal of the indium phosphide unit cell. B) Two interpenetrating face-centered-cubic lattices separated by the vector $(\frac{a}{4})(\hat{x}+\hat{y}+\hat{z})$, where a is the lattice constant.

Under standard temperature and pressure conditions, indium phosphide can exhibit two crystal structures: the thermodynamically favored zincblende crystal structure and the metastable wurtzite structure. However, the synthesis methods for wurtzite InP QDs are relatively new and not well-optimized. Consequently, this research will focus on quantum

dots with a zincblende crystal structure. In the zincblende structure, both the cation and anion occupy face-centered cubic arrangements, with each slightly offset from the other by the vector $(\frac{a}{4})(\hat{x}+\hat{y}+\hat{z})$, where a is the lattice constant as shown in figure 1.1.[1]

In InP, the lowest energy electronic transition is dominated by movement of an electron from the 2P orbital of the phosphorus anion to the 5s orbital of the indium cation[2]. This transition corresponds to a direct band gap minimum at the Γ point in the Brillouin zone of the crystal lattice, representing a wavevector with zero velocity. The band gap at this position is 1.35 eV, which corresponds to a bulk emission wavelength of approximately 900 nm.

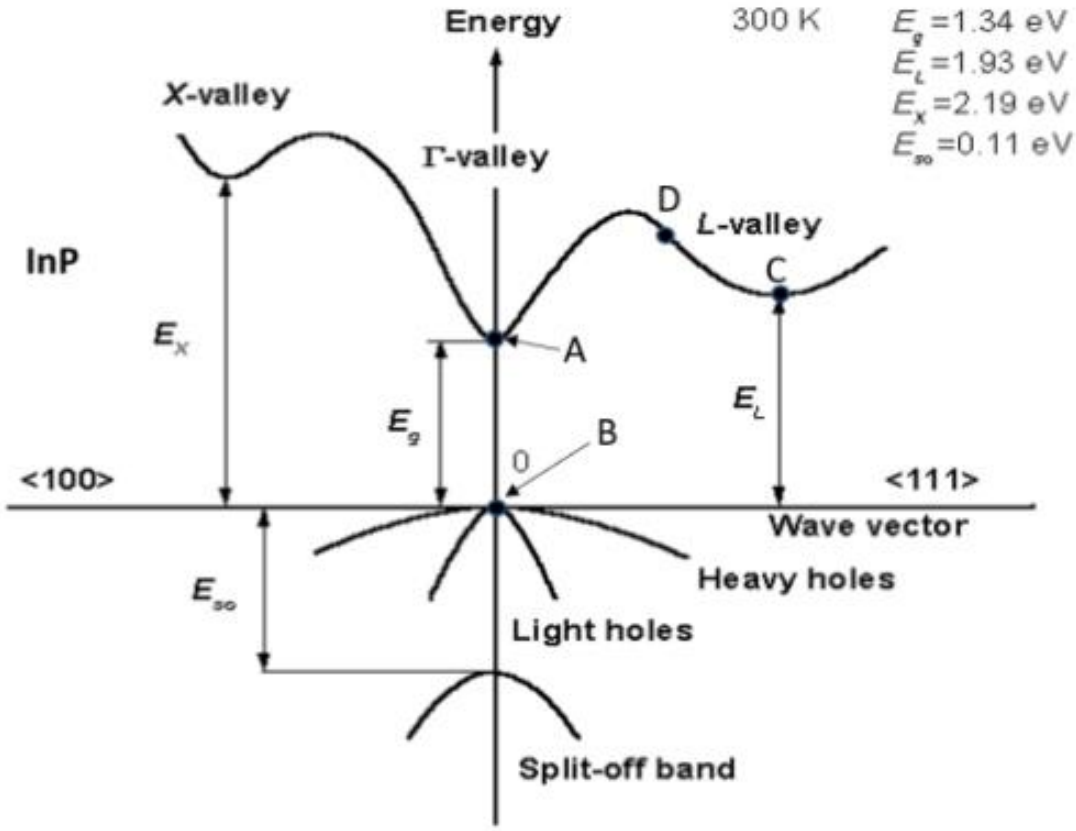

Figure 1.2: The band diagram of bulk InP showing the position of both the conduction band and the light hole, heavy hole, and split-off hole valence bands.[3] This plot has an x axis in terms of K, the wavevector, and a Y axis that is E(k) or the energy of a carrier with some wavevector.

The curvature near of the bands in a band structure diagram such as the one shown in figure 1.2 is interpreted using the Kronig-Penney model, which describes the motion of a charge carrier in a one-dimensional periodic potential.[1] This approximates the periodic potential experienced by a carrier as it moves across the crystal lattice in a specific direction defined by its wavevector. The Kronig-Penney model simplifies this potential by representing it as a periodic series of potential wells separated by potential barriers. This concept can be

expanded into more complex models such as the nearly-free electron model or the tight-binding model, which employ different potentials to better approximate specific crystalline systems. A solution to this system was found by Felix Bloch as shown in eq 1.1.[4]

$$\text{(Eq 1.1)} \quad \Psi_{(x)} = u_{(x)} e^{ikx}$$

This equation contains the free electron solution e^{ikx} modified by a function $u_{(x)}$which has the same periodicity as the crystal lattice. The wavevector k is described by the equation:

$$\text{(Eq 1.2)} \quad k^2 = \frac{2mE}{\hbar^2}$$

One of the conclusions of the Kronig-Penney model is that when we make use of the free electron wavefunction and a periodic lattice, the boundary conditions enforced by this periodicity creates regions of allowed and unallowed carrier energies called bands and band gaps respectively[1]. In order for an electronic transition to occur the ground state electron must be excited from its initial position in the valence band and end in a state with an allowed energy in the conduction band. The forbidden carrier energies between these levels cause a minimum transition energy that is dependent on the material referred to as that material's band gap.

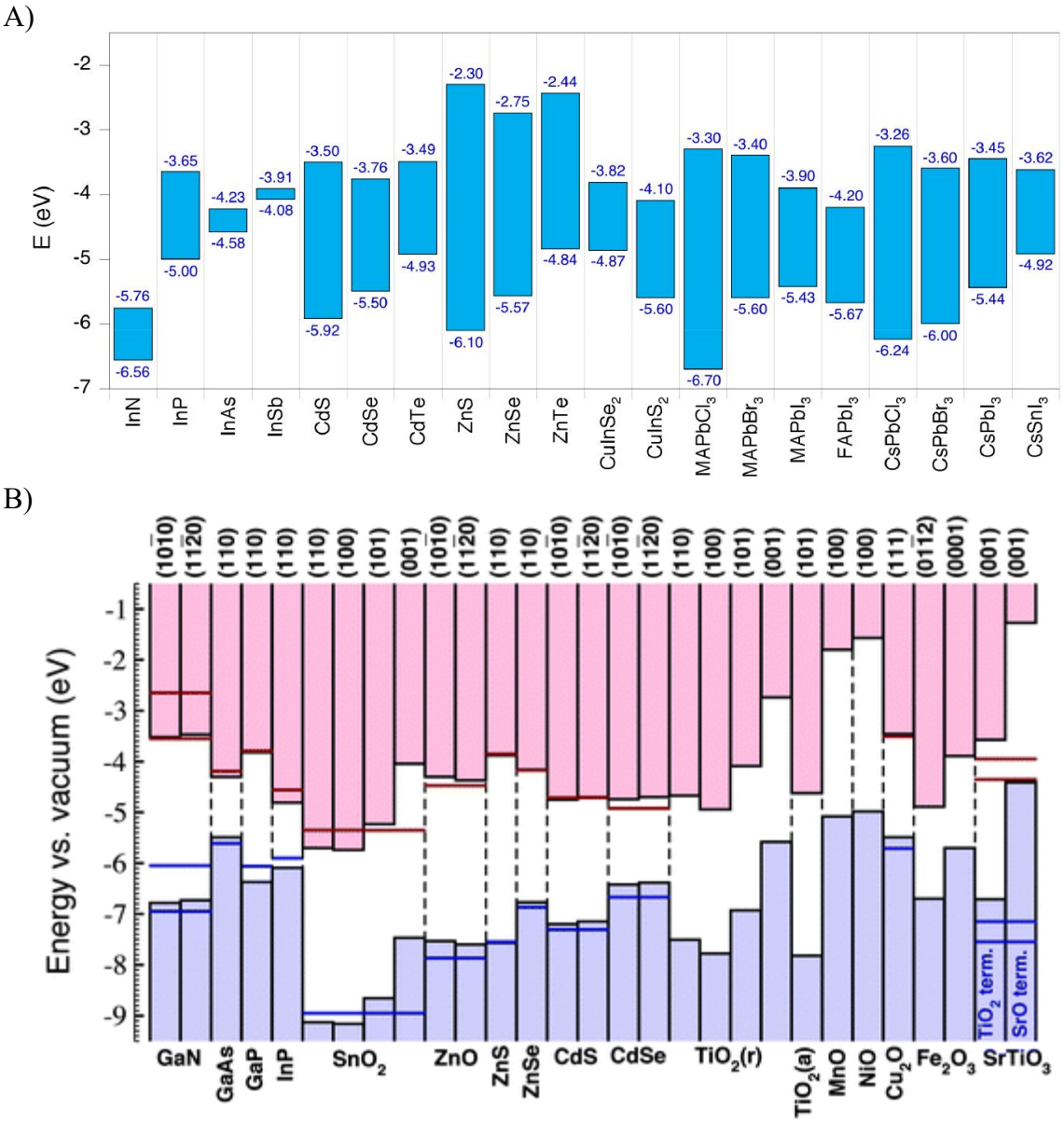

Figure 1.3: Example valence and conduction bands relative to "vaccum" for a number of II-VI and III-V semiconductors from A) Aldakov et al.[5] B) Stevanović et al.[6]

The band gap of a luminescent material can generally be approximated by observing the wavelength of the band edge emission, however determining the relative position of one material's band gap to another provides significant challenge.[5,6] Figure 1.3 shows that different groups find large differences in the offset relative to vacuum for the same materials. A naïve approach to determining these band offsets is to use the ionization energy of a material, or the energy required for a material to eject an electron from its valence band into the vacuum. This value represents the distance from the valence band to the vacuum level. The band gap can then be subtracted from the ionization energy to find the conduction band level. However, this naïve approach fails to account for the complexities of how these band positions shift in response to surface chemistry even in high vacuum conditions.

Characteristics like ligands, surface dipoles, pH, and even what crystal facet is being measured can shift the conduction and valence band levels by amounts greater than 2 eV. This means that finding the relative band offsets for a heterostructure such as InP/ZnSe can be difficult. Often the relative band offsets of a heterostructure cannot be easily measured and one must make assumptions based on the spectroscopic data available.

This interpretation is made more complex by the size of the nanocrystal. The Kronig-Penney model and the band offsets shown in figure 1.3 are both accurate only in the case where the crystal size is very large with respect to the carrier wavefunction, i.e., "bulk." This is certainly not the case in QDs, which by definition use small crystal volumes to confine the carriers. The relatively low number of atoms in these crystals, on the order of hundreds to thousands, makes treatment of QDs as large molecules a reasonable consideration. However, the technical difficulty of modeling that number of heavy atoms computationally is often prohibitively expensive. Towards that end effective mass models are used as a computationally cheap way of modeling the electronic structures of QDs.

1.3 Effective Masses and Envelope Functions

To gain insight into the spectroscopic properties of quantum dots (QDs), effective mass models are employed to provide a semiquantitative understanding. In the effective mass approximation, the mass of a carrier is described by the curvature of the band edge. In InP/ZnSe the band edge is at the Γ point. Near the Γ point these bands can be approximated to be parabolic and the effective mass of these carriers becomes a constant value unique to each band given by the relation:

$$\text{(Eq 1.3)} \qquad \frac{1}{m_{eff}} = \frac{1}{\hbar^2}\left(\frac{d^2E}{dk^2}\right)$$

As shown in figure 1.2, the valence band at the Γ point is split into the degenerate $J_{3/2}$ (light/heavy hole) bands and the $J_{1/2}$ (split-off hole) band, where the subscript stands for the total angular momentum J. This angular momentum J is the sum of the spin quantum number (m_s) and the orbital quantum number (m_l). The spin quantum is determined by the electron spin and can be either $\pm 1/2$. The orbital quantum number is determined by what atomic orbital the carrier resides in before the transition. For InP the band edge electron resides in an indium 5s ($m_l = 0$) orbital while the hole resides in a phosphorous 2p orbital ($m_l = \pm 1$). InP has relatively strong spin orbit coupling, and as such m_s and m_l are not conserved during transitions. Instead, the sum of the two values J is conserved. At wavevectors close to but not at the Γ point the $J_{3/2}$ band is further split into the $J_m = \pm 3/2$ and $J_m = \pm 1/2$ sub-bands where J_m is the projection of J in the Z direction.

The curvature of the conduction band in InP gives an electron mass of .073 m_o where m_o is the free electron mass. Alternatively, we can perform this same operation on the $J_m = \pm 3/2$ and $J_m = \pm 1/2$ valence sub-bands to get -.058m_o and -0.12m_o respectively.[4] This negative effective mass is referred to as the hole effective mass and represents the vacancy left behind by the electron transferring to the conduction band. This vacancy is modeled as a virtual particle to a great degree of success. The respective valence bands are therefore referred to as the heavy hole and light hole bands respectively, with the remaining

$J_{1/2}$ valence band being referred to as the split-off hole with a mass of -0.12m_o. Generally, as a convention the negative sign of the hole mass is dropped.

The effective mass of carriers can be utilized to determine an excitonic Bohr radius, which corresponds to the typical separation between an electron and a hole that are mutually attracted by Coulombic forces. This concept draws inspiration from atomic orbitals, where the Bohr radius represents the average distance between an electron and the nucleus. Similarly, the excitonic Bohr radius characterizes the average separation between an electron and a hole within their Coulombic attraction. The formation of this atom-like structure, comprising the bound electron-hole pair, is known as exciton. The equation for finding the Bohr radius of an atom is given by:

$$\text{(Eq 1.4)} \qquad a_0 = \frac{4\pi\varepsilon_0\hbar^2}{m_o e^2}$$

When eq 1.4 is solved for the hydrogen atom in a vacuum the excitonic Bohr radius a_0 is found to be .053 nm. In order to find the exciton Bohr radius in a material it is necessary to incorporate the reduced effective masses (μ_{eff}) of the charge carriers and the relative permittivity of the material (ε_r).

$$\text{(Eq 1.5)} \qquad a_x = \varepsilon_r \frac{m_o}{\mu_{eff}} a_0$$

The exciton Bohr radius of a material gives a scale for the confinement of an exciton. As the size of the material in which the exciton is confined moves from bulk towards the exciton Bohr radius the exciton is forced to occupy a smaller volume which leads to increased spacing between the allowed energy levels of the carriers. In a QD the exciton is confined within an approximately spherical volume, it can therefore be analogized to the "particle in a sphere" toy model. The solutions to the Schrödinger equation for a particle in a sphere are given by the spherical Bessel functions, along with the spherical harmonics, which form a set of orthogonal basis functions. In the context of the Schrödinger equation the spherical Bessel functions represent the probability amplitude distribution of a carrier, characterized by its effective mass within the QD. These spherical Bessel functions are denoted as $\alpha_{l,n}$ where l and n are the dual index roots. These roots describe a series of atomic-like orbitals referred to as the envelope functions as shown in figure 1.4.

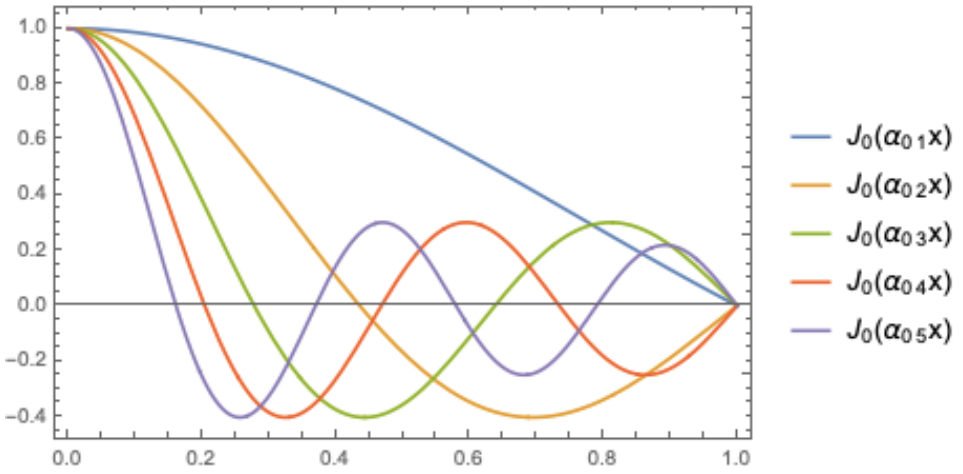

Figure 1.4: Example of a series of S like (l=0) envelope functions.

Electronic transitions in direct band gap semiconductors are referred to by the participating envelope function and by the carriers involved. For example, a transition that involves the 1S electron and the 1S heavy hole would be denoted as a $1S_e - 1S_{3/2}$ transition. A transition involving an electron and the split-off hole would be a $1S_e - 1S_{1/2}$ transition. In order for electron-hole recombination to occur the overlap of the wavefunctions of these two envelope functions must be nonzero. In cases where the boundary for both the electron and hole are in the same place (such as in the case of infinite potential wells) this leads to a series of selection rules as shown below.

$\Delta n = 0$: The radial quantum number (root indices n) must be equal.

$\Delta l = 0$: The wavefunctions must be of the same kind; S-S, P-P etc.

$\Delta m = 0$: The angular quantum number must be equal.

The energy of a given envelope function is given as eq 1.6 and the sum of the energy of the electron and hole envelope functions along with the band gap of the material give the energy of any given transition. A diagram of the relative position of these energy levels for both the electron and hole in a core only QD is shown in figure 1.5.

(Eq 1.6) $$E_{envelope} = \frac{\hbar^2 \alpha_{l,n}^2}{2m_{eff}a^2}$$

(Eq 1.7) $$E_{transition} = E_{BG} + E_{electron\ envelope} + E_{hole\ envelope}$$

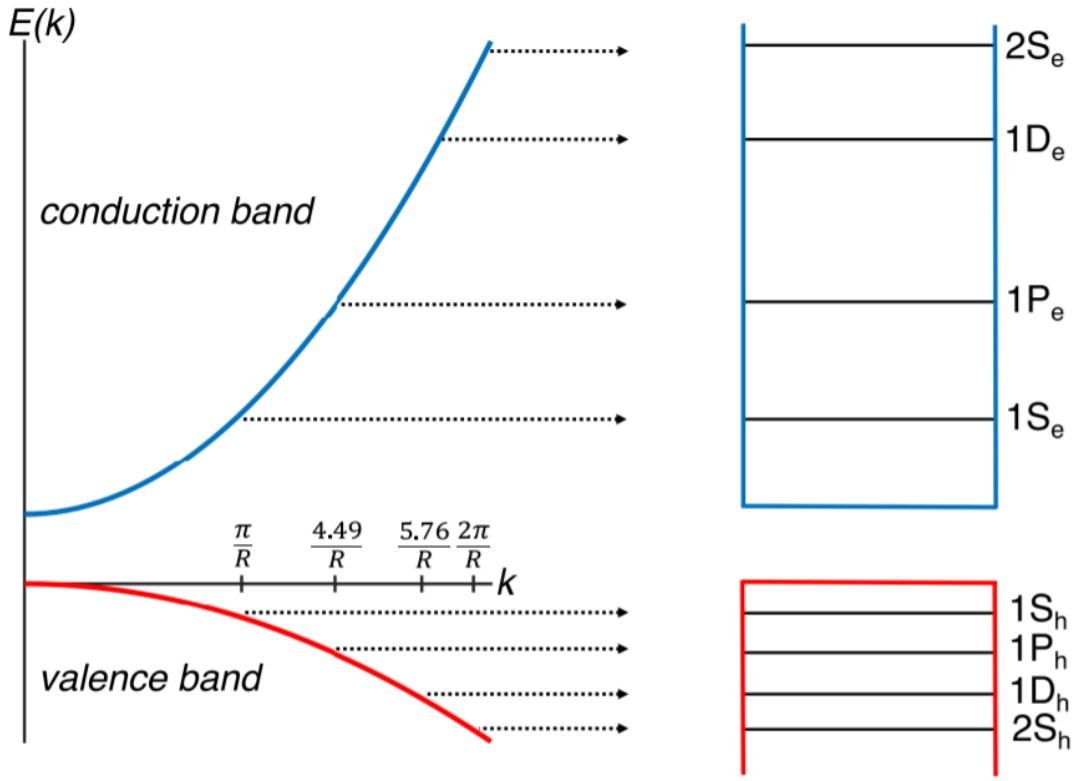

Figure 1.5: Set of electron and hole envelope functions determined by the curvature of their respective bands. The energy of a given transition is shown as the difference in energy between the two contributing states.

Nanocrystal structures are named for the ways in which the electron and hole wavefunctions are confined. By coating the core of a QD with a shell of another material it is possible to control the extent of confinement of the electron and hole independently. In a type-1 system both carriers are strongly confined to the core by a shell with both a higher energy valence and conduction band energy level. A type 2 structure has one carrier confined to the core, while the other carrier is confined mostly to the shell. In a quasi-type 2 or type 1.5 system one carrier is confined to the core while the other carrier is able to delocalize across both the core and shell. In practice the electron and hole are never exactly confined to the same volume, (even in nominally type 1 band offsets) and this relaxes the Δn restriction allowing for 1S-2S transitions. Additionally, real crystals may not be spherically symmetric and so the Δl restriction may not hold, allowing for the possibility of S-P transitions.

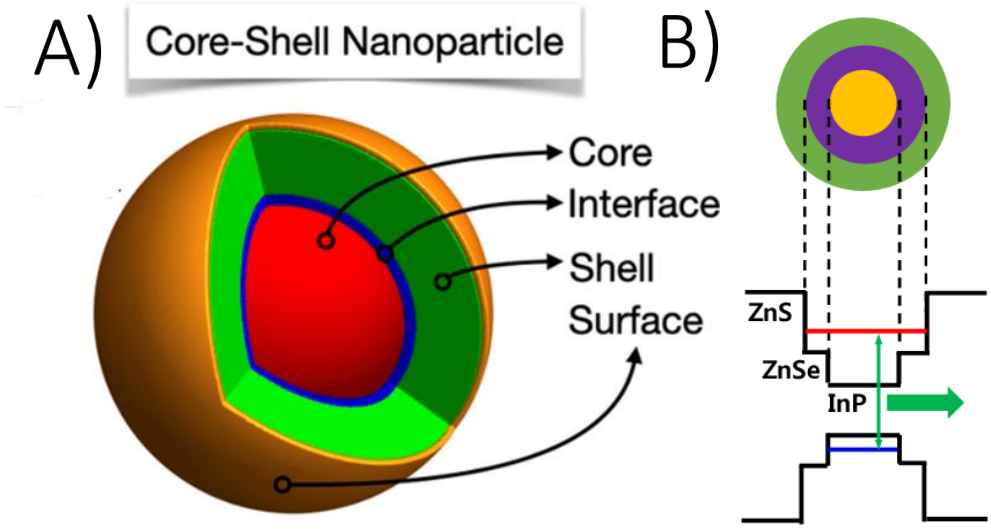

Figure 1.6: A) Example core/shell/shell QD structure showing key structural components. B) Diagram of how the bulk bandgap of the QD varies across a cross section of the QD (black) with calculated conduction band minimum after confinement (red) and calculated valence band minimum (blue) after confinement.

Based on the relative positions of the conduction and valence bands in InP and ZnSe it is possible to assign this as a type 1.5 structure. As shown in figure 1.6B the hole is strongly confined to the core while the conduction bands of the InP and ZnSe are close enough in energy to allow the electron to delocalize across both the core and shell. In later chapters it will be shown that the extent to which the electron delocalizes through the shell depends on the shell thickness, and that for particles with thicker shells the electron may not be fully delocalized.

1.4 Fine Structure

Section 1.3 built a framework of allowed envelope function transitions between two charged carriers, however due to the double degeneracy of the $1S_e$ state with respect to spin direction, and the fourfold degeneracy of the $1S_{3/2}$ (due to the degeneracy of the light and heavy hole, along with the spin direction degeneracy of both) the $1S_e - 1S_{3/2}$ transition is eightfold degenerate with respect to the projection of its total angular momentum. A theoretical analysis of the band-edge exciton structure in CdSe QDs was laid out by Efros et al. in 1996[7,8]. In CdSe the lowest split-off hole transition has a transition energy significantly above the band edge and is not considered. While the split-off hole is significantly closer to the band edge in InP, at only 110 meV separation, this simplification still works well for interpreting the band edge dynamics of InP QDs. Due to the similarities between the effective masses and band structure of zincblende CdSe and zincblende InP, the well understood fine structure of CdSe QDs can be used as a framework for understanding the fine structure of InP QDs. Chapter 2 will discuss the pitfalls of drawing direct comparisons between InP and CdSe, but the comparison is valuable for the discussion of band-edge fine structure.

The band-edge fine structure will become critically important to the emission of these QDs, as Kasha's rule holds true for QDs, and virtually all of the emission comes from the lowest allowed envelope function transition ($1S_e - 1S_{3/2}$). Therefore, the angular momentum fine structure states within the $1S_e - 1S_{3/2}$ envelope transition are the key to understanding the emission properties of these QDs. Efros et al. in 1996 calculated that the eightfold degenerate exciton predicted by the band gap diagram is split by the electron-hole exchange interaction and the shape anisotropy into five levels as shown in figure 1.7[7,8]. Two of the five states, including the lowest energy state, are dark, having nearly zero oscillator strength. The oscillator strength of the other three levels depends strongly on crystal size, shape, and electric field. The relative ordering of the energy levels is also heavily influenced by these parameters. These energy levels are named for the projection of their total angular momentum onto the Z axis.

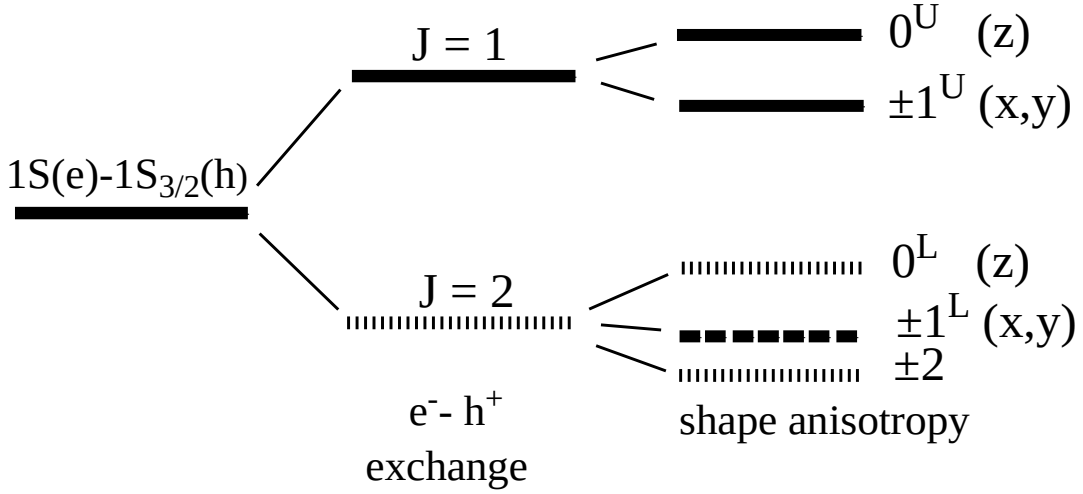

Figure 1.7: Fine structure levels of the $1S_e - 1S_{3/2}$ envelope function with the corresponding polarizations under the experimentally supported assumption of a slightly oblate geometry.[7–10]

In a perfectly spherical zincblende particle with no shape anisotropy, the ±2, $\pm1^L$ and 0^L states are degenerate and have no oscillator strength. The higher energy 0^U and $\pm1^U$ states are also degenerate and taken together, form an isotropic oscillator. The energetic separation between the upper (singlet) and lower (triplet) states is determined by the electron-hole exchange interaction. The fine structure becomes more complicated when spherical symmetry is broken.[11] In the case of slightly oblate or prolate ($D_{\infty h}$) particles, the exchange interaction leads to different orderings of the angular momentum fine structure states. The anisotropy breaks the degeneracies of the ±2 and $\pm1^L$ states and mixes the $\pm1^U$ and $\pm1^L$ states. As a result, the experimentally observed lowest (weakly) allowed transition is a planar, x,y polarized oscillator and some of the x,y oscillator strength is lost from the upper states. Further symmetry reduction (to C_{2v} or lower) breaks the x,y degeneracy and can result in the lowest allowed transition being linearly polarized.[11]

Temperature dependent studies on InP QDs indicate that the lowest excited state is only very weakly allowed, and most room temperature emission comes from thermal population of a slightly higher energy partially allowed state. Consistent with these assignments, Brodu et al. also assign the lowest energy dark and bright states to the ±2 and $\pm1^{L}$ states, respectively.[12] The energy separation of these states has been shown to be on the order of 5 – 10 meV and increases with decreasing particle size. Time-resolved Photoluminescence (TRPL) studies show that there is a strongly allowed excited state well above the emitting bright state. This bright-bright splitting increases from 40 to 147 meV as the particle size is decreased from 3.3 to 2.4 nm. The strongly allowed upper allowed states can be assigned to the $\pm1^{U}$, 0^{U} states, as discussed by Efros et al.[1] All the above results can be understood in terms of an energy level scheme in which the lowest state is dark, there is a weakly allowed state at slightly higher energy and strongly allowed states at considerably higher energy.

1.5 Colloidal Synthesis

Previous sections have developed the theory behind the structure of InP/ZnSe QDs, however a core goal of this work is connecting synthetic controls to the electronic properties of these QDs. This section will cover the most simplified description of a colloidal synthesis of InP cores and the shelling of InP/ZnSe/ZnS core/shell/shell particles. These syntheses were performed by collaborators at Nanosys Inc.[13–20] While the core and shell synthesis shown here is based on work by Peng et al, some syntheses use additional treatment and purification steps.[21]

For a typical InP core synthesis $In(acetate)_3$ is reacted with tri(octyl)phosphine and/or tri(methylsilyl)phosphine in octadecene (ODE) at ~270 °C. When the desirable particle sizes are reached, the reaction is stopped by removing from heat. Without any further surface treatments, InP cores are defect prone and tend to have very low QY. In order to passivate defects a ZnSe shell is grown over the InP core. ZnSe is chosen for its significantly higher energy valence band and because the lattice parameter, the side length of the unit cell, is a close match. Zincblende structures of InP and ZnSe have a ~3% lattice mismatch, facilitating epitaxy of ZnSe shells onto InP cores. When undergoing shelling, the InP core QDs synthesized using the above procedure were maintained at 270 °C then after the addition of $Zn(myristate)_2$ and a Se suspension in ODE they are heated to 300 °C. With a relatively small lattice mismatch of 5% between ZnSe and ZnS, an additional thin ZnS shell can be epitaxially grown onto the InP/ZnSe core/shell QDs to improve chemical stability of the QDs. This is done by adding sulfur-ODE at 300 °C.

The overall indium-to-phosphorous ratio of these QDs is of particular interest and has been determined through inductively coupled plasma (ICP) elemental analysis. This analysis gives complete In/P/Zn/Se/S elemental ratios. Particle dimensions (core size and shell thicknesses) are determined through a combination of the elemental analysis results and core size determinations from calculations based on known sizing curves.[22] This gives core diameters and shell thicknesses that are consistent with both the absorption spectra and the elemental ratios. The determination tacitly assumes that the P/Se and P/S elemental ratios give the core-to-ZnSe and core-to-ZnS volume ratios (ignoring the differences in molar volumes), essentially assuming that there is no phosphorous in the shells. The overall particle diameters calculated this way agree with sizes determined by transmission electron

microscopy (TEM) imaging as shown in figure 1.8, within the uncertainties of the measurements.

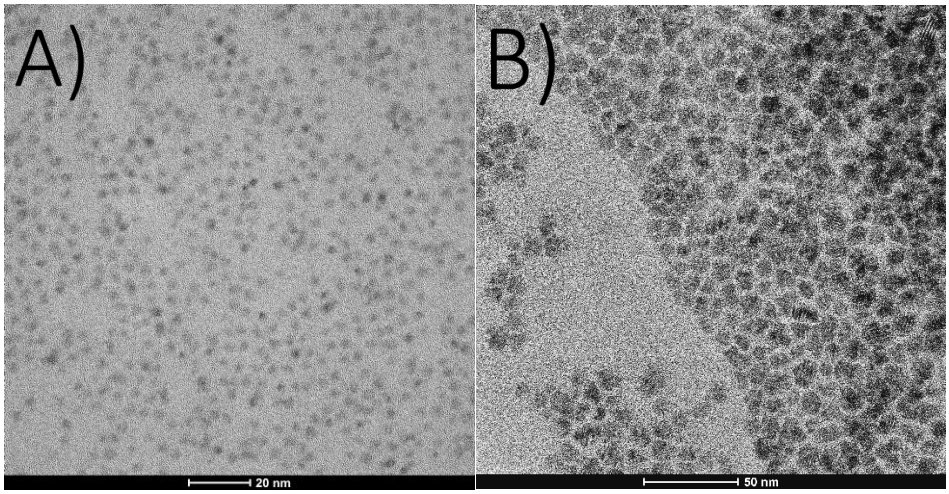

Figure 1.8: Transmission electron microscopy images of A) InP cores B) InP/ZnSe/ZnS core shell particles.

The indium-to-phosphorous ratio measured by ICP gives rise to another synthetic handle. In the synthesis provided above, if no steps are taken to remove the excess indium used in the synthesis of the core before shelling, then the resulting particles will be synthesized with an overall indium-to-phosphorous ratio that ranges from 1.4 to 2.0. These samples with uncontrolled indium content are referred to as nonstoichiometric particles and are abbreviated as NSx.xx where x.xx is the shell thickness of the particle being studied. In addition to nonstoichiometric particles this work will look at two more types QDs with further levels of purification. The second set are referred to as core derivatized, CDx.xx. These particles undergo an additional step after core synthesis in which they are exposed to an excess of zinc oleate, which creates a monolayer of zinc coating the core. This decreases the amount of excess indium that is incorporated into the QD during shelling, generally leading to a 1.05-1.4 indium-to-phosphorus ratio. Finally there are stoichiometric particles, Sx.xx. These particles undergo the most significant purification. They are exposed to excess zinc oleate after core synthesis to create a zinc monolayer to protect the InP core, after which they are precipitated and then redispersed in a solution for shelling without the presence of leftover indium precursor. When this purification is performed, the indium-to-phosphorous ratio is much closer to stoichiometric, typically .99-1.05. This agreement further establishes the core/shell morphology of these particles and indicates that they are not extensively alloyed.

1.6 Conclusions

This chapter has created a framework by which the electronic characteristics of an indium phosphide quantum dot can be reasonably interpreted based on the electronic and structural properties of the materials involved. This includes a description of the way in which the band gap of the material is dependent on the size of the nanocrystal, allowing for the tunability of emission across the visible range. In addition, the fine structure of these quantum dots will be

key to the interpretation of their band edge dynamics. Importantly it showed that the lowest fine structure level, ±2, is entirely dark and that at room temperature all emission comes from the faintly allowed $\pm 1^L$ state which is x,y polarized. In addition, this chapter has classified InP/ZnSe/ZnS quantum dots into three categories: nonstoichiometric, core derivatized, and stoichiometric, each characterized by different ratios of indium to phosphorus and distinct interfacial treatments. This framework is poised to serve as a valuable tool for the analysis and interpretation of experimental data when complex trapping mechanisms are introduced in later chapters.

1.7 **References**

(1) Kuno, M. *Introductory Nanoscience*; Garland Science, 2011. https://doi.org/10.1201/9780429258442.

(2) Dümbgen, K. C.; Zito, J.; Infante, I.; Hens, Z. Shape, Electronic Structure, and Trap States in Indium Phosphide Quantum Dots. *Chemistry of Materials* **2021**, *33* (17), 6885–6896. https://doi.org/10.1021/acs.chemmater.1c01795.

(3) Orlenko, E.; Orlenko, F. Magnetic Ordering in Systems of Identical Particles with an Arbitrary Spin. *Chemosensors* **2019**, *7* (4), 54. https://doi.org/10.3390/chemosensors7040054.

(4) Yu, P. Y.; Cardona, M. *Fundamentals of Semiconductors*; Springer Berlin Heidelberg: Berlin, Heidelberg, 2010. https://doi.org/10.1007/978-3-642-00710-1.

(5) Aldakov, D.; Reiss, P. Safer-by-Design Fluorescent Nanocrystals: Metal Halide Perovskites vs Semiconductor Quantum Dots. *The Journal of Physical Chemistry C* **2019**, *123* (20), 12527–12541. https://doi.org/10.1021/acs.jpcc.8b12228.

(6) Stevanović, V.; Lany, S.; Ginley, D. S.; Tumas, W.; Zunger, A. Assessing Capability of Semiconductors to Split Water Using Ionization Potentials and Electron Affinities Only. *Physical Chemistry Chemical Physics* **2014**, *16* (8), 3706. https://doi.org/10.1039/c3cp54589j.

(7) Efros, A. L.; Rosen, M.; Kuno, M.; Nirmal, M.; Norris, D. J.; Bawendi, M. *Band-Edge Exciton in Quantum Dots of Semiconductors with a Degenerate Valence Band: Dark and Bright Exciton States*; 1996.

(8) Sercel, P. C.; Efros, A. L. Band-Edge Exciton in CdSe and Other II-VI and III-V Compound Semiconductor Nanocrystals - Revisited. *Nano Letters*. American Chemical Society July 11, 2018, pp 4061–4068. https://doi.org/10.1021/acs.nanolett.8b01980.

(9) Rodina, A. V.; Efros, A. L. Band-Edge Biexciton in Nanocrystals of Semiconductors with a Degenerate Valence Band. *Phys Rev B Condens Matter Mater Phys* **2010**, *82* (12). https://doi.org/10.1103/PhysRevB.82.125324.

(10) Shabaev, A.; Rodina, A. V.; Efros, Al. L. Fine Structure of the Band-Edge Excitons and Trions in CdSe/CdS Core/Shell Nanocrystals. *Phys Rev B* **2012**, *86* (20), 205311. https://doi.org/10.1103/PhysRevB.86.205311.

(11) Sercel, P. C.; Shabaev, A.; Efros, A. L. Photoluminescence Enhancement through Symmetry Breaking Induced by Defects in Nanocrystals. *Nano Lett* **2017**, *17* (8), 4820–4830. https://doi.org/10.1021/acs.nanolett.7b01662.

(12) Brodu, A.; Ballottin, M. V.; Buhot, J.; van Harten, E. J.; Dupont, D.; La Porta, A.; Prins, P. T.; Tessier, M. D.; Versteegh, M. A. M.; Zwiller, V.; Bals, S.; Hens, Z.; Rabouw, F. T.; Christianen, P. C. M.; de Mello Donega, C.; Vanmaekelbergh, D. Exciton Fine Structure and Lattice Dynamics in InP/ZnSe Core/Shell Quantum Dots. *ACS Photonics* **2018**, *5* (8), 3353–3362. https://doi.org/10.1021/acsphotonics.8b00615.

(13) Kelley, A. M.; Cavanaugh, P.; Sun, H.; Wang, X.; Bautista, M. J.; Jen-La Plante, I.; Ippen, C.; Kelley, D. F. Identity of the Reversible Hole Traps in InP/ZnSe Core/Shell Quantum Dots. *J Chem Phys* **2022**, *157* (17), 174701. https://doi.org/10.1063/5.0123956.

(14) Sun, H.; Cavanaugh, P.; Jen-La Plante, I.; Bautista, M. J.; Ma, R.; Kelley, D. F. Reversible Interfacial Charge Transfer and Delayed Emission in InP/ZnSe/ZnS Quantum Dots with Hexadecanethiol. *The Journal of Physical Chemistry C* **2022**, *126* (47), 20065–20073. https://doi.org/10.1021/acs.jpcc.2c06203.

(15) Nguyen, A. T.; Cavanaugh, P.; Plante, I. J.-L.; Ippen, C.; Ma, R.; Kelley, D. F. Auger Dynamics in InP/ZnSe/ZnS Quantum Dots Having Pure and Doped Shells. *The Journal of Physical Chemistry C* **2021**, *125* (28), 15405–15414. https://doi.org/10.1021/acs.jpcc.1c03015.

(16) Cavanaugh, P.; Sun, H.; Jen-La Plante, I.; Bautista, M. J.; Ippen, C.; Ma, R.; Kelley, A. M.; Kelley, D. F. Radiative Dynamics and Delayed Emission in Pure and Doped InP/ZnSe/ZnS Quantum Dots. *J Chem Phys* **2021**, *155* (24). https://doi.org/10.1063/5.0077327.

(17) Sun, H.; Cavanaugh, P.; Jen-La Plante, I.; Ippen, C.; Bautista, M.; Ma, R.; Kelley, D. F. Biexciton and Trion Dynamics in InP/ZnSe/ZnS Quantum Dots. *J Chem Phys* **2022**, *156* (5), 054703. https://doi.org/10.1063/5.0082223.

(18) Cavanaugh, P.; Jen-La Plante, I.; Ippen, C.; Ma, R.; Kelley, D. F.; Kelley, A. M. Resonance Raman Study of Shell Morphology in InP/ZnSe/ZnS Core/Shell/Shell Nanocrystals. *The Journal of Physical Chemistry C* **2021**, *125* (19), 10549–10557. https://doi.org/10.1021/acs.jpcc.1c02616.

(19) Sun, H.; Cavanaugh, P.; Jen-La Plante, I.; Bautista, M. J.; Ma, R.; Kelley, D. F. Reversible Interfacial Charge Transfer and Delayed Emission in InP/ZnSe/ZnS Quantum Dots with Hexadecanethiol. *The Journal of Physical Chemistry C* **2022**, *126* (47), 20065–20073. https://doi.org/10.1021/acs.jpcc.2c06203.

(20) Cavanaugh, P.; Wang, X.; Bautista, M. J.; Jen-La Plante, I.; Kelley, D. F. Spectral Widths and Stokes Shifts in InP-Based Quantum Dots. *J Chem Phys* **2023**, *159* (13). https://doi.org/10.1063/5.0165956.

(21) Li, Y.; Hou, X.; Dai, X.; Yao, Z.; Lv, L.; Jin, Y.; Peng, X. Stoichiometry-Controlled InP-Based Quantum Dots: Synthesis, Photoluminescence, and Electroluminescence. *J Am Chem Soc* **2019**, *141* (16), 6448–6452. https://doi.org/10.1021/jacs.8b12908.

(22) Lange, H.; Kelley, D. F. Spectroscopic Effects of Lattice Strain in InP/ZnSe and InP/ZnS Nanocrystals. *The Journal of Physical Chemistry C* **2020**, *124* (41), 22839–22844. https://doi.org/10.1021/acs.jpcc.0c07145.

Chapter 2. Causes of Absorbance Congestion, Photoluminescence Width, and Stokes Shift in Indium Phosphide Zinc Selenide QDs.

2.1 Introduction

Chapter 1 identified the allowed electronic transitions in quantum dots. This chapter will focus on relating these electronic transitions to ensemble observables that will determine their efficacy in device applications. InP QDs are primarily intended for use in optoelectronic devices, and therefore characteristics such as the wavelength of light emitted and the color clarity of QD ensembles is of great interest. For photoluminescence down converting QDs (QDs intended to be excited at a blue wavelength and then emit at a target wavelength for use in a display or for lighting) the relationship between absorption cross section and emission wavelength is of great importance. This chapter will identify ways in which both the absorption and emission spectra of these QDs are complicated by considerations that don't significantly contribute to the features of their cadmium-based counterparts. Specifically, it will identify strong dipoles at the core-shell interface which make large contributions to the absorbance and photoluminescence widths that are unique to the InP/ZnSe spectra. It will also show that these considerations allow for the interpretation of the Stokes shift, absorption congestion, and emission width of InP using the same theoretical framework that is used for their cadmium-based counterparts and that was discussed in the previous chapter.

2.2 Congested Absorbance and Broad Photoluminescence Spectra

A comparison of the absorption spectra of core only InP QDs and other types of core only QDs such as CdSe or CdTe (cadmium telluride) shows a significant difference in the extent of congestion in the absorption spectrum as shown in figure 2.1. CdSe and CdTe QDs have multiple peaks in the absorption spectrum that can be assigned using the envelope functions laid out in chapter 1. Some of the congestion in these spectra can be assigned to the contribution of transitions involving the split-off hole. The split-off hole envelope function transitions similar to their spin 3/2 counterparts but are shifted to higher energies by the spin orbit splitting of their valence band (Δ_o). This Δ_o has values in the bulk of 110 meV for InP, 920 meV for CdTe, and 430 meV for CdSe[1–3]. The separation of the spin 3/2 and 1/2 valence bands in QDs varies slightly from the bulk Δ_o, but it gives a rough approximation of the expected contribution of the split-off hole states to the absorbance spectrum. This accounts for some of the differences in the absorption spectra of core only QDs, however when a shell is placed on CdSe or CdTe there is only a small change in the congestion of their absorbance spectra. When a shell is put on an InP core as shown in figure 2.1D, it becomes virtually impossible to identify the energetic position of any specific transition above the $1S_e - 1S_{3/2}$.

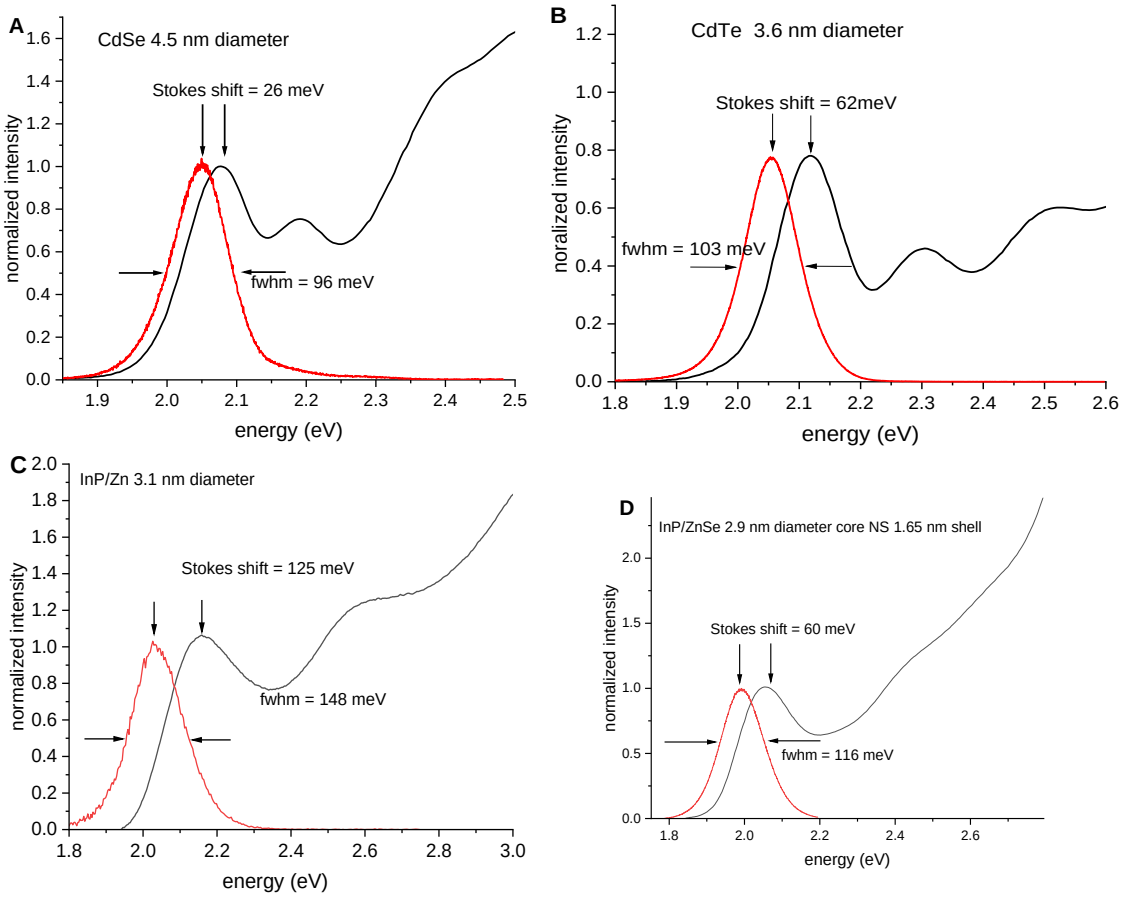

Figure 2.1: Absorption (black) and emission (red) spectra with Stokes shift and FWHM of the emission labelled for A) CdSe core of 4.5 nm diameter. B) CdTe core of 3.6 nm diameter. C) InP core of 3.1 nm (coated with a zinc monolayer to allow for measurable luminescence). D) InP/ZnSe nonstoichiometric core shell particle with 2.9 nm core and 1.65 nm shell.

The interpretation of this congested absorption spectrum is difficult without an understanding of the mechanisms that lead to the broadness of these transitions. As such we must take the time to examine the literature on what features contribute to the ensemble linewidths such as those shown in figure 2.1. As discussed in chapter 1 each allowed transition between carrier envelope functions has a set of fine structure states. In addition to the fine structure states, there are a number of vibrationally excited states that make up the phonon progressions. The contributions of the phonon progressions are apparent in low-temperature single particle emission spectra and allow determination of the phonon energies.[4] There is often a high density of phonon states that are not individually resolved. Their presence shifts the absorption maximum to higher energies and the PL maximum to lower energies, compared to the zero-phonon line.

The acoustically broadened zero-phonon line of the $\pm 1^{L}$ of the $1S_e - 1S_{3/2}$ transition has been reported at temperatures ranging from 4 to 220 kelvin in single particle photoluminescence studies.[4] It has been shown to have a FWHM that varies from 5 meV to 30 meV over that range. Comparing the single particle and ensemble PL measurements there is a significant difference in the observed FWHM. This difference in width is usually assigned to inhomogeneous distributions, or distributions in the structural properties of individual QDs within the ensemble. For QDs this is generally referenced in terms of size distributions. QDs in an ensemble have slight variance in size, and therefore a difference in the confinement energies and emission wavelength. This variance in emission wavelength leads to broadening in the ensemble measurement and is observed to be very close to Gaussian. When two Gaussian functions are convolved, (such as the homogeneous and inhomogeneous linewidths) the resulting function is also a Gaussian. The width of the resulting Gaussian depends on the widths of the two original Gaussian functions being convolved. The convolution of two Gaussian functions with standard deviations (widths) σ1 and σ2 results in a Gaussian function with a standard deviation (width) given by:

$$\text{(Eq 2.1)} \qquad \sigma_{convolved} = \sqrt{\sigma_1^2 + \sigma_2^2}$$

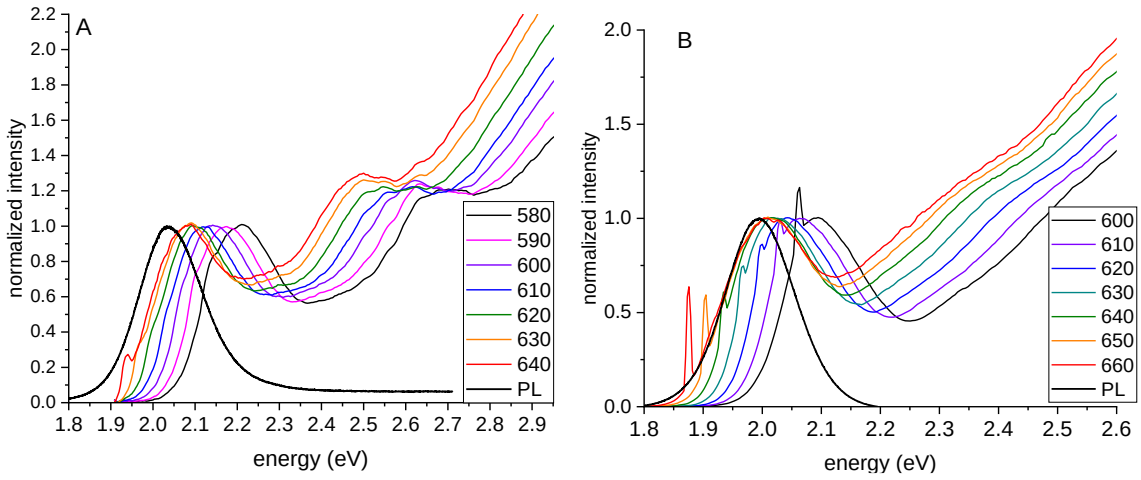

Figure 2.2: A) PLE of zinc treated, 3.1 nm diameter InP core particles B) PLE spectra of CD-2.28 InP/ZnSe/ZnS QDs with the detection window at several different wavelengths across the PL band. At the observation wavelength there is a sharp peak corresponding to the scattered excitation beam.

In order to determine the width of inhomogeneous broadening a photoluminescence excitation spectrum (PLE) can be performed where the PL intensity at a specific detection energy is measured as a function of excitation energy. The nature of a PLE spectrum is that by choosing a specific detection energy one can select a narrow slice (within the homogeneous width) of the inhomogeneously broadened population. As such, the PLE spectra should be relatively narrow, having widths determined by the homogeneous broadening in both the absorption and PL spectra. Importantly, if size inhomogeneity is the dominant form of inhomogeneous broadening, then the PLE spectra obtained at different detection wavelengths should be very similar, differing only slightly with the change in confinement energy associated with emission at that wavelength as is seen in the cores shown in figure 2.2A. As figure 2.2B shows, this is not observed in InP/ZnSe.

Instead, there is a significant change in the linewidths at the different observation wavelengths, and the spacing between the $1S_{3/2}$-$1S_e$ absorption and emission peaks changes in a way impossible to interpret with size inhomogeneity alone. Size inhomogeneity would predict a linear relationship between the detection window and the absorption peak with a slope that is very near to 1, instead InP/ZnSe QDs have a slope that is nearly half that, as shown in figure 2.3.

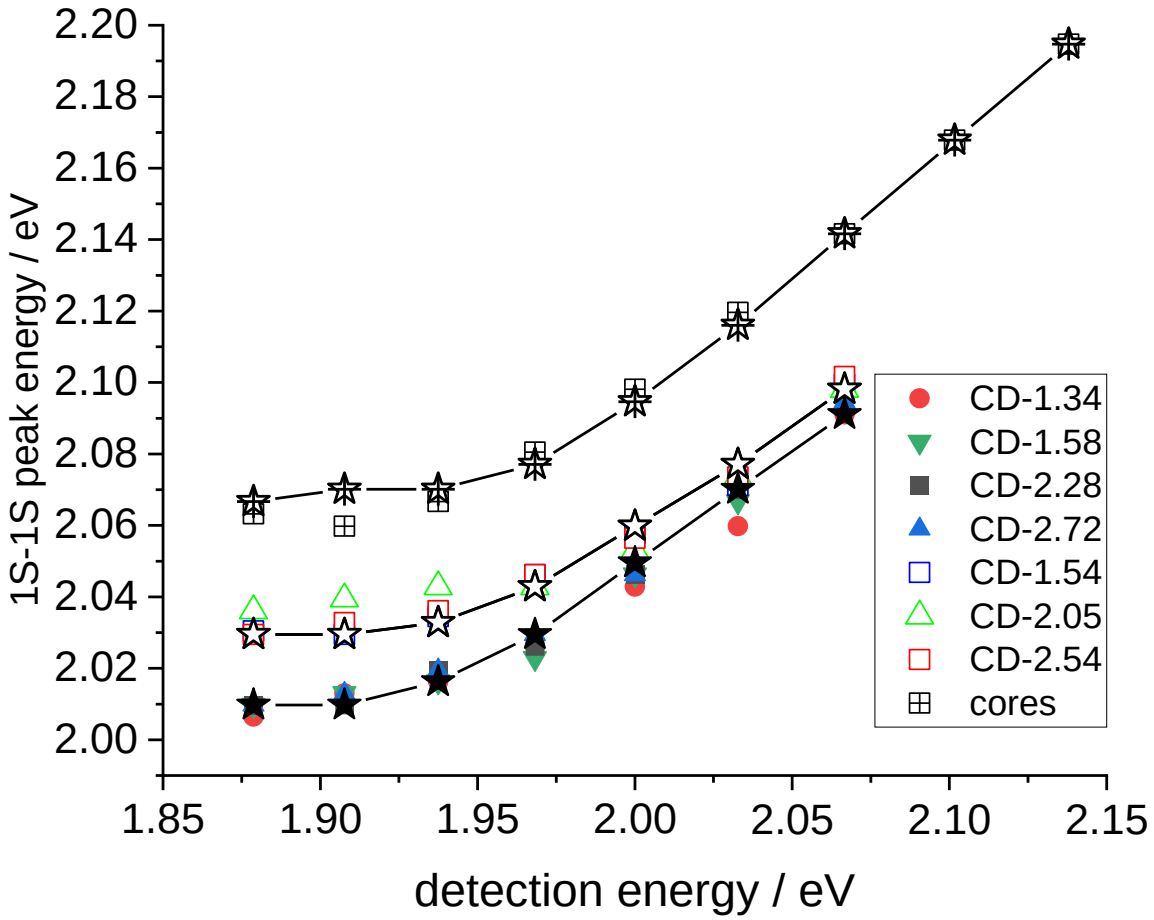

Figure 2.3: Plot of the observed PLE 1S-1S peak energy as a function of the detection energy for zinc treated InP core QDs and for core-derivatized QDs. The CD-1.54, CD-2.05 and CD-2.54 particles have 2.76 nm cores; the others have 2.9 nm cores. Also shown are calculated curves (stars connected by lines) based on the model presented later in figure 2.5, as will be discussed in the text.

To achieve the required QY to obtain accurately measurable photoluminescence, InP cores need to undergo passivation. This passivation process involves treating them with zinc oleate, resulting in the formation of a zinc monolayer coating on the QDs. The zinc monolayer has minimal effects on the position of the absorption and emission of the QD. In the PLE experiments conducted on these passivated InP cores, shown in figure 2.2A, it is observed that the energy difference between the $1S_{3/2}$-$1S_e$ and 1P-1P transitions is larger in the higher detection energy PLE spectra. Additionally, the ratios of the $1S_{3/2}$-$1S_e$ and 1P-1P quantum confinement energies (i.e., transition energies minus the bulk bandgap energy) are nearly constant, approximately 1.55 in all cases. For a simple particle-in-a-sphere model, the ratio of 1P and 1S energies is represented by the ratio of the first zeros of the spherical Bessel functions, $j_1(\alpha_{11})/j_0(\alpha_{01})$, which is numerically 1.43.[1] This experimental value of 1.55 is in reasonable agreement with the expected value for a core-only particle, as it would be for a simple particle-in-a-sphere. TEM images taken of the InP cores in figure 2.2A were used to

measure the size distribution and it was found to be 3.1 ± 0.3 nm. (For TEM images see S.I.) By comparing the calculated exciton energies of 2.8 and 3.4 nm InP particles, the width of the inhomogeneous energy distribution due to size can be determined. This calculated width is found to be slightly larger than the total observed inhomogeneous width of 138 meV. This leads to the conclusion that within the measurement uncertainty of the TEM sizing, the dispersion in the cores corresponds to the entire observed energy dispersion.

However, the spectroscopy of InP/ZnSe QDs cannot be explained by a simple combination of homogeneous and inhomogeneous size broadening. This is seen from an examination of the PLE spectra of the InP/ZnSe QDs in figure 2.2B. Deposition of a ZnSe shell makes the exciton energy much less sensitive to core size dispersion than the case of the InP core-only particles. This is due to reduced electron quantum confinement in the core-shell particles. Otherwise stated, the ratio of how the exciton energy changes with core size, dE_x/dr_{core}, varies with the extent to which the electron is delocalized into the shell and therefore with the ZnSe shell thickness. The effective mass approximation calculations described in reference[5] can be used to compare these red-emitting InP/ZnSe/ZnS QDs having 2.5 nm thick ZnSe shells with their initial cores and a calculated ratio of the derivatives dE_x/dr_{core} of 0.64 is obtained. This allows estimation of the size inhomogeneity in the core/shell/shell particles. If we take the core size dispersion in the core-derivatized particles to be the same as that measured for the above core-only particles, then following shell growth, this corresponds to a size inhomogeneity of 0.64 x 138 meV = 88 meV in the final core/shell/shell QDs. When this calculated size inhomogeneity is convolved with the single particle line widths at room temperature as found in reference[4] it does not account for the observed ensemble emission linewidth.

We suggest that the widths of the $1S_{3/2}$-$1S_e$ absorption, and PL peaks can be understood in terms of two types of inhomogeneity: size inhomogeneity and core/shell interface inhomogeneity. Later we will show that this core/shell interface inhomogeneity also allows for the interpretation of the Stokes shift and conjested absorbance in the PLE. Size inhomogeneity affects the spectra in the well-understood way as discussed above: larger particles have less quantum confinement and therefore have lower energy optical transitions. The mechanism by which the nature of the core-shell interface affects the spectroscopy is through an electrostatic interaction produced by the core-shell interfacial dipole. The core facets in InP/ZnSe QDs are either In or P terminated, and there are core-shell dipoles associated with In-Se and with P-Zn interfacial bonding. Depending on the relative number of In-Se and P-Zn interfacial bonds, the net electric dipole can point either away from or toward the InP core. We further note that an InP core having both types of interfacial dipoles can produce internal electric fields that may break the inversion symmetry. A relaxation of inversion symmetry could cause transitions that would be forbidden in particles that are otherwise nearly spherically symmetric to have some oscillator strength.

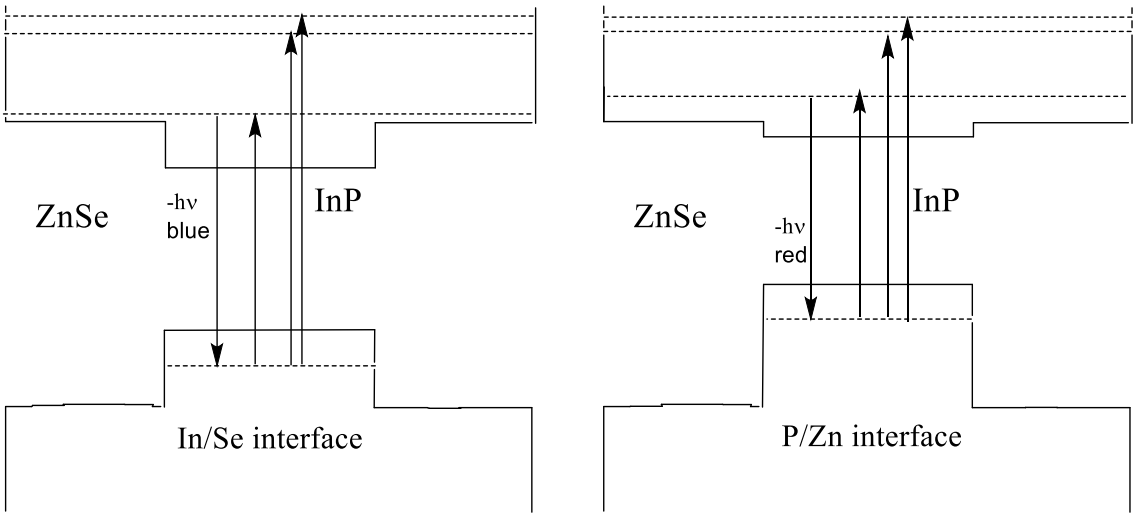

Figure 2.4: Schematic of the quantum confined energy levels of a QD with two different types of core/shell interfaces in InP/ZnSe particles.

These interfacial dipoles can be understood in terms of relative electronegativities: selenium has a larger electronegativity than phosphorous (2.55 compared to 2.19) and zinc has a slightly smaller electronegativity than indium (1.65 compared to 1.78).[6] In the case of an indium terminated core surface, the presence of an In-Se bond gives the indium a more positive charge than one that is only bonded to phosphorus. Thus, the presence of In-Se bonding at the core-shell interface will result in a dipole pointing away from the core. Alternatively stated, the presence of In-Se interfacial bonds results in an InP core that is net positively charged, shifting the core conduction and valence bands further from the vacuum level. The opposite occurs with P-Zn bonds at the core-shell interface. We note that the larger electronegativity differences and hence the larger dipoles are expected with In-Se bonding. The relative number of In-Se versus P-Zn interfacial bonds determines the magnitudes of the band offset shifts. This ratio can vary from one particle to another, giving rise to band offset inhomogeneity. We suggest that this is a significant source of spectral inhomogeneity in the case of InP/ZnSe core/shell QDs.

Band offset inhomogeneity can have dramatic effects on the exciton energy because the quantum confinement energies of the electrons and holes change by different amounts in response to changes of the InP core conduction and valence band potentials. This is because of differences in the spatial extents of the electron and hole wavefunctions. Holes have large effective masses and there is a large offset to the ZnSe valence band.[1] They are therefore well localized to the core, and their energies closely follow the InP valence band potential. Electrons have small effective masses and a small potential offset to the ZnSe conduction band. They are therefore more delocalized into the ZnSe shell, and their energies vary less than the hole energies with changes in the core potential. EMA calculations, as described in reference[7] indicate that small changes in the core potential can result in significant changes in

the exciton energy. Specifically, we calculate that raising the core potential by 50 meV lowers the exciton energy by about 30 meV.

We note that the energetic effects of a core-shell dipole are analogous to the effects of surface dipoles associated with polar ligands on single-component nanoparticles.[8–18] Such dipoles can shift the conduction and valence bands by several hundred meV, and shifts approaching these magnitudes are expected from dipoles at core-shell interfaces. The extent to which this occurs is determined by the relative amounts of In and P termination on an individual core with the spectroscopic and energetic effects of the net interfacial dipoles indicated schematically in figure 2.4. The effect of core-shell interfacial dipoles and their effect on the spectroscopy of InP/ZnSe QDs has recently been reported and analyzed in terms of some of the same considerations shown in figure 2.4.[6]

In the context of these energetic considerations, we can consider the assignment of the continuum absorption seen in the PLE spectra at 200 – 700 meV above the $1S_{3/2}$-$1S_e$ peak. The intensity of this absorption also depends on the composition of the reaction mixture used for the first layer of ZnSe shell deposition, and hence the nature of the core-shell interface as shown in figure 2.5B. We find that the presence of excess indium during the initial shell deposition decreases the amount of the high energy continuum absorption, consistent with the mechanism in figure 2.4.

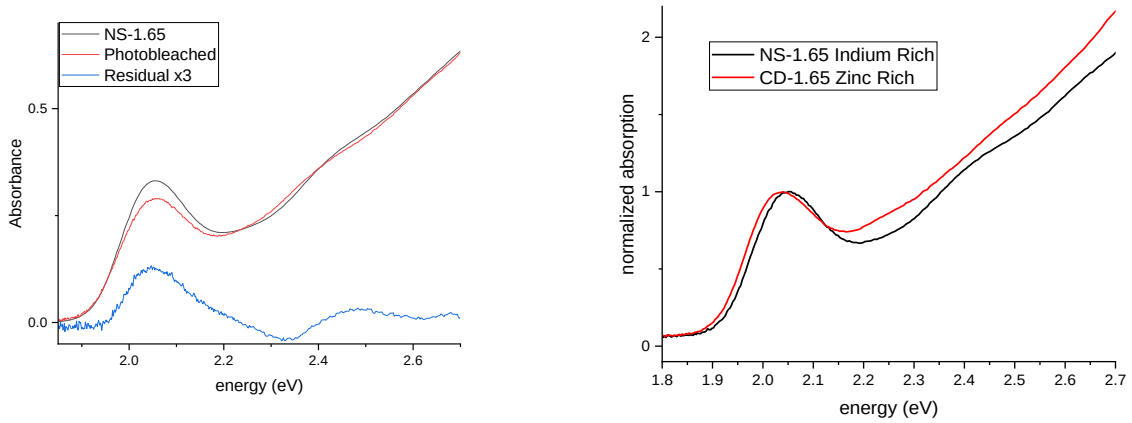

Figure 2.5: A) Photobleaching by lithium borohydride of NS-1.65 with a residual that shows the position of the $1S_{3/2}$-$1S_e$ and $1S_{1/2}$-$1S_e$ transitions. B) Comparison of the absorbance spectrum of NS-1.65 which has an indium-selenium rich interface, with CD-1.65 which has a comparitively phosphorous-zinc rich interace. Both are normalized to the first exciton peak.

The evaluation of this assignment involves an analysis of figure 2.5A, which presents a photoreduction spectra. This assignment focuses on the $1S_{3/2}$-$1S_e$ and $1S_{1/2}$-$1S_e$ transitions which are both bleached when an electron is introduced to the 1Se state through photopbleaching, while higher-energy transitions remains mostly unaffected. The experimental setup involves titrating a quantum dot (QD) sample with small quantities of lithium borohydride. When a QD is excited through photon absorption, lithium borohydride has the capability to donate an electron into the valence band hole created by the excitation, thereby leaving an electron in the conduction band and negatively charging the QD. This

process leads to the partial filling of the 1Se state, which, in turn, results in a decrease in intensity of all transitions that involve the placement of an electron in this state.

We also note that in a transient absorbance spectrum the bleach following low power excitation is also due to partial filling of the conduction band $1S_e$ state.[19] Consistent with the photobleaching results, previously reported TA spectra show that exciton formation results in the same lack of bleaching above the $1S_{1/2}$-$1S_e$ transition.[5,20] These considerations indicate that the transition producing the continuum absorption cannot involve the $1S_e$ state and it must be assigned to transitions to higher energy conduction band states.

This understanding finally allows assignment of the cause of the comparative congestion of the absorption spectrum in InP/ZnSe QDs when compared to other semiconductor QDs. It is a combination of the small Δ_o of InP, and the interfacial dipole mechanism. The first leads to a greater number of states in the observed range, while the second leads to a distribution in the position of these states relative to the $1S_e - 1S_{3/2}$ transition (as shown in figure 2.4) causing a large broadening of these higher energy states. Additionally, the interfacial dipole mechanism contributes a new mechanism of inhomogeneous broadening to the PL. However, the lack of observed $1S_e - 1P$ transitions in the photobleached and TA spectra suggests that this inhomogeneity does not lead to a significant deviation from inversion symmetry.

2.3 Stokes Shift

For a complete modeling of the PLE data presented in figures 2.2 and 2.3 in the previous section it is important to address the Stokes shift. The Stokes shift in CdSe and CdTe have both been successfully interpreted using a combination of fine structure and phonon progressions. However there have recently been questions as to the efficacy of this assignment for InP/ZnSe QDs. The spectroscopy of InP nanocrystals that are either unpassivated, passivated by HF etching or by deposition of a ZnS shell have been reported by Janke et al.[21] Large Stokes shifts are seen in InP nanocrystals passivated by either method, and they conclude that this is due to radiative recombination of a conduction band electron and a hole trapped at crystal defects or at zinc dopants in the InP core. This assignment of the Stokes shift is very different than an assignment to phonon progressions and angular momentum fine structure. If the Stokes shifted PL were due to the recombination of a trapped hole with a conduction band electron, the polarization of the emitting oscillator would randomly oriented, and the luminescence would be unpolarized.

This section will examine the polarized and unpolarized PL and PLE spectra of very high quality InP/ZnSe/ZnS particles as a function of InP core size and ZnSe shell thickness. We also examine core only InP particles which are surface passivated by adsorbed zinc ions. These results are compared with results obtained for CdSe, CdTe and CdSe/CdS core/shell particles. In all cases, the results can successfully be interpreted in terms of the angular momentum fine structure, phonon progressions, size inhomogeneity and inhomogeneities brought about by the nature of the core-shell interface.

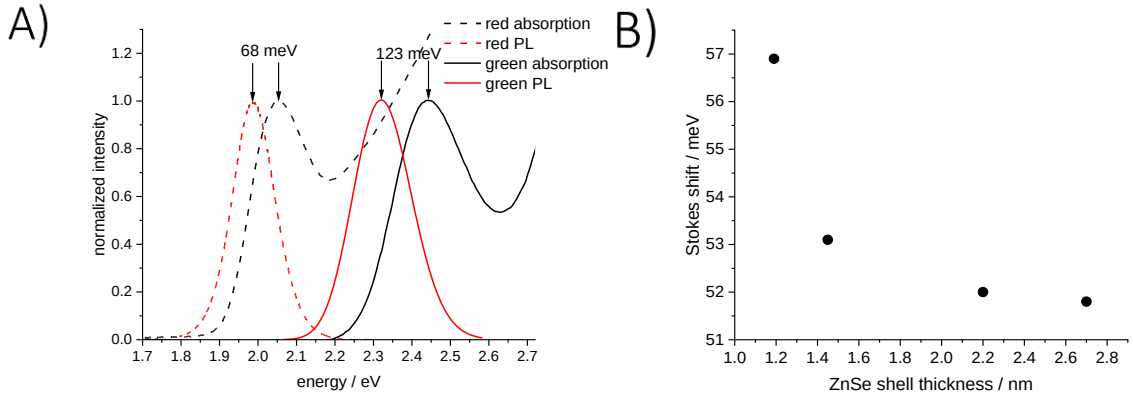

Figure 2.6: A) Size dependent absorption and PL spectra for red (2.9 nm core) and green (1.45 nm core) emitting InP/ZnSe/ZnS particles showing the large effect of changes in core size with similar overall volume. B) Dependence of the Stokes shift on shell thickness for a series of InP/ZnSe/ZnS QDs having identical 2.9 nm InP cores showing a smaller but measurable effect.

In quantum dots, the Stokes shift of the band edge emission originates from two causes: phonon progressions and angular momentum fine structure. The role of angular momentum fine structure in the Stokes shift has been described in a series of papers by Efros et al.[22–25] The energetic separation between the upper (singlet) and lower (triplet) states is determined in large part by the electron-hole exchange interaction as was shown in figure 1.7. The electron-hole exchange interaction predicts that the Stokes shift should scale inversely to the size of the particle as demonstrated in figure 2.2A and should scale inversely to shell thickness as shown in figure 2.2B. This is because the electron hole exchange interaction is coulombic, and scales with the inverse of the average distance between the carriers. A smaller particle decreases the average distance between carriers, while a shell increases the volume accessible to the electron increasing their average distance.

It is noteworthy that as additional layers of ZnSe are added to the shell of the quantum dot in figure 2.2B, the Stokes shift decreases by approximately 10%. However, after adding 1.8 nm of shell, the Stokes shift levels off, showing little further change. A similar change in behavior at 1.8 nm will be observed again in chapter 3 when calculating the photon cross-section of the $1S_{3/2}$-$1S_e$ transition. This suggests that at the point where 1.8 nm of ZnSe shell has been added, the effect of further electron delocalization becomes minimal, leading to the stabilization of the Stokes shift and absorption characteristics.

PLE experiments can be polarization resolved to get further insight into the fine structure states at the band edge. In this experiment, the excitation light is vertically polarized and photo-selects those QDs having their absorption oscillators aligned with the polarization of the light. Both horizontally and vertically polarized detection signals are measured giving the relative orientation of the emitting oscillator. The excitation wavelength dependent

anisotropies are defined in eq 2.2 where I_{par} (I_{perp}) is the PL intensity when the detection polarization is parallel (perpendicular) to the excitation polarization.

$$\text{(Eq 2.2)} \qquad r = \frac{I_{par} - I_{perp}}{I_{par} + 2I_{perp}},$$

For any specified excitation and detection energies, the measured anisotropy depends on the relative orientations of the absorbing and emitting oscillators. A few limiting cases are of particular interest. When the absorbing and emitting oscillators have the same polarizations, a positive anisotropy is obtained. Specifically, r = 0.4 when the absorbing and emitting oscillators are colinear, and r = 0.1 when the oscillators are coplanar or when either oscillator is planar, and the other linear oscillator is in that plane. When the absorbing and emitting oscillators are perpendicular, a negative anisotropy is obtained, r = -0.2. With these limiting cases, it is possible to qualitatively analyze the anisotropy spectra in figure 2.7 in terms of the polarizations indicated in figure 1.7.

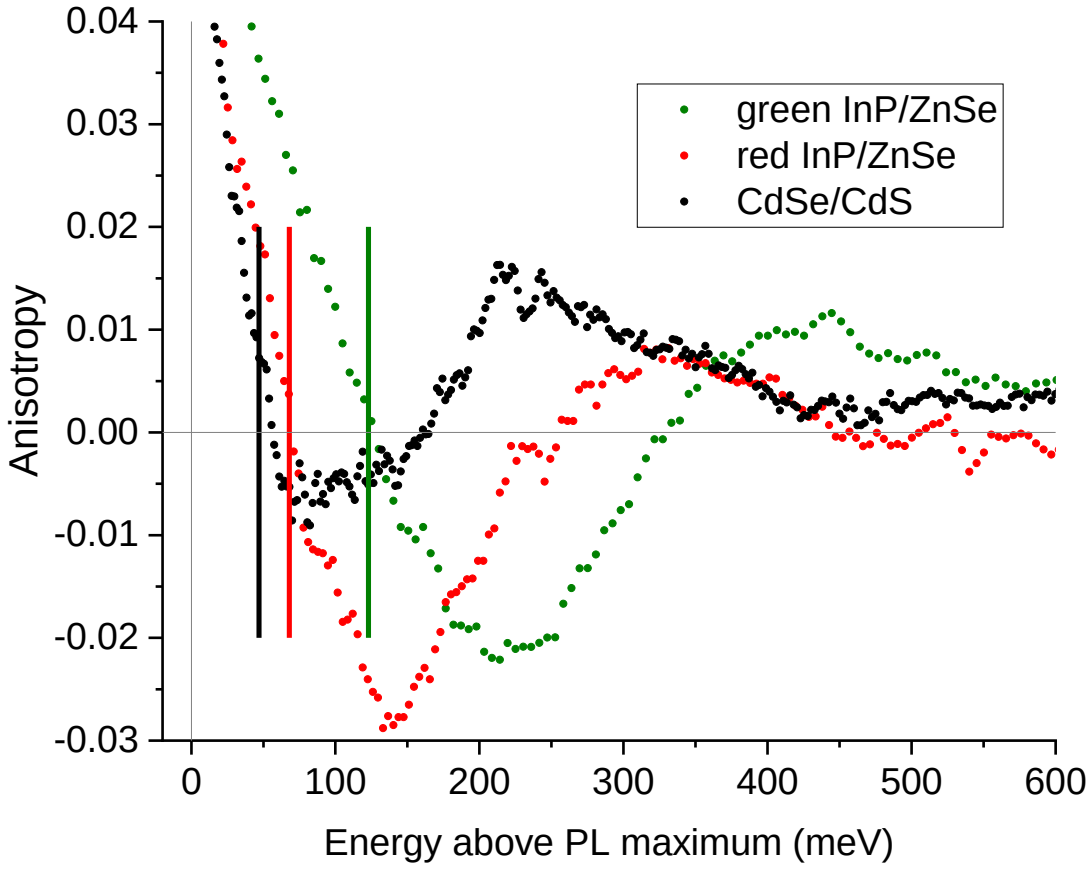

Figure 2.7: PLE anisotropy spectra for InP/ZnSe/ZnS particles having core diameters of 1.85 nm (green) and 2.9 nm (red) with approximately 2 nm thick ZnSe shells and for CdSe/CdS particles having a core diameter of 4.0 nm and a 1.2 nm monolayer CdS shell. Vertical lines indicate the Stokes shift for the corresponding particle.

When the QD is excited very near the observation wavelength the likelihood that the absorbing and emitting state are the same is very high and as such we expect a positive anisotropy. It is of interest to note the lowest energy crossover point in figure 2.7 from positive to negative anisotropy occurs at an energy that almost exactly matches the Stokes shift energy. In the $1S_{3/2}$-$1S_e$ envelope transition most of the oscillator strength is in the x,y-polarized $\pm1^U$ and z-polarized $\pm0^U$ state, and the absorption maximum is close to the midpoint energy of these states. The Stokes shift is the energy difference between this absorption maximum and the maximum of the emission from the $\pm1^L$ state. The anisotropy zero also occurs at the midpoint between these energies and is therefore very close to the absorption maximum where the x,y-polarized $\pm1^U$ and z-polarized $\pm0^U$ state would have roughly equivalent contributions leading to an unpolarized transition. The qualitative behavior of the anisotropy spectra is consistent with the assumption that most of the Stokes shift can be assigned to energy splitting in the angular momentum fine structure.

In a QD with oblate geometry luminescence occurs from the (x,y-polarized) $\pm1^L$ state, and the detection energy is set to the center of this band in these polarization studies. At higher excitation energies, most of the excitation is to the higher lying, more strongly allowed $\pm1^U$ and 0^U fine structure levels. It is important to note that excitation on the low energy side of the $\pm1^U$ and 0^U states selectively excites the x,y-polarized $\pm1^U$ state, and excitation on the high energy side of these states selectively excites the z-polarized $\pm0^U$ state. As the excitation energy is increased above the detection energy, excitation is to primarily the $\pm1^L$ states at the lowest energies, and the $\pm1^U$ states at slightly higher energies. Below the midpoint of the $\pm1^U$ and 0^U states, both the emitting and the dominant fraction of the absorbing oscillators are x,y polarized and figure 2.7 shows that in this low energy regime, a positive anisotropy is observed. When excitation is to the blue of the midpoint between the $\pm1^U$ and 0^U states, most of the absorption is to the z-polarized 0^U state, and a negative anisotropy is observed. The lowest energy anisotropy zero occurs at an energy between the $\pm1^U$ and 0^U states, corresponding to about 67 and 125 meV for the red and green InP/ZnSe/ZnS QDs, respectively. At excitation energies above the blue edge of the $1S_{3/2}$-$1S_e$ absorption bands, the spectroscopy is complicated by many transitions involving other envelope functions. [26,27] However, just as with the $1S_e$-$1S_{3/2}$ transition, the low energy edges of these transitions are dominated by absorption into the lower energy, x,y-polarized fine structure levels. Following relaxation to the emissive x,y-polarized $\pm1^L$ level of the $1S_{3/2}$-$1S_e$ band, the higher energy positive anisotropy is observed.

This assignment is consistent with the data in reference[28], which indicates that in InP/ZnS QDs, the dark/bright ($\pm2/\pm1^L$) and bright/bright ($\pm1^U/\pm1^L$) splittings decrease with increasing core size. Figure 2.7 also presents an analogous anisotropy spectrum for CdSe/CdS particles having a comparable exciton energy. The most obvious difference is that the exchange interaction is considerably smaller in the larger diameter CdSe/CdS particles. This is also consistent with the results in reference [29], which reports smaller dark/bright splittings and hence smaller exchange interactions for CdSe/CdS, that also decrease with increasing core size and shell thickness.

This is in line with the assignment that the Stokes shift is determined by the fine structure, asymmetric phonon broadening, and the previously mentioned band offset inhomogeneity and is not due to trap emission as proposed Janke et al. With this understanding it is now possible to accurately model the PLE spectrum.

2.4 Calculated Photoluminescence Excitation Spectrum

This model allows for semiquantitative analysis of the PLE spectrum near the band edge. Analysis starts by first considering the simple case of a non-zero homogeneous width and a single inhomogeneous (due to size inhomogeneity) distribution. The PLE intensity with detection at E_d and excitation at E_x is given by:

$$\text{(Eq 2.3)} \qquad I(E_d, E_x) = \int dE\, G_H(E - E_d)\, G_H(E + \Delta E - E_x)\, G_I(E_0 - E)$$

E_0 is the center emission wavelength, ΔE is the splitting between the absorbing and emitting states, and $G_H(E)$ and $G_I(E)$ are the homogeneous and inhomogeneous energy distributions, respectively. The value of ΔE gives the fine structure contribution to the overall Stokes shift. These values of E_0 vary with the nature of the core-shell interface, as described by the model in figure 2.4. With this additional source of inhomogeneity, the convolution integral in equation 2.3 becomes:

$$\text{(Eq 2.4)} \qquad I(E_d, E_x) = \int dE_0 \int dE\, G_H(E - E_d)\, G_H(E + \Delta E - E_x)\, G_I(E_0 - E)\, G_{I2}(E_0 - E_c)$$

Where $G_{I2}(E)$ is the inhomogeneous distribution associated with the core-shell band offsets with E_c as its center. Similarly, the analogous treatment with the same energy distributions results in an expression for the $1S_{3/2}$-$1S_e$ PL intensity, given by:

$$\text{(Eq 2.5)} \qquad PL(E_d) = \int dE_0 \int dE\, G_H(E - E_d)\, G_I(E_0 - E)\, G_{I2}(E_0 - E_c)$$

Evaluation of equations 2.3 – 2.5 requires the use of parameters to model the energy distribution functions $G_H(E)$, $G_I(E)$ and $G_{I2}(E)$. However, fitting the PLE maxima in figure 2.3 and considering the widths of the PL and PLE spectra imposes constraints on the functional forms and parameters used in the $G_H(E)$, $G_I(E)$ and $G_{I2}(E)$ distribution functions. The initial approach of assuming Gaussian distributions with standard deviations σ_H, σ_I and σ_{I2} proves to be a poor approximation. Based on single particle and photon-correlation Fourier spectroscopy,[4] InP/ZnSe QDs show an asymmetric phonon broadening to the emission described by a Gaussian having a 40% the total amplitude and a width that is 2.5 times larger than the central part of the homogeneous spectrum. Specifically, for the homogeneous emission spectrum:

$$\text{(Eq 2.6)} \qquad G_H(E) = \frac{1}{\sigma_H \sqrt{2\pi}} \exp\left(-E^2 / 2\sigma_H^2\right) \qquad \text{for } E > 0$$

$$\text{(Eq 2.7)} \qquad G_{H+}(E) = \frac{0.6}{\sigma_H \sqrt{2\pi}} \exp\left(-E^2 / 2\sigma_H^2\right) + \frac{0.4}{\sigma_H \sqrt{2\pi}} \exp\left(-E^2 / 2(2.5\sigma_H)^2\right) \quad \text{for } E < 0.$$

The homogeneous absorption spectrum reverses the negative and positive energy phonon contributions and has a tail to the blue. Although based on the results of photon correlation spectroscopy, this model is not unique; any functional form that has a long low-energy tail gives the same qualitative result.

The parameters used to fit the curves in figure 2.3 are given in terms of full-width-half-maximum widths, which are related to the Gaussian sigma values by the equation, $w = \sigma(8\ln 2)^{-1/2}$. All the calculated curves in figure 2.3 take w_H to be 76 meV, so the broad homogeneous width in the second term of equation 2.6 is 190 meV. Figure 2.3 finds the center energies for the core-only and the core-derivatized QDs having 2.9 and 2.76 nm cores to be 2.049, 2.006 and 2.026 eV, respectively. For both types of core-derivatized particles the splitting between the absorbing and emitting states, ΔE, is taken to be 52 meV, and the total (size and offset) inhomogeneous widths, $w_{Itot} = (w_I^2 + w_{I2}^2)^{1/2}$, are 110 meV. We note that the core particles have somewhat larger values of ΔE, 79 meV, compared to 52 meV for the core/shell QDs. This is consistent with the larger exchange interaction in the core-only particle, as discussed above.

The fits to the results in figure 2.3 give only the total inhomogeneous width (w_{Itot}). Separating the amounts of the size and offset inhomogeneities requires an accurate measure of the core size dispersion. Values of w_{Itot} are obtained from the fits in figure 2.3, so using TEM images we can determine w_I, and therefore values of w_{I2} are obtained. As mentioned previously TEM images were taken of the InP cores in figure 2.2A and the size distribution and it was found to be 3.1 ± 0.3 nm. In the case of these cores the width of the inhomogeneous energy distribution due to size was found to be slightly larger than the total observed inhomogeneous width of 138 meV. The core size dispersion in the core-derivatized particles was assumed to be similar to that measured for the core-only particles. The effective mass approximation calculations described earlier and in reference[5] gives a ratio of the derivatives dE_x/dr_{core} of 0.64. This corresponds to a size inhomogeneity of 0.64 x 138 meV = 88 meV in the final core/shell/shell QDs. With a total (size plus offset) inhomogeneous width of 110 meV derived from figure 2.3, an offset inhomogeneous width of 66 meV is calculated.

This calculation shows that inhomogeneity of the core-shell interface makes large contributions to both the absorbance congestion, and photoluminescence width. The contribution from the offset inhomogeneity to emission widths is approximately 75% of the contribution of size inhomogeneity. This factor is currently uncontrolled in virtually all synthesis observed in the literature and gives a new avenue from which to engineer narrower emitting InP/ZnSe QDs.

2.5 Conclusion

This chapter identified ways in which both the absorption and emission spectra of InP/ZnSe QDs are complicated by considerations that don't significantly contribute to the features of their cadmium-based counterparts. The widths of the $1S_{3/2}$-$1S_e$ absorption, PL peaks and the presence of the detection energy dependent continuum absorption in the PLE spectra can be understood in terms of two types of inhomogeneity: size inhomogeneity and core/shell interface inhomogeneity. Size inhomogeneity affects the spectra in a well-

understood way: larger particles have less quantum confinement and therefore have lower energy optical transitions. The mechanism by which the nature of the core-shell interface affects the spectroscopy is through an electrostatic interaction produced by the core-shell interfacial dipole. While the effect of size inhomogeneity has been well understood in both InP and CdSe, and there are many currently techniques to minimize it, the effect of band offset inhomogeneity has previously been unknown and is somewhat to unique the InP/ZnSe system. This work has laid the groundwork for quantitative measurement of the effect of band offset inhomogeneity that can be used in synthesis optimization.

2.6 Experimental Methods

Static absorption spectra were measured using a Cary 50 UV−vis spectrophotometer. Polarization resolved PLE and Static luminescence spectra were measured on a Jobin-Yvon Fluorolog 3.

2.7 References

(1) Kuno, M. *Introductory Nanoscience*; Garland Science, 2011. https://doi.org/10.1201/9780429258442.

(2) Yu, P. Y.; Cardona, M. *Fundamentals of Semiconductors*; Springer Berlin Heidelberg: Berlin, Heidelberg, 2010. https://doi.org/10.1007/978-3-642-00710-1.

(3) Norris, D. J.; Bawendi, M. G. Measurement and Assignment of the Size-Dependent Optical Spectrum in CdSe Quantum Dots. *Phys Rev B* **1996**, *53* (24), 16338–16346. https://doi.org/10.1103/PhysRevB.53.16338.

(4) Berkinsky, D. B.; Proppe, A. H.; Utzat, H.; Krajewska, C. J.; Sun, W.; Šverko, T.; Yoo, J. J.; Chung, H.; Won, Y.-H.; Kim, T.; Jang, E.; Bawendi, M. G. Narrow Intrinsic Line Widths and Electron–Phonon Coupling of InP Colloidal Quantum Dots. *ACS Nano* **2023**, *17* (4), 3598–3609. https://doi.org/10.1021/acsnano.2c10237.

(5) Nguyen, A. T.; Jen-La Plante, I.; Ippen, C.; Ma, R.; Kelley, D. F. Extremely Slow Trap-Mediated Hole Relaxation in Room-Temperature InP/ZnSe/ZnS Quantum Dots. *The Journal of Physical Chemistry C* **2021**, *125* (7), 4110–4118. https://doi.org/10.1021/acs.jpcc.0c11317.

(6) Jeong, B. G.; Chang, J. H.; Hahm, D.; Rhee, S.; Park, M.; Lee, S.; Kim, Y.; Shin, D.; Park, J. W.; Lee, C.; Lee, D. C.; Park, K.; Hwang, E.; Bae, W. K. Interface Polarization in Heterovalent Core–Shell Nanocrystals. *Nat Mater* **2022**, *21* (2), 246–252. https://doi.org/10.1038/s41563-021-01119-8.

(7) Lange, H.; Kelley, D. F. Spectroscopic Effects of Lattice Strain in InP/ZnSe and InP/ZnS Nanocrystals. *The Journal of Physical Chemistry C* **2020**, *124* (41), 22839–22844. https://doi.org/10.1021/acs.jpcc.0c07145.

(8) Morgan, D. P.; Kelley, D. F. Mechanism of Hole Trap Passivation in CdSe Quantum Dots by Alkylamines. *The Journal of Physical Chemistry C* **2018**, *122* (44), 25661–25667. https://doi.org/10.1021/acs.jpcc.8b08798.

(9) Kalyuzhny, G.; Murray, R. W. Ligand Effects on Optical Properties of CdSe Nanocrystals. *J Phys Chem B* **2005**, *109* (15), 7012–7021. https://doi.org/10.1021/jp045352x.

(10) Houtepen, A. J.; Hens, Z.; Owen, J. S.; Infante, I. On the Origin of Surface Traps in Colloidal II–VI Semiconductor Nanocrystals. *Chemistry of Materials* **2017**, *29* (2), 752–761. https://doi.org/10.1021/acs.chemmater.6b04648.

(11) Jasieniak, J.; Califano, M.; Watkins, S. E. Size-Dependent Valence and Conduction Band-Edge Energies of Semiconductor Nanocrystals. *ACS Nano* **2011**, *5* (7), 5888–5902. https://doi.org/10.1021/nn201681s.

(12) Munro, A. M.; Zacher, B.; Graham, A.; Armstrong, N. R. Photoemission Spectroscopy of Tethered CdSe Nanocrystals: Shifts in Ionization Potential and Local Vacuum Level As a Function of Nanocrystal Capping Ligand. *ACS Appl Mater Interfaces* **2010**, *2* (3), 863–869. https://doi.org/10.1021/am900834y.

(13) Wang, C.; Shim, M.; Guyot-Sionnest, P. Electrochromic Nanocrystal Quantum Dots. *Science (1979)* **2001**, *291* (5512), 2390–2392. https://doi.org/10.1126/science.291.5512.2390.

(14) Soreni-Harari, M.; Yaacobi-Gross, N.; Steiner, D.; Aharoni, A.; Banin, U.; Millo, O.; Tessler, N. Tuning Energetic Levels in Nanocrystal Quantum Dots through Surface Manipulations. *Nano Lett* **2008**, *8* (2), 678–684. https://doi.org/10.1021/nl0732171.

(15) Carroll, G. M.; Tsui, E. Y.; Brozek, C. K.; Gamelin, D. R. Spectroelectrochemical Measurement of Surface Electrostatic Contributions to Colloidal CdSe Nanocrystal Redox Potentials. *Chemistry of Materials* **2016**, *28* (21), 7912–7918. https://doi.org/10.1021/acs.chemmater.6b03493.

(16) Kroupa, D. M.; Vörös, M.; Brawand, N. P.; McNichols, B. W.; Miller, E. M.; Gu, J.; Nozik, A. J.; Sellinger, A.; Galli, G.; Beard, M. C. Tuning Colloidal Quantum Dot Band Edge Positions through Solution-Phase Surface Chemistry Modification. *Nat Commun* **2017**, *8* (1), 15257. https://doi.org/10.1038/ncomms15257.

(17) Santra, P. K.; Palmstrom, A. F.; Tanskanen, J. T.; Yang, N.; Bent, S. F. Improving Performance in Colloidal Quantum Dot Solar Cells by Tuning Band Alignment through Surface Dipole Moments. *The Journal of Physical Chemistry C* **2015**, *119* (6), 2996–3005. https://doi.org/10.1021/acs.jpcc.5b00341.

(18) Nguyen, E. P.; Carey, B. J.; Ou, J. Z.; van Embden, J.; Gaspera, E. Della; Chrimes, A. F.; Spencer, M. J. S.; Zhuiykov, S.; Kalantar-zadeh, K.; Daeneke, T. Electronic Tuning of 2D MoS_2 through Surface Functionalization. *Advanced Materials* **2015**, *27* (40), 6225–6229. https://doi.org/10.1002/adma.201503163.

(19) Morgan, D. P.; Kelley, D. F. What Does the Transient Absorption Spectrum of CdSe Quantum Dots Measure? *The Journal of Physical Chemistry C* **2020**, *124* (15), 8448–8455. https://doi.org/10.1021/acs.jpcc.0c02566.

(20) Sun, H.; Cavanaugh, P.; Jen-La Plante, I.; Ippen, C.; Bautista, M.; Ma, R.; Kelley, D. F. Biexciton and Trion Dynamics in InP/ZnSe/ZnS Quantum Dots. *J Chem Phys* **2022**, *156* (5), 054703. https://doi.org/10.1063/5.0082223.

(21) Janke, E. M.; Williams, N. E.; She, C.; Zherebetskyy, D.; Hudson, M. H.; Wang, L.; Gosztola, D. J.; Schaller, R. D.; Lee, B.; Sun, C.; Engel, G. S.; Talapin, D. V. Origin of Broad Emission Spectra in InP

Quantum Dots: Contributions from Structural and Electronic Disorder. *J Am Chem Soc* **2018**, *140* (46), 15791–15803. https://doi.org/10.1021/jacs.8b08753.

(22) Sercel, P. C.; Efros, A. L. Band-Edge Exciton in CdSe and Other II-VI and III-V Compound Semiconductor Nanocrystals - Revisited. *Nano Letters*. American Chemical Society July 11, 2018, pp 4061–4068. https://doi.org/10.1021/acs.nanolett.8b01980.

(23) Rodina, A. V.; Efros, A. L. Band-Edge Biexciton in Nanocrystals of Semiconductors with a Degenerate Valence Band. *Phys Rev B Condens Matter Mater Phys* **2010**, *82* (12). https://doi.org/10.1103/PhysRevB.82.125324.

(24) Efros, A. L.; Rosen, M.; Kuno, M.; Nirmal, M.; Norris, D. J.; Bawendi, M. *Band-Edge Exciton in Quantum Dots of Semiconductors with a Degenerate Valence Band: Dark and Bright Exciton States*; 1996.

(25) Sercel, P. C.; Shabaev, A.; Efros, A. L. Photoluminescence Enhancement through Symmetry Breaking Induced by Defects in Nanocrystals. *Nano Lett* **2017**, *17* (8), 4820–4830. https://doi.org/10.1021/acs.nanolett.7b01662.

(26) Norris, D. J.; Bawendi, M. G. Measurement and Assignment of the Size-Dependent Optical Spectrum in CdSe Quantum Dots. *Phys Rev B* **1996**, *53* (24), 16338–16346. https://doi.org/10.1103/PhysRevB.53.16338.

(27) Cavanaugh, P.; Wang, X.; Bautista, M. J.; Jen-La Plante, I.; Kelley, D. F. Spectral Widths and Stokes Shifts in InP-Based Quantum Dots. *J Chem Phys* **2023**, *159* (13). https://doi.org/10.1063/5.0165956.

(28) Brodu, A.; Ballottin, M. V.; Buhot, J.; van Harten, E. J.; Dupont, D.; La Porta, A.; Prins, P. T.; Tessier, M. D.; Versteegh, M. A. M.; Zwiller, V.; Bals, S.; Hens, Z.; Rabouw, F. T.; Christianen, P. C. M.; de Mello Donega, C.; Vanmaekelbergh, D. Exciton Fine Structure and Lattice Dynamics in InP/ZnSe Core/Shell Quantum Dots. *ACS Photonics* **2018**, *5* (8), 3353–3362. https://doi.org/10.1021/acsphotonics.8b00615.

(29) Accanto, N.; Masia, F.; Moreels, I.; Hens, Z.; Langbein, W.; Borri, P. Engineering the Spin–Flip Limited Exciton Dephasing in Colloidal CdSe/CdS Quantum Dots. *ACS Nano* **2012**, *6* (6), 5227–5233. https://doi.org/10.1021/nn300992a.

Chapter 3. Time Resolved Spectroscopy of Indium Phosphide Quantum Dots

3.1 Introduction

Accurate prediction of radiative lifetimes is a starting point for the design of QDs intended for device applications. This chapter will demonstrate how absorbance experiments can be used to calculate the photon cross-section of a QD and relate that to the radiative lifetime. Comparison with Time Resolved Photoluminescence (TRPL) experiments will show that a thermal Boltzmann distribution between emissive and non-emissive states is required to relate the two values, as is predicted by the fine structure discussed in chapter 1. Furthermore, the observed radiative lifetime varies across the emission band in a way that is predictable using the Einstein relations. This property can be used to determine the extent of aggregation in samples by looking at deviations in the wavelength dependent radiative lifetime due to Förster resonant energy transfer (FRET).

If during the synthesis of InP/ZnSe QDs, the presence of indium is not carefully controlled during the shelling, excess indium can become incorporated into the ZnSe shell. Early in this project it was discovered that the photophysical properties of InP/ZnSe QDs with indium to phosphorous ratios near 1:1 behaved differently than those with larger indium to phosphorous ratios. It was determined, and will be thoroughly explored in this chapter, that this excess indium contributed to the formation of transient hole traps. These shallow hole traps allow for holes to equilibrate between the valence band and the traps states, leading to significant effects on the TRPL decay.

In higher fluence conditions the InP/ZnSe QDs can absorb a second photon either simultaneously or, more often, sequentially. When this happens a biexciton forms. Biexcitons have their own fine structure that can be interpreted by considering the corresponding literature on CdSe QDs.[1] In InP QDs this new fine structure has an allowed transition as its lowest state and, based on the comparative oscillator strengths of the exciton and biexciton, predicts a radiative lifetime on the order of a few nanoseconds. However, the observed radiative lifetime is significantly faster, governed primarily by the Auger recombination rate.

Auger recombination is a process that competes with biexcitons recombining radiatively. In this process two carriers recombine and transfer their momentum to either of the two remaining carriers. This can create very high energy or “hot” carriers. These “hot” carriers are of great interest because they are known to be able to perform chemical reactions that can lead to the degradation and quenching of photoluminescence in QDs. Minimizing or controlling the generation of these “hot” carriers is of utmost importance to increasing the stability of InP/ZnSe QDs at high fluences. TRPL and TA biexciton measurements will be compared to extract information about the energetic position of the biexciton emitting state as compared to the single exciton emitting state. Additionally, the indium based transient traps will be shown to contribute to biexciton kinetics. Biexcitons states involving a trapped carrier will exhibit significant deviations in behavior from their counterparts without a trapped carrier, and these differences will allow for synthetic control over the formation of “hot” carriers.

3.2 Absorbance, Emission and Radiative Lifetime Relationships

Accurate prediction of the radiative lifetimes is a starting point for the design of QDs based applications. Absorption intensities and radiative lifetimes are related to each other through the Einstein A and B coefficients. The Einstein A coefficient is of particular interest because it represents the rate at which an excited state spontaneously emits a photon. In a two-level system the radiative lifetime of a transition is one over the Einstein A coefficient.

The Einstein A coefficient is calculable using the particle core and shell volumes along with the wavelength-dependent "absorption coefficient," α, of the bulk materials. At 350 nm, α = 2.0 e+5 cm^{-1} for ZnSe and α = 6.8 e+5 cm^{-1} for InP. This value is much higher for InP because 350 nm is much further above the bandgap in InP than it is for ZnSe, and therefore at this wavelength InP has a much larger density of states. We evaluate the QD absorption at 350 nm and equate this to the absorption of equal volumes of the bulk materials. This assumes that there are no quantum confinement effects at this wavelength. 350 nm is more than 1 eV above the exciton, so this is a good approximation. The relative volumes or core and shell materials can be determined by ICP (induction coupled plasma spectrometry), and the total volume of the average QD can be determined through TEM or by using published sizing curves.[2] Knowing the volume of the QD allows for easy interconversion from the "absorption coefficient", α in cm^{-1} to the absorption cross-section σ cm^2. Eq 3.1 can then be used to relate the photon cross-section to a molar extinction coefficient that can be used in the determination of the Einstein A.[3–5]

(Eq 3.1) $$\sigma(cm^2) = 2.303(1000cm^3/liter)\varepsilon/N_a$$

(Eq 3.2) $$A = 2.88x10^{-15}\frac{n^2}{\lambda^4}\int \varepsilon(\lambda)\, d\lambda$$

These calculations are initially used to determine the absorption coefficient at 350 nm, however emission in QDs come from the lowest allowed envelope function, the $1S_e - 1S_{3/2}$ transition. Using the absorbance spectrum to find the ratio of cross-section at 350 to the $1S_e - 1S_{3/2}$ absorbance peak allows for the determination of the Einstein A of the $1S_e - 1S_{3/2}$ transition.

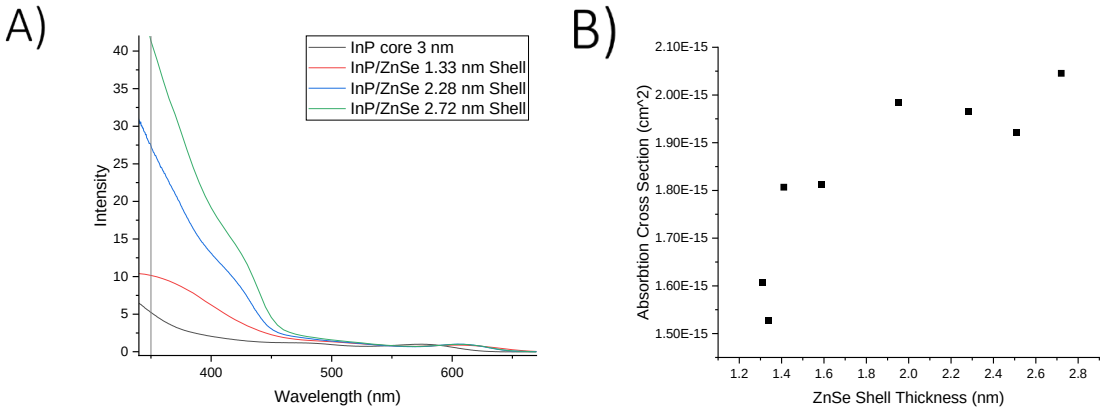

Figure 3.1: A) Absorption spectrum of 3 nm diameter core and core derivatized QDs 2.9 nm core diameter with 1.33 nm, 2.28nm, and 2.72 nm shell thicknesses normalized to first exciton. Intensity at 350 nm is shown using a reference line. B) Calculated absorption cross section $\sigma(cm^2)$ of a series of core derivatized QDs with identical cores and varying shell thicknesses.

Figure 3.1B shows a change in behavior in the absorption cross section of the first exciton as additional layers of ZnSe shell are added to the InP/ZnSe QD. Initially there is an increase in the absorption cross section of 30%, however after 1.8 nm this increase slows and levels off. There are two processes that affect this value, the delocalization of the electron into the shell as more shell is added, increasing the oscillator strength and the decrease in overlap as the electron expands past the confinement of the hole. The increase in oscillator strength suggests that the former is the larger effect, and the inflection suggests that the electron does not significantly further delocalize after 1.8 nm of shell is added. This is in strong agreement with figure 2.6 of the previous chapter, which showed a similar trend of electron delocalization with shell thickness.

When radiative lifetimes are computed with this method they are typically on the order of a few nanoseconds. However, it's crucial to understand that these calculated oscillator strengths pertain to the entire $1S_e - 1S_{3/2}$ transition, whereas the fine structure state that is performing the emission has only a fraction of that intensity.[1,6,7] Additionally, chapter 1 pointed out that the lowest energy state is dark. The splitting between the emitting ($\pm 1^L$) and dark (± 2) states is very small which leads to roughly half of the exciton population exists in the dark exciton state at any given moment.[8] The close proximity of the emitting ($\pm 1^L$) and dark (± 2) states effectively doubles the observed radiative lifetime. In oblate geometries such as those experimentally observed the 0L state is high enough above the $\pm 1^L$ and ± 2 states that it does not meaningfully contribute to the Boltzmann distribution. Consequently, the observed radiative lifetime determined by TCPC amounts to around 30 nanoseconds on average, as shown in figure 3.2, resulting in an intrinsic radiative lifetime of approximately 15 nanoseconds for the emitting ($\pm 1^L$) state.

Direct measurement of radiative lifetimes is typically performed using time-resolved photoluminescence (TRPL) experiments. In these experiments, a light pulse is split into two beams. One beam is directed to a photodiode as a timing reference, while the other passes through the sample. Light from the sample is then directed through a monochromator and put onto a detector. Using the difference in arrival time between the timing pulse and the detector it becomes possible to measure the average observed radiative lifetime of a sample for specific wavelength ranges.

The photoluminescence kinetics of a molecule or quantum dot can provide insights into the emitting states and their dynamics. In its simplest form, the luminescent species can be conceptualized as a two-level electronic system undergoing radiative relaxation. In a more comprehensive scenario, the decay rate of the excited state is a combination of radiative and nonradiative rates. Generally, the observed radiative lifetime τ, which is the inverse of the decay rate, is what is measured in these experiments. The observed lifetime can therefore be expressed as $1/\tau = 1/\tau_r + 1/\tau_{nr}$. In QDs, nonradiative decay is often facilitated by defect sites serving as electron-hole recombination centers. This process competes with photoluminescence decay and reduces the PL quantum yield. Exceptionally high-quality QDs lack such recombination centers, leading to sluggish nonradiative electron-hole recombination. Consequently, they exhibit near unity PL QYs, and their PL decays closely align with radiative decay times. This relationship is described by:

$$\text{PLQY} = \frac{k_r}{k_r + k_{nr}} \qquad \text{(Eq 3.3)}$$

However, these relations only hold true for uniform populations, or populations in which each QD has the same radiative and non-radiative rates. In a sample with an ensemble of QDs there can be members that have a variety of defects that contribute non radiative rates to some number of QDs. In this case the QY is the sum of QYs of each unique population of QDs in the ensemble weighted by what percent of the ensemble they make up.

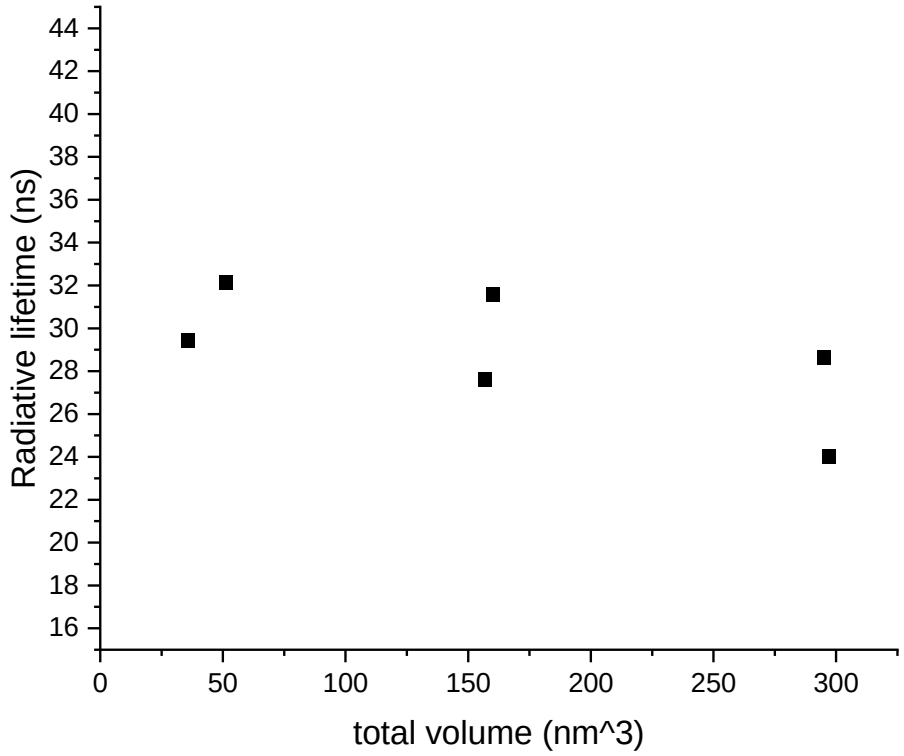

Figure 3.2: Radiative lifetimes of stoichiometric particles determined by TCPC, with between 2.9 and 3.05 nm diameter cores with shell of thicknesses varying from 1-3 nm.

In an InP/ZnSe nanocrystal increasing the shell thickness changes three factors that contribute to determining the radiative lifetime. Increasing the overall size of the particle increases the number of oscillators (unit cells) in the exciton transition and thereby increases the radiative rate. This effect is partially countered by a decrease in the electron-hole overlap, decreasing radiative rate. The electron-hole overlap quantifies the spatial overlap between the wave functions of an electron and a hole in a semiconductor crystal lattice. It can be expressed as:

$$S = \int \psi_{e^-} \, \psi_{h^+} dv \qquad \text{(Eq 3.4)}$$

Where ψ_{e^-} is the wavefunction of the electron and ψ_{h^+} is the wavefunction of the hole. Another factor affecting the radiative rate is the decrease in fine structure splitting with increasing particle size as demonstrated in figure 2.6. This has the effect of increasing the population of the bright state and thereby decreasing the radiative lifetime. However due to the small splitting between the emissive and non-emissive fine structure states this is a very small effect. The combined contributions of these factors are

observed to be a small net increase in the radiative rate (decrease in the radiative lifetime) with increasing shell thickness as shown in figure 3.2.

When performing TRPL experiments it is important to prevent reabsorption effects and Förster resonance energy transfer (FRET). The extent of reabsorption depends on the optical density of the sample at the first exciton. To minimize reabsorption effects the optical density at the first exciton was kept below .05 OD for the measurements taken in figure 3.2 and 3.3. Reabsorption involves the emission and subsequent absorption of a photon by different QDs, causing delayed and red-shifted emission.[4] FRET is a phenomenon in which energy is transferred from one excited QD (donor) to another nearby QD (acceptor) through nonradiative dipole-dipole coupling.[9] A redshift in the emission is the result of both processes as energy transfer is favored when the donor QD has a larger bandgap than the acceptor. While these processes share a conceptual similarity, they differ in their mechanisms. Reabsorption scales with the optical density of the sample and is relatively straightforward to calculate. The efficiency of FRET is highly dependent on the distance between the donor and acceptor molecules and scales as the inverse sixth power of the distance. This means that FRET is most efficient at very short distances (typically in the range of a few nanometers to around 10 nm).

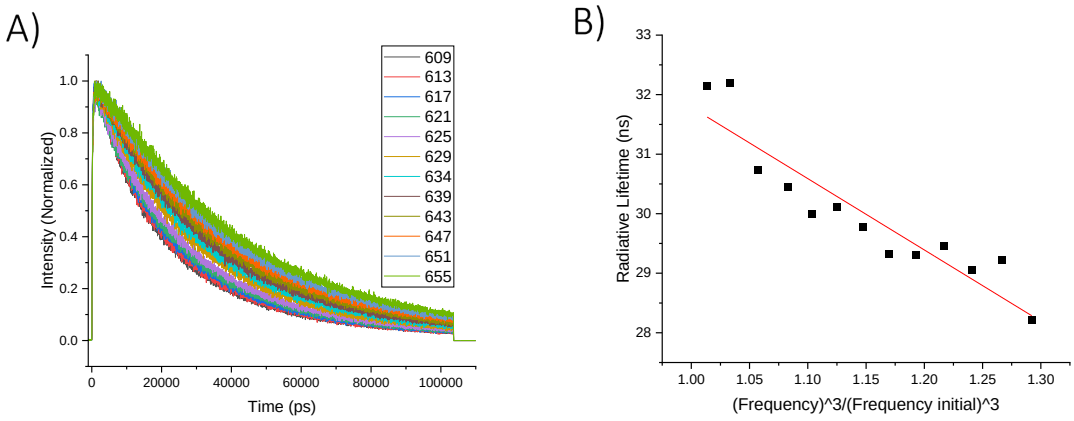

Figure 3.3: A) Radiative lifetime of an ensemble of QDs as the emission wavelength being observed is varied. B) The fits of radiative lifetime from A as a function of the change in the cube of the frequency.

FRET can be evaluated by performing a spectral reconstruction, tracking the radiative lifetime of a sample across multiple wavelengths. In the absence of FRET, the radiative lifetime's variation should scale with one over the wavelength cubed, as was shown in equation 3.2, whereas the presence of FRET would result in longer lifetimes at the red edge of the sample's spectrum. The one over wavelength cubed relationship is generally plotted in terms of frequency cubed, which then gives a linear fit in the limit of no aggregation as shown in figure 3.3B. Deviation from the linear fit then allows for the determination of the extent of aggregation in a sample. Aggregation can have significant detrimental effects on the QY of QDs. One can consider the possibility that the QDs form aggregates in solution and that there is FRET between QDs in these aggregates. In this

case, the exciton can hop from particle to particle until it finds one with fast nonradiative processes, and this could quench PL from the entire aggregate. Thus, when extensive FRET occurs, one would expect to observe an overall faster PL decay and for the blue edge of the PL spectrum to exhibit much shorter decays than the red edge beyond what is predicted by the frequency cubed dependance of Einstein A relationship.

The argument presented above hinges on the implicit assumption that the absorption and emission spectra of these particles are primarily influenced by inhomogeneous broadening. Comparative analysis of the linewidths observed in ensemble measurements and those from analogous single-particle investigations reveals a noteworthy distinction. Specifically, the linewidths measured from single nanoparticles exhibit a significantly narrower profile when compared to the broader linewidths observed in ensemble measurements.[8] In other words, the broadening of spectral lines within the ensemble arises primarily from variations in the local environments, band offsets, and/or sizes of individual nanoparticles. Refer back to chapter 2 for a full discussion of the role of inhomogeneity in ensemble measurements.

This section has shown that in the case of stoichiometric particles the TRPL decay is interpretable using the well-established methodology put in place for cadmium based QDs. Calculations of the photon cross-section of these QDs follow the same trend in the extent of electron delocalization with shell thickness that was shown in figure 2.6. This photon cross-section was related to a radiative lifetime, and that radiative lifetime was related to the observed TRPL data using the fine structure discussed in the previous two chapters. It has also explored a variety of ways in which the ensemble measurements can be complicated by factors such as concentration and FRET. This framework will be key for the interpretation of the more complex dynamics of the nonstoichiometric and core derivatized particles.

3.3 Single Exciton Trap Dynamics

The effects of transient trapping in these particles were first noticed during determination of QD lifetimes. The TRPL of particles with indium to phosphorous ratios greater than 1.05 showed a slow rise component that varied from a few hundred picoseconds to nanoseconds with increasing shell size as shown in figure 3.4.[10,11] This unusual behavior has not been seen in CdSe QDs. Semiconductor QDs often contain impurities and/or defects that may create energy levels that are within the band gap of that QD. If these defects are far enough inside of the band gap so as to prevent the trapped carriers from thermally repopulating to the band edge, then they will become irreversibly trapped.[12] These carriers end up eventually undergoing nonradiative recombination, leading to a drop in the QY. The InP/ZnSe QDs used in this study all have high QYs, usually in excess of 90%, and narrow linewidths. This along with the data presented in chapter 2 points to emission from a thermal repopulation of the band edge from a trap state.

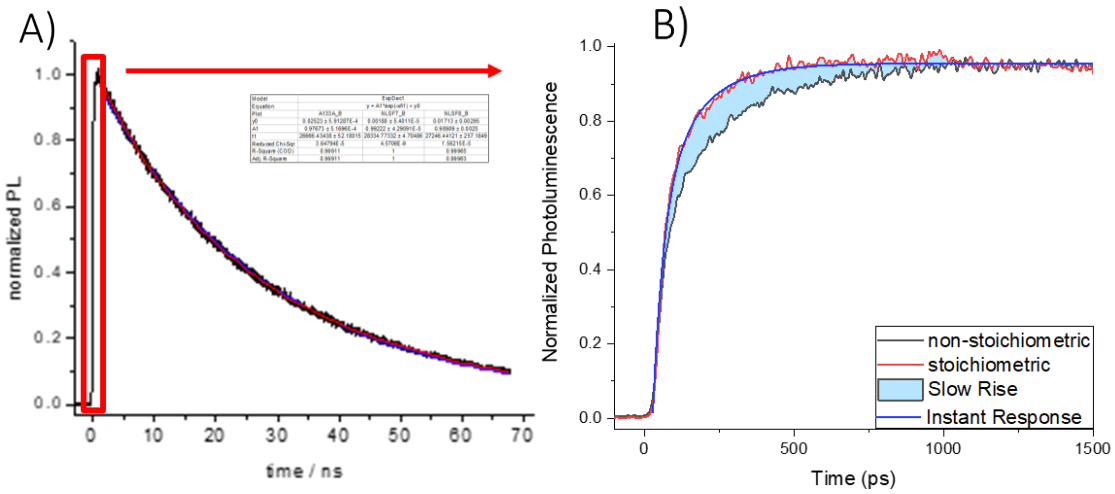

Figure 3.4: A) PL decays of a S-2.51 QD obtained following 423 nm excitation with detection at the 624 nm PL maximum. Also shown is a fit curve corresponding to a 28 ns single exponential decay B) Examples of the first 1.5 ns of a stoichiometric particle with a nearly 100% instrument-limited rise time is also shown (red curve) and core derivatized QD with a biexponential rise time of 162 ps 13.5%, and 1750 ps 9.0% (black curve). For comparison, the instrument limited response is shown in blue. The instrument limited response is what would be observed if carrier cooling processes were fast and emission from the sample was instantaneous compared to the timescale of the experiment.

Both the amplitudes and the time constants of the risetime are strongly dependent on the shell thickness. In addition, the PL risetimes observed in the thicker shell core-derivatized QDs have larger amplitudes and longer time constants than previously reported for the nonstoichiometric QDs.[5,11,13] In the case of the thickest shells, there is clearly a distribution of time constants for the risetimes, and the kinetics cannot be adequately fit to a single exponential. In these cases, the kinetics are fit to a biexponential rise. The most accurate fits to the data of the thinner shell core-derivatized QDs also use a biexponential risetime. The longest components in the thick shell core-derivatized particles are greater than 1 ns, which is much longer than the approximately 350 ps used to fit the nonstoichiometric QD rise kinetics. The PL risetimes are assigned to hole tunneling from shell traps to the core valence band. With this assignment, the PL kinetics indicate that there are more traps having slower hole tunneling times to the core in the particles having thicker shells.

We can assume that at the blue excitation wavelength used here (423 nm) the holes quickly become localized in either the core or the shell and this localization to some extent persists as hole cooling proceeds. In this case, it follows that excitation into the ZnSe shell will result in a larger probability of hole trapping than excitation into the InP core. If we further assume that the trap density in the ZnSe shell is uniform (independent of shell thickness or distance from the core), it follows that the total number of traps should scale with the total shell volume. (Further discussion of this assumption follows, below.) With these assumptions, it follows that the fractional magnitude of the slowly rising component of PL kinetics should be proportional to the fraction of nascent holes

produced in the shell and therefore should scale linearly with the fraction of the QD absorbance due to the shell. This fraction is given as $f_{SA} = \alpha_{ZnSe}V_S/(\alpha_{ZnSe}V_S + \alpha_{InP}V_C)$, where V_S and V_C are the shell and core volumes, respectively, and α_{ZnSe} and α_{InP} are the respective 423 nm bulk material absorption coefficients. Such a plot is shown in figure 3.5A.

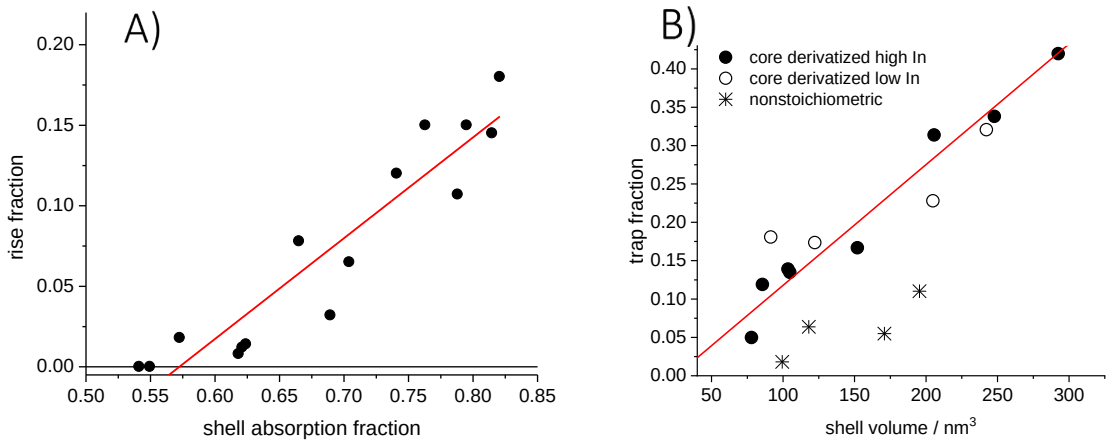

Figure 3.5: A) Plot of the fraction of slow PL risetime of the core-derivatized QDs as a function of the fraction of 423 nm photon cross section due to the ZnSe shell. Also shown is a linear fit to the data having an x-intercept of 0.57. B) Fraction of the thermally equilibrated hole population in trap states as a function of shell volume for the nonstoichiometric and core-derivatized QDs having high and low excess indium concentrations, as indicated. A linear fit through the core derivatized data points is shown, having an x-intercept of 25 nm^3.

The fraction of the hole population in these states is given by $f = 1 - \tau_0/\tau$, where τ and τ_0 are the measured PL and intrinsic radiative lifetimes, that is, the lifetimes in the presence and absence of the traps, respectively. A plot of this fraction as a function of shell volume for the nonstoichiometric and core-derivatized QDs is shown in figure 3.5B. At equilibrium, the thickest shell QDs (specifically, CD-2.28, CD-2.51, CD-2.54 and CD-2.72) have about 35% of the hole population in traps and 65% in the valence band. These QDs show about 23 - 25% slow rise component, with the remainder of the PL appearing promptly. The product of the equilibrium fraction of the holes in the valence band and the fraction of the PL that appears immediately gives the overall fraction of the holes that initially cool directly to the valence band. We conclude that in the above QDs having the thickest shells, about 50% relax directly, and the other 50% of the holes initially cool into traps. Hole tunneling then tends toward the valence band until stabilizing at the final equilibrium value.

The analysis of hole dynamics reveals that while traps located in much of the inner part of the ZnSe shell may be involved in hole trapping, their fast-tunneling times do not significantly contribute to the observed risetime in the photoluminescence (PL) kinetics. Figure 3.5A illustrates that no observable risetime is evident when the fraction of the shell absorbance is less than approximately 57% at the 423 nm excitation wavelength. The x-intercept of 0.57 in figure 3.5A corresponds to the shell thickness of the thinnest ZnSe shells in the core-derivatized series, approximately 1.3 nm.

Consequently, it is concluded that long-lived hole trapping (greater than about 40 ps) occurs primarily for traps situated in the region of the shell that is more than about 1.3 nm (equivalent to approximately 4.5 ZnSe monolayers) away from the core.

The hole tunneling times exhibit a rapid increase with increasing distance between the trap and the core, which explains why very long tunneling times are observed only in the QDs with the thickest shells. This behavior can be understood through effective mass approximation calculations of the valence band hole wavefunction.[11] These calculations indicate that the wavefunction amplitude decays exponentially close to the shell, with a characteristic decay length of about 0.28 nm (approximately 1 ZnSe monolayer). Consequently, hole tunneling times are expected to increase exponentially with the number of ZnSe monolayers separating the trap from the core. For instance, a trap located one monolayer closer to the core would exhibit a tunneling time approximately 7.39 times faster, or about 5.5 ps, which would be indistinguishable from the instrument limited response with the present time resolution.

This analysis highlights that there may be a significant fraction of traps closer to the core, but their rapid tunneling times render them undetectable with the ~40 ps time resolution employed in the study. It's noteworthy that this simple model predicts very long tunneling times for traps situated close to the shell's outer interface, exceeding several nanoseconds. However, such extended tunneling times are not observed in the PL kinetics, where the longest components are on the order of 1-2 ns. The simple model does not account for trap-to-trap tunneling, which may be relevant for the slowest trap-to-core tunneling times. Trap-to-trap mobility is a well-known phenomenon and has been analyzed in terms of direct and superexchange mechanisms.[14]

As discussed earlier the equilibrium formed between the trap states and the valence band fine structure states shown in figure 3.6A lead to a decrease in the population of holes in the emitting ($\pm 1^{L}$) state. This leads to significant increases in the observed radiative lifetime. In the case of the largest QDs the increase in observed radiative lifetime between the stoichiometric and core derivatized particles is upwards of 50% as shown in figure 3.6B. The difference in the contribution of trapping to the observed radiative lifetime between the core derivatized and nonstoichiometric QDs can be understood in terms of the radial distribution of these traps which is determined in large part by the core/shell interface. This radial distribution will be elucidated further in chapter 4.

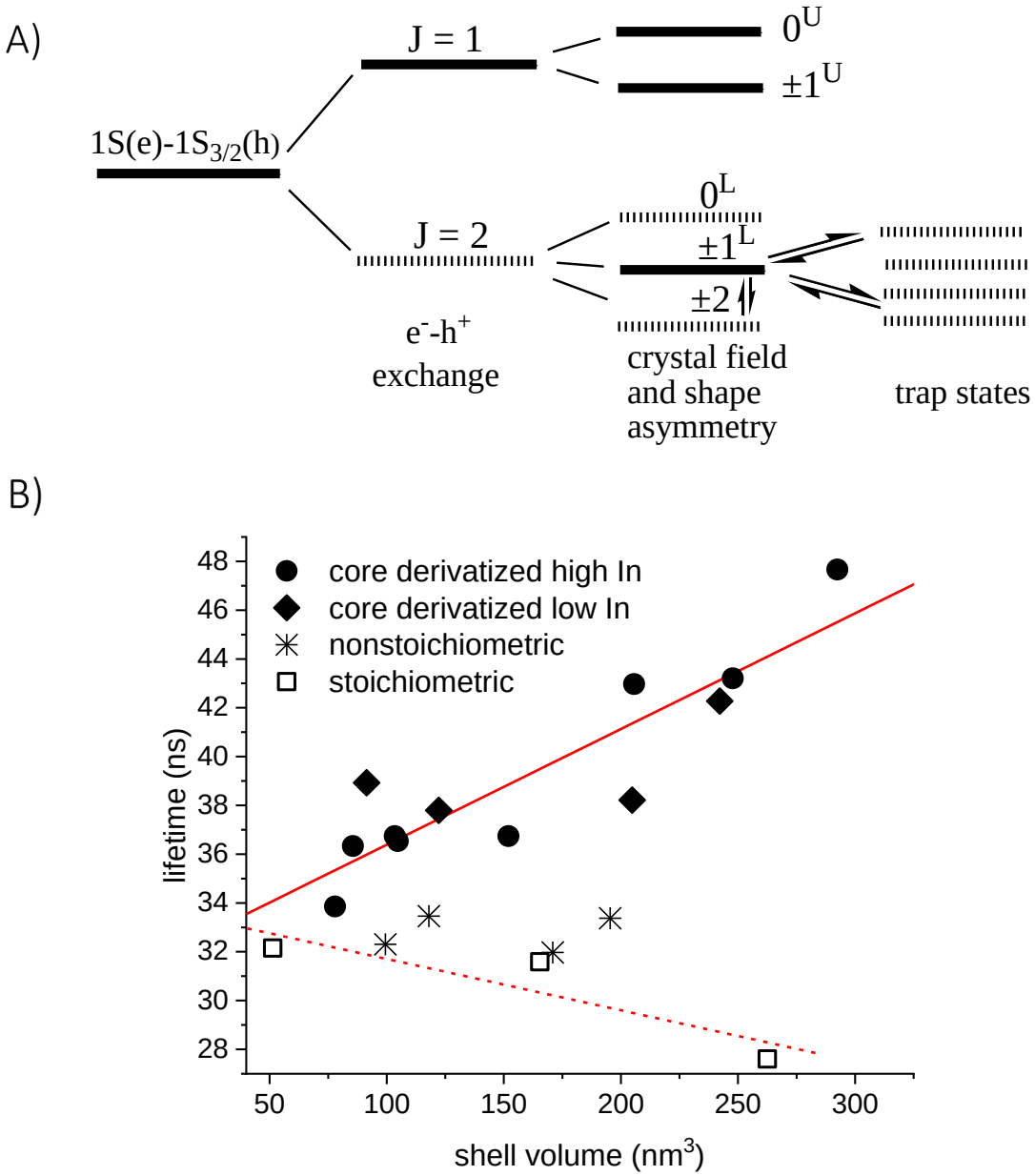

Figure 3.6: A) Angular momentum fine structure energy levels of the lowest exciton in II-VI and III-V QDs. Optically allowed (forbidden) levels are indicated with solid (dotted) lines and are in equilibrium with the bright $\pm 1^L$ state.[1,6] Also indicated are the hole trap states in equilibrium with the bright exciton state, which is specific to InP/ZnSe QD having indium dopants in the ZnSe shell. B) Radiative lifetimes of the stoichiometric (open squares), nonstoichiometric (stars) and core derivatized (high indium, closed circles and low indium, closed diamonds) QDs as a function of ZnSe shell volume. Also shown are linear fits to the core derivatized QDs (solid red line) and the stoichiometric QD (dashed red line) lifetimes. These lines intersect at a shell volume of 33 nm^3.

In order to function as transient traps these trap states must exist in between the InP core valence band level and the ZnSe shell valence band level. From the model in figure 2.4 it follows that trap to valence band tunneling should be more energetically favorable when the interfaces have more Zn/P character, that is, when PL detection is on the red edge of the PL band. The more energetically favorable hole transfer reaction would be expected to proceed faster, reducing the time constant and/or apparent amplitude of the slow rise component. Figure 3.7B shows that this predicted difference across the PL band results in small, but easily observed differences in the PL kinetics of the CD-2.72 particles. As seen in figure 3.7, the blue edge gives a significantly slower PL risetime. With 600 and 648 nm detection, we get the risetimes and amplitudes indicated in the aforementioned figure.

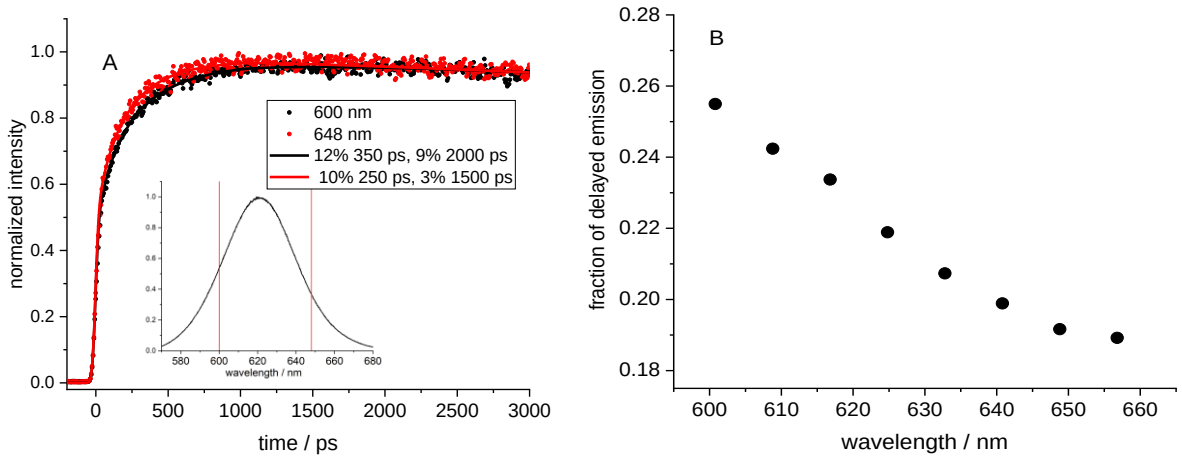

Figure 3.7: A) Rise kinetics obtained in the red (648 nm) and blue (600 nm) regions of the CD-2.72 QDs PL spectrum, as indicated in the inset. The kinetics are fit to a fast (instrument limited) component and slower biphasic risetime. The fitting risetimes and amplitudes are indicated in the figure. A faster rise is observed on the red edge of the PL spectrum. B) Measured fraction of the total PL that occurs as delayed emission as a function of detection wavelength for the CD-2.72 QDs.

In references[10,15] the kinetics of delayed emission associated with holes having an equilibrium between the core-localized valence band and the shell-localized trap states were measured. The radiative lifetime of these QDs is about 30 ns, and the delayed emission is defined as having a decay time of greater than 75 ns. As depicted in figure 3.7, this equilibrium favors a larger fraction of the hole population being in the traps in the case of the dominantly In/Se interface, that is, on the blue edge of the PL spectrum. This is shown by the fraction of delayed PL as a function of detection wavelength and that the variation predicted by the model in figure 2.4 is observed.

The band offset model introduced in chapter 2 has allowed for a complete interpretation of the complex and counterintuitive trap dynamics of the low fluence TRPL decay. The introduction of indium based transient hole traps in the shell creates both slow rise and delayed emission. This delayed emission can increase the observed radiative lifetime of these particles by up to 50%, which in turn has a large impact on the durability of these QDs as they are subjected to higher and higher fluences. Biexcitons formation rates in devices scale with the radiative lifetime, and as such this trapping has a direct effect on device stability.

3.4 Biexcitons and Trions

When there are more carriers in a single QD than an electron hole pair, trions and biexcitons can be formed. Trions come in two types: negative and positive. In a negative trion (T^-) the QD has two electrons in the conduction band and a single hole in the valence band. Conversely a positive trion (T^+) has two holes in the valence band and a single electron in the conduction band. If a QD has both two electrons in the conduction band and two holes in the valence band this is referred to as a biexciton (XX). For both trions and biexcitons the primary recombination pathway is Auger recombination. In Auger recombination an electron and hole recombine nonradiatively, and instead of emitting a photon, the energy is transferred to the remaining charge carriers. This leads to charge carriers with energies well beyond the band gap of ZnSe/ZnS or most other shell materials. These processes are diagramed in figure 3.8. Charge carriers with energy well outside of the band gaps of the shell materials are colloquially referred to as “hot” carriers. While in the field of semiconductors “hot” carriers refers to any carrier outside of a thermal Boltzmann distribution, we will use the term here to refer to carriers with energies of ~2 eV above their respective band edge.

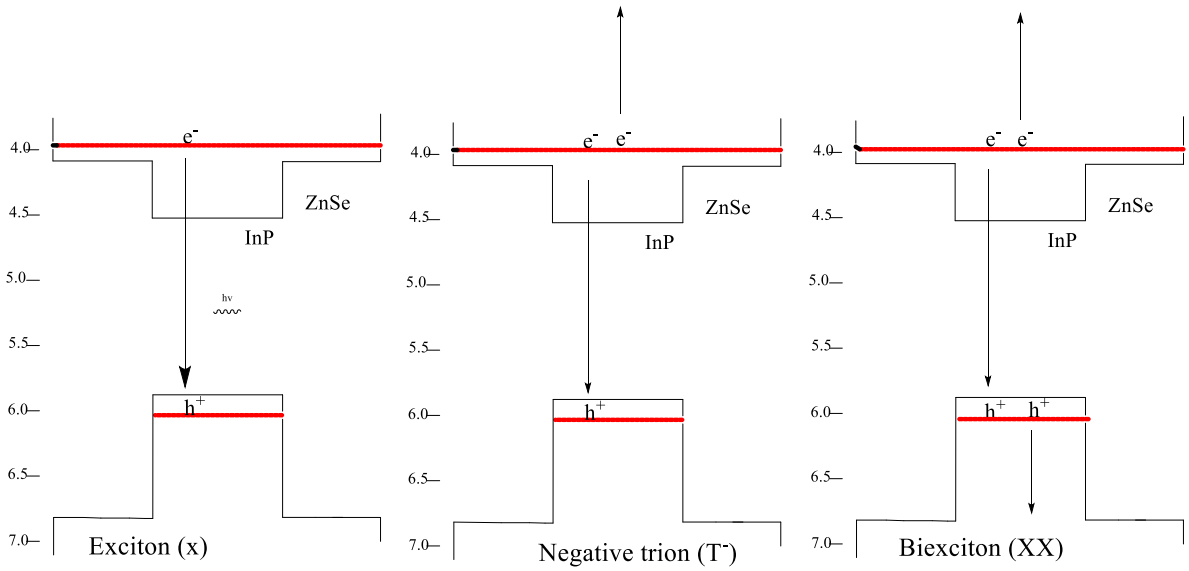

Figure 3.8: Diagrams showing the number of carriers, and whether there are “hot” carriers produced for an exciton, negative trion, and biexciton.

Trion dynamics have important implications for the design of electroluminescent devices. These devices use a current to inject electrons and holes into QDs instead of relying on absorption of higher energy photons. When a positive voltage is applied to the device, this voltage helps to push holes from the anode (positive electrode) toward the quantum dots. The injected holes accumulate in the valence band of the quantum dots. When a negative voltage is applied to the device, electrons are pulled from the cathode (negative electrode) toward the quantum dots. These injected electrons accumulate in the conduction band of the quantum dots. Any imbalance in the rate at which electron and holes are injected into the QD can lead to the formation of trions, and control over the injection rate can help determine which flavor of trion is formed. Due to trions recombining primarily nonradiatively through Auger recombination an imbalance in the injection rates can significantly decrease the electroluminescence quantum yield (ELQY) and device lifetime.

In addition, there are consumer lighting applications for which the intensity of incident light on QDs in a device leads to absorption outpacing emission. This can occasionally cause QDs to absorb a second photon before the emission of the first photon leading to the formation of a biexciton. This has significant implications for InP based QDs intended for high flux applications compared to those intended for low flux applications. Unlike Auger recombination of trions, where there is only one “hot” carrier, in biexciton Auger recombination both of the carriers have the potential to be “hot.” The odds of Auger recombination producing a “hot” electron or “hot” hole is referred to as the Auger branching ratio.

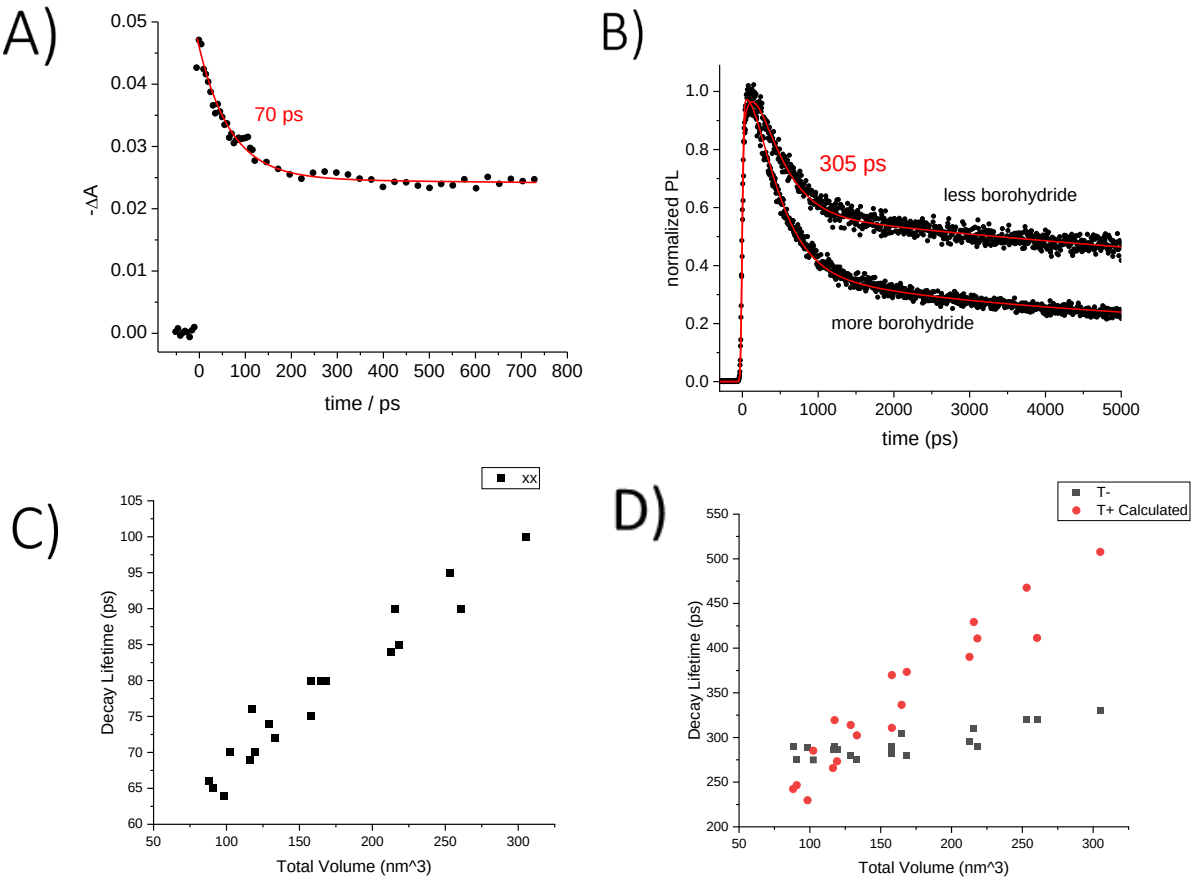

Figure: 3.9 A) TA decay of S-2.51 B) Photobleached TCPC decay for NS 2.01. Plots of C) biexciton and D) trion Auger rates for a variety of InP QDs.

To determine the biexciton Auger recombination rate a combination of transient absorption (TA) and time-resolved PL spectroscopy were used. Because of the higher time resolution (limited only by the femtosecond pulse width), TA spectroscopy is most commonly used to measure the Auger dynamics in ensemble samples of semiconductor QDs. It is limited by a significantly lower rep rate, and a significantly lower signal to noise. Despite the lower time resolution (typically 30 – 90 ps), time-correlated single-photon counting (TCSPC) PL spectroscopy can also be used to measure these dynamics in all but the most rapidly relaxing QDs. TCSPC has a significantly higher rep rate and an arbitrarily high signal to noise. The combination of these two methods gives unique fits for the biexciton Auger rate. Fits of the kinetics measured through both TCPC and TA show a single exponential decay of the biexcitons, with a time constant of 60 – 100 ps varying with shell volume as shown in figure 3.9 C.

In the study of single exciton and biexciton recombination rates, various types of carrier traps can play significant roles. Carrier localization and trapping can influence biexciton dynamics. In core/shell QDs, lattice strain is inherent due to the core/shell structure, which can lead to defects at the interface. The presence of these defects adds

complexity to the understanding of Auger dynamics at either sharp or graded interfaces. Researchers, such as Beane et al., have employed TA spectroscopy to investigate the impact of hole localization or partial trapping at the core/shell interface in CdSe/ZnSe nanocrystals. [13] Their findings suggest that interfacial hole trapping can have substantial effects on biexciton Auger dynamics. In addition, surface traps, often caused by incomplete ligation during QD synthesis, are among the most common forms of carrier traps. Dopants can also lead to carrier trapping. [14-15] Despite the potential presence of these traps, the PLQY of the samples studied here are very high, usually exceeding 90%. This high QY indicates that these samples do not experience significant contributions from surface or interfacial traps which would act as electron-hole recombination centers.

The negative trion lifetimes shown in figure 3.9B and D were determined by TCPC experiments performed on photobleached samples. In this experiment a QD sample is titrated with small amounts of lithium borohydride. After a QD is excited lithium borohydride can donate an electron into the hole left in the valence band, leaving an electron in the conduction band, and negatively charging the QD. Further excitations while that electron is in the conduction band will lead to the formation of negative trions. These negatively charged QDs are stable for tens of minutes before recovering. The extent of photobleaching can be determined through an absorption experiment by measuring the decrease in absorbance of the $1S_{3/2}$-$1S_e$ and the $1S_{1/2}$-$1S_e$ transitions. Due to the conduction band state filling a negatively charged QD will have roughly half of the transition strength of the uncharged QD for transitions including the $1S_e$ envelope function. This was discussed in chapter 2 and shown in figure 2.5.

In the photobleached TCPC experiment, there is a long-lived component that matches that of the unreduced QDs. In addition, there is a dominant 250-300 ps decay component, having an amplitude that increases with the amount of added borohydride as shown in figure 3.9B. This component is assigned to the trion lifetime. There is a slower, very small (a few percent of the total) transient of about 3 – 4 ns that also increases with the amount of added borohydride. This component is assigned to borohydride quenching of the uncharged excited state QDs. There is also a small decay component of about 50 ps that is typically about 10% of the total and increases with borohydride concentration more rapidly than does the dominant 250-300 ps component. This component is assigned to multiply charged QDs. Throughout these studies, the concentration of borohydride is chosen to give a relatively large 250 – 300 ps decay without getting too much of the ~ 80 ps component. Similar measurements have been made on several different stoichiometric, nonstoichiometric, and core derivatized QDs. The results in figure 3.9D show that a linear correlation between the trion Auger time and the total particle volume is obtained. This makes good sense in terms of the volume scaling of the overlap integral of a QD with the conduction band electrons delocalized over the entire InP/ZnSe structure as was shown in the previous chapters. This is similar to CdSe/CdS, for which k_{T-} and k_{T+} have been independently measured as a function of core diameter and shell thickness.[16]

The radiative rates are calculated using the Einstein relations connecting the absorption cross section to the radiative rate as described earlier in the chapter.[3–5] This calculation uses the calculated neutral QD, trion and biexciton relative oscillator strengths, and requires an accurate determination of the lowest exciton extinction

coefficients to determine the oscillator strength for the QD → X transition.[1,5–7,17] Evaluation of these rates gives the radiative lifetimes of XX and T^- as 1.25 and 2.5 ns, respectively. As shown in figure 3.9C and D, the timescales for the biexciton and trion Auger process are less than 100 and several hundred picoseconds, respectively. This is much faster than the calculated radiative lifetimes. As such, subtraction of the radiative rate from the measured biexciton and trion decay times is a small correction and is ignored in this treatment.

(Eq 3.5)	$XX \rightarrow X$	k_{XX}	(biexciton Auger)
(Eq 3.6)	$XX \rightarrow X + h\upsilon$	$k_{rxx} \sim (1.25\ ns)^{-1}$	(biexciton radiation)
(Eq 3.7)	$T^- \rightarrow QD^-$	k_{T-}	(trion Auger)
(Eq 3.8)	$T^- \rightarrow QD^- + h\upsilon$	$k_{rT-} \sim (2.5\ ns)^{-1}$	(trion radiation)

Positive trions have been demonstrated in the literature, but universally have been shown to be immediately and largely irreversibly detrimental to the photostability of the QD.[18] This makes direct measurement of the positive trion Auger time difficult. However, to a good approximation, we can take the overall biexciton Auger rate to be a sum of electron and hole Auger rates, i.e., negative and positive trion rates, $k_{XX} = 2(k_{T-} + k_{T+})$, or alternatively stated in terms times, $1/\tau_{XX} = 2(1/\tau_+ + 1/\tau_-)$ where τ_{XX}, τ_+ and τ_- are the biexciton, positive trion and negative trion Auger times, respectively.[19] We note that the fraction of electron excitation in the biexciton Auger process is given by $f_e = \tau_+/(\tau_+ + \tau_-) = 2\tau_{XX}/\tau_-$ and that the fraction of hole excitation can then be written as $f_h = 1 - f_e$. The values of $1/k_{T+}$ shown in figure 3.9D are only for cores with diameters of approximately 2.9 nm. The biexciton and trion Auger recombination rates are size dependent, and that causes calculated electron f_e and hole f_h excitation fractions to also be size dependent as is shown in figure 3.10.

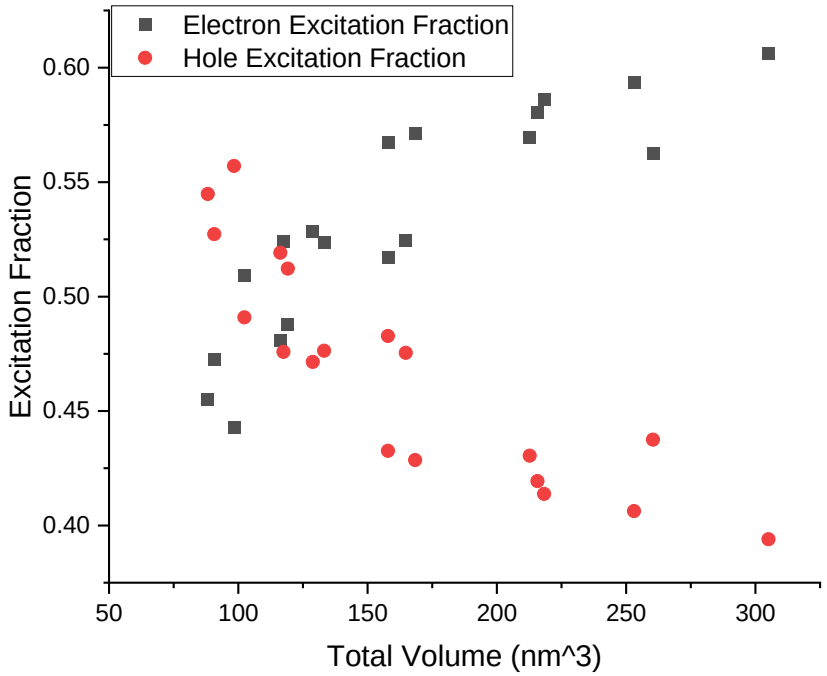

Figure 3.10: Ratio of hot carrier creation calculated from the relative contributions of negative and positive trions to the biexciton Auger rate.

In addition to the Auger recombination rates, the energetic position of the biexciton and trion bands are of interest. In an analogous fashion to the spectral reconstruction used in chapter 2 for determination of FRET, spectral reconstruction can be performed on trion and biexciton TRPL spectra shown in figure 3.11A-B. In figure 3.11B the sample is excited with fluences that generate large numbers of biexcitons (roughly 1/2 -2/3 of the emission amplitude). After the first nanosecond of the decay all of the biexciton processes have resolved and the spectral reconstruction matches that of the single exciton. However, for the first hundred picoseconds the biexciton makes up the majority of the signal and redshifts the emission spectrum. The central limit theorem allows for calculation of the biexciton emission maximum. The complimentary TA experiment for determining these bands shown in figure 3.11C is complicated by the stimulated emission (S.E.) from the fully allowed XX and negative trion emissive state.

An analogous TA experiment can be performed with a photobleached sample to determine the emission of the negative trion. However, the low repetition rate of the TA experiment makes the required time to take the measurement long compared to the stability of the photobleached sample. This limits the negative trion measurements to TRPL and prevents easy determination of the energetic position of the negative trion states.

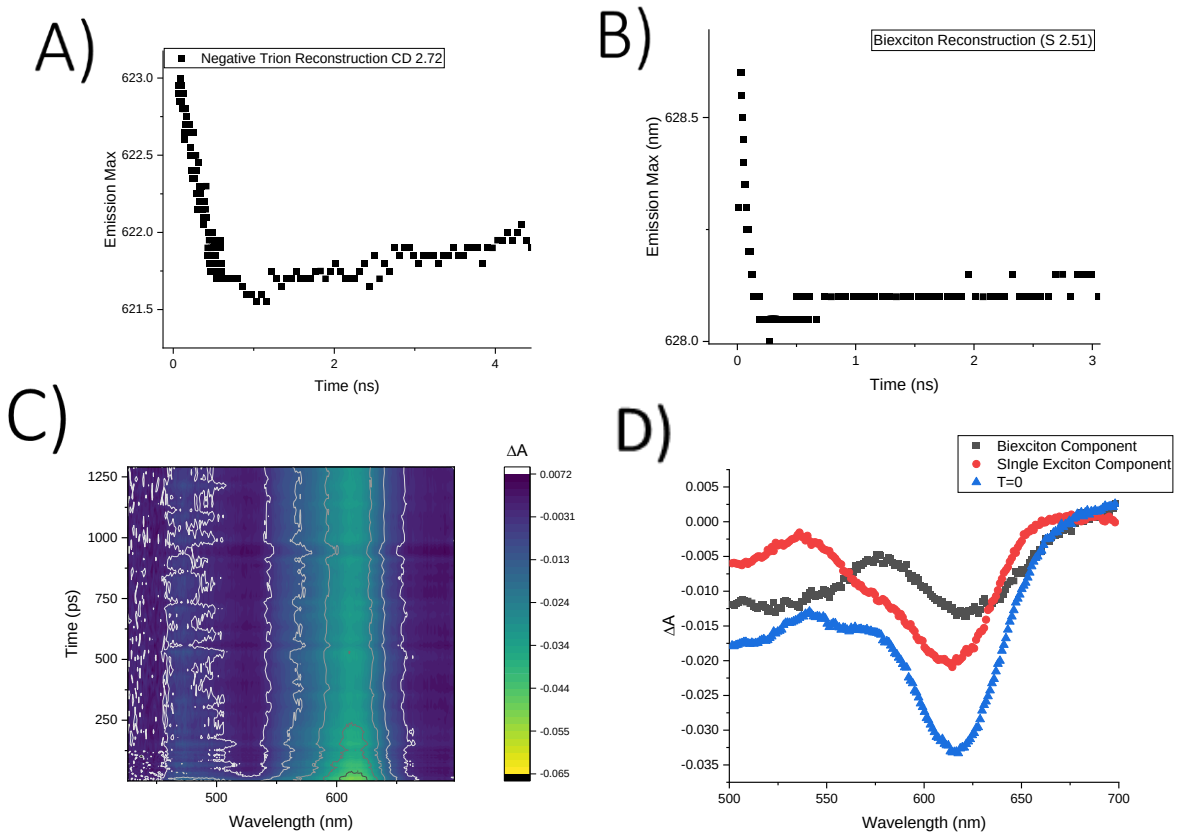

Figure 3.11: A) spectral reconstruction showing the shift in emission maximum due to the contribution of emission from the negative trion. B) Spectral reconstruction showing the shift in peak maximum due to emission from the biexciton under high flux. C) Transient absorbance experiment showing the overall change in absorbance over 1.3 nanoseconds. D) Relative contribution of recoveries from time components assigned to the biexciton and single exciton to the t=5 ps transient absorbance spectrum.

The TRPL experiments are rather straightforward to interpret and allow for accurate determination of the emission wavelength of the negative trion even at relatively low concentrations. Figure 3.11A demonstrates a small redshift that has been well documented in the literature. This redshift is referred to as the trion binding energy. TRPL of the biexciton is also easy to interpret in theory, however in practice the sub-hundred picosecond time scale makes accurate determination of the emission band significantly more difficult. TA is even more difficult to interpret due to the contribution of absorbing transitions and stimulated emission of the excited states.[10,20–23]

In the TA measurement shown in figure 3.11C-D there are three species of QDs present; unexcited QDs (G), singly excited QDs(X), and doubly excited QDs (XX). In the ground state there is no stimulated emission, and the transitions are all G-X. This forms the background. At long times (>100ns) the transient absorbance spectrum will fully decay back to the ground state, giving a difference spectrum of zero at all wavelengths. The singly excited state is more complex. First, for the population that is excited, the G-X

transitions have been replaced with X-XX transitions. In addition, there is now a small stimulated emission (S.E.) contribution from the X-G transitions.

For the population that has been doubly excited, those in a biexciton state, the $1S_e - 1S_{3/2}$ and $1S_e - 1S_{1/2}$ regions are fully bleached and do not have any further absorbance transitions. Therefore, the only XX state contribution at the band edge is the XX-X S.E. transition. Interpretation of these complex summed signals becomes identifiable due to the large differences in the decay constants of the constituent QD species. The biexciton has been shown to decay on the 100ps timescale, while the exciton decays on the order of 40ns. On the timescale of the biexciton decay, the single exciton decay can be taken to be constant. In addition, it is important to assume that all electrons and holes cool to the Boltzmann equilibrium determined lowest energy states at time constants fast compared to the instrument timescale (~1ps). This is reasonable, as electron and hole cooling processes in this system have been shown to be a few picoseconds.[1]

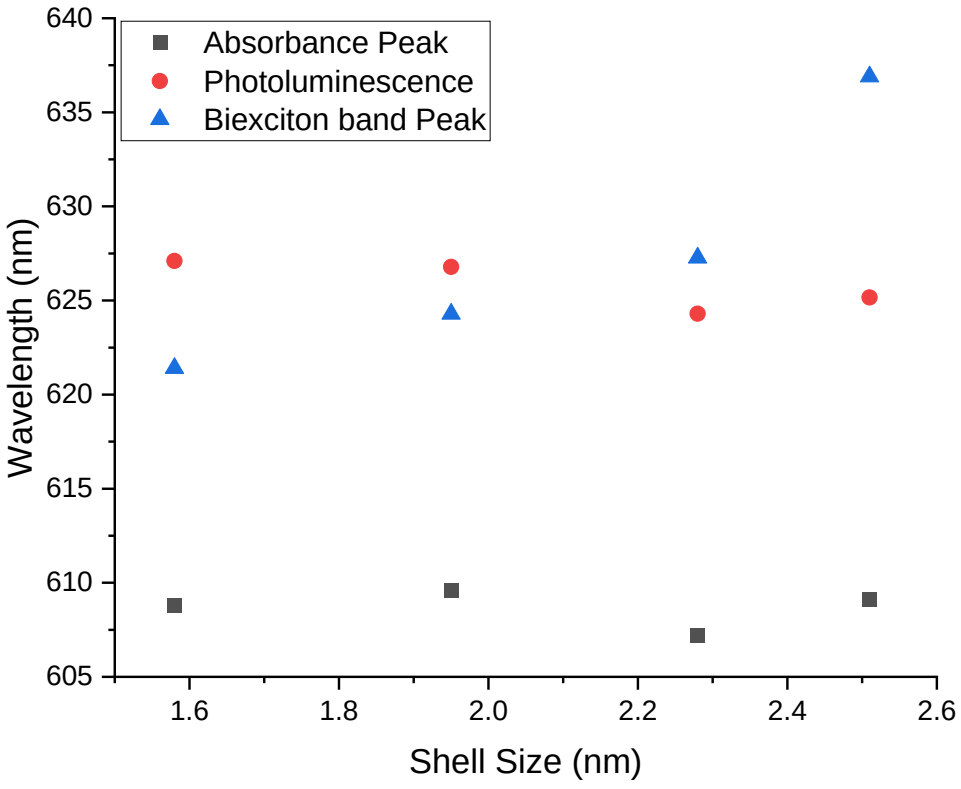

Figure 3.12: The relative position of the peak wavelength of the "biexciton band" determined by the TA experiment as a function of shell size compared to the low flux absorbance and emission peaks.

At times shortly after the pump has arrived all cooling processes are complete and our population of G, X, and XX state QDs has been prepared. If we take this t=5 ps difference spectrum to be our baseline, then on the timescale of 100 ps two processes occur. As doubly excited QDs decay they create X state QDs. As this process occurs stimulated emission from the biexciton decreases linearly with population. In addition, single excitons are formed, and X-XX transitions appear along with the corresponding X-G stimulated emission. These two changes both allow less light through and appear as an increase in absorbance. Therefore, the difference between t=1 ps and t=100 ps corresponds to three features: the XX-X S.E. the X-G S.E. and the X-XX absorption bands. In addition to this, the weaker transition strengths should cause the X-G S.E. to be a significantly lower relative contribution than the XX-X state S.E. Untangling these complex contributions is difficult without a large set of assumptions. However, the position of the band-edge peak with the time constant corresponding to the biexciton Auger time can be assigned as a combination of equal parts X-XX absorbance and XX-X S.E. from the biexciton. The peak that is observed for this feature is narrow, with a similar width to the absorbance of the lowest G-X transition. This suggests that the X-XX absorbance and XX-X S.E are very close in energy and an approximation of the biexciton binding energy. This is shown in figure 3.12 in which the position of this biexciton band is plotted relative to the ground state absorbance and excited state luminescence. This binding energy affects the energetic favorability of forming a biexciton and likely contributes significantly to the biexciton formation rate. The interpretation performed here ignores many factors that complicate this spectroscopy such as spectral shifts due to stimulated emission and the contribution of absorbance and stimulated emission to each species of QD in the TA spectrum. However, it lays the groundwork for further study of the energetics of biexcitons and trions.

As discussed earlier the formation and ejection of “hot” carriers is the primary degradation pathway of QDs under high fluences. This section has shown that the likelihood of a biexciton being created and the ratio of “hot” electrons and “hot” holes is modulated by shell size. QDs with thicker shells are more likely to form biexcitons and those biexcitons are more likely to create “hot” electrons. Both of these factors are important considerations when designing QDs for device applications. This section has lightly explored the effect of core and shell size on the energetic favorability of forming a biexciton which is an underexplored area in InP/ZnSe with large implications on device stability.

3.5 Biexciton Trap Dynamics

Following the exploration of the role of traps in single photon dynamics found in section 3.3 one may question to what extent these transient trap states contribute to the photophysics at biexciton fluences. To begin, one can perform the comparison of a stoichiometric QD and a core derivatized QD with roughly equivalent cores and shell volumes in both TA and TCPC. These experiments show that samples with trapping contributions to the single photon decay also show trapping contributions in the biexciton lifetimes. The biexciton Auger recombination component can no longer be fit to a single exponential, and instead must be fit to a biexponential as shown in figure 3.13B. One

component of this biexponential has an Auger recombination rate that matches the comparable stoichiometric QD, however it also has a component that is nearly 4 times slower. This component has a slower Auger recombination rate than the negative trion and scales proportionally to the biexciton amplitude with changes in fluence.[24] We assign the former component which exists in both stoichiometric and non-stoichiometric QDs to biexcitons having both holes in the InP core (XX state) and we assign the latter component as biexcitons which have one hole trapped in the ZnSe shell (XT state) as shown in figure 3.13A.

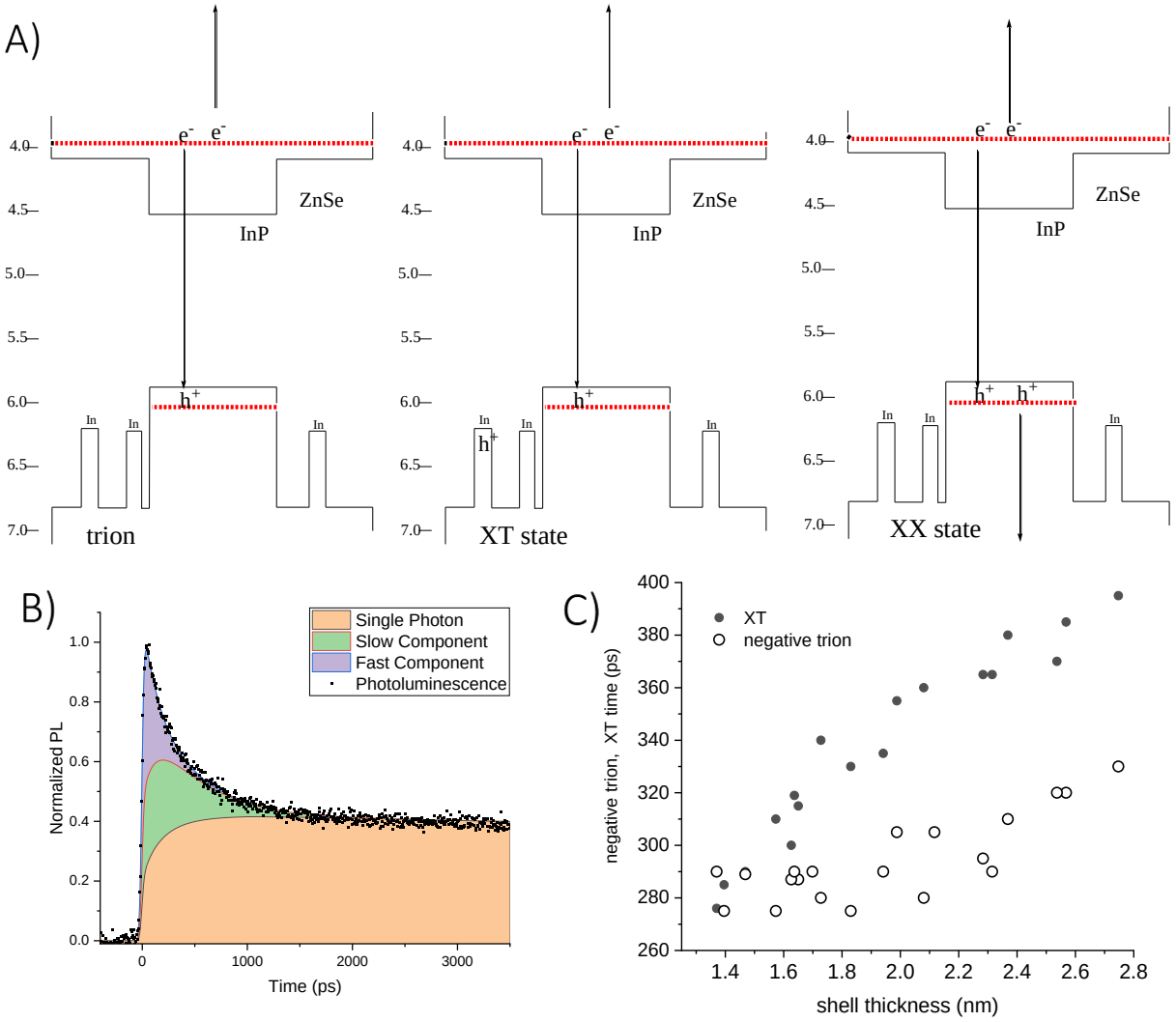

Figure 3.13: A) Energy level diagram and electron and hole dynamics in the negative trion XT and XX states. B) Cartoon showing the contributions of the XX and XT states to the first 4 ns of a TCPC decay curve. C) Comparison of the negative trion times (open circles) and the XT state decay times (filled circles) as a function of ZnSe shell thickness.

At wavelengths higher in energy than the stimulated emission of the contributing states the magnitude of the TA bleach depends primarily on conduction band state filling.[20,21,23] Both the XX and XT states have two conduction band electrons and therefore result in bleach magnitudes that differ only by the magnitude of the exciton

absorbance. This difference is given by the square of the electron-hole overlap integral. The situation is slightly more complicated for PL kinetics. The intensity of the PL, and hence the amplitude of the PL decay component, depends on the oscillator strength of the optical transitions involved in the luminescence. The XT state has only one valence band hole, compared to two in the XX state. This situation has been analyzed in papers by Efros et al.,[25,26] and the conclusion is simple: the presence of two valence band holes in the XX state gives it a factor of 2 larger oscillator strength compared to the negative trion, which is analogous to the XT state. This factor of 2 difference in the oscillator strength predicted by Efros et al. should only differ by changes in electron-hole overlap caused by the presence of the trapped hole. The trapped hole in the shell produces an electric field that perturbs the conduction band electrons and the remaining valence band hole. Thus, the different valence band occupancies and different electron-hole overlap integrals result in transitions involving absorption and PL of the XX and XT states having different oscillator strengths. These effects can be quantified, allowing the determination of the XT state fraction from the PL and TA kinetics, which can then be compared. The TA biexciton bleach recovery kinetics and PL biexciton kinetics are given by;

$$-\Delta A(t) = const \cdot \left(P_{XX} \exp(-t/\tau_{XX}) + P_{XT} K_{XT} \exp(-t/\tau_{XT}) \right) \quad \text{(Eq 3.9)}$$

$$I(t) = const' \cdot \left(2.0 P_{XX} \exp(-t/\tau_{XX}) + P_{XT} K_{XT} \exp(-t/\tau_{XT}) \right) \quad \text{(Eq 3.10)}$$

P_{XX} and P_{XT} are the XX and XT state populations, respectively, and K_{XT} is the square of the ratio of XT and XX electron-hole overlap integrals. The presence of two valence band holes in the XX state and only one in the XT state gives a factor of 2.0 in the biexciton radiative rate. The unperturbed overlap integral is defined as $S^2 = \left| \left\langle \Psi_{1S_e} \middle| \Psi_{1S_h} \right\rangle \right|^2$, and in terms of this quantity, the perturbed overlap integral is then given by $\left| \left\langle \Psi_e \middle| \Psi_h \right\rangle \right|^2 = S^2 K_{XT}$. The fraction of the slow components seen in the TA and PL experiments, F_{TA} and F_{PL}, respectively, are given by;

$$F_{TA} = \frac{P_{XT}}{P_{XX}/K_{XT} + P_{XT}} \quad \text{(Eq 3.11)} \qquad F_{PL} = \frac{P_{XT}}{(2.0/K_{XT})P_{XX} + P_{XT}} \quad \text{(Eq 3.12)}$$

We can define the fraction of biexciton XT states formed, $f = P_{XT}/(P_{XX} + P_{XT})$, which can be written in terms of F_{TA} and F_{PL}.

$$f = \frac{(1/K_{XT})F_{TA}}{1 + (1/K_{XT} - 1)F_{TA}} \quad \text{(Eq 3.13)}$$

$$f = \frac{(2.0/K_{XT})F_{PL}}{1 + (2.0/K_{XT} - 1)F_{PL}} \quad \text{(Eq 3.14)}$$

K_{XT} is the amount that the trapped hole changes the extent of electron-hole overlap. From a comparison of the XT and negative trion recombination rates for the red QDs, the presence of the trapped hole reduces the extent of electron-hole overlap and thereby increases the radiative lifetime by about 15%-20%. To the extent that the Auger rate scales with the electron-hole overlap, the ratio of XT state and negative trion rates corresponds to the values of K_{XT}. However, the relationship between the negative trion and XT recombination rates is not constant in thin shells. This suggests the presence of another XT state quenching process in the thinnest shells. It is proposed that the observed shorter XT state lifetimes in these shells are due to hole tunneling from the XT state to the XX state, effectively quenching the XT states. The hole tunneling time from XT to XX states is estimated to be on the order of 2 nanoseconds in the case of the thin-shelled red QDs, which is not observed in QDs with thicker shells.[24] This indicates that significant tunneling occurs primarily from traps located close to the core-shell interface.

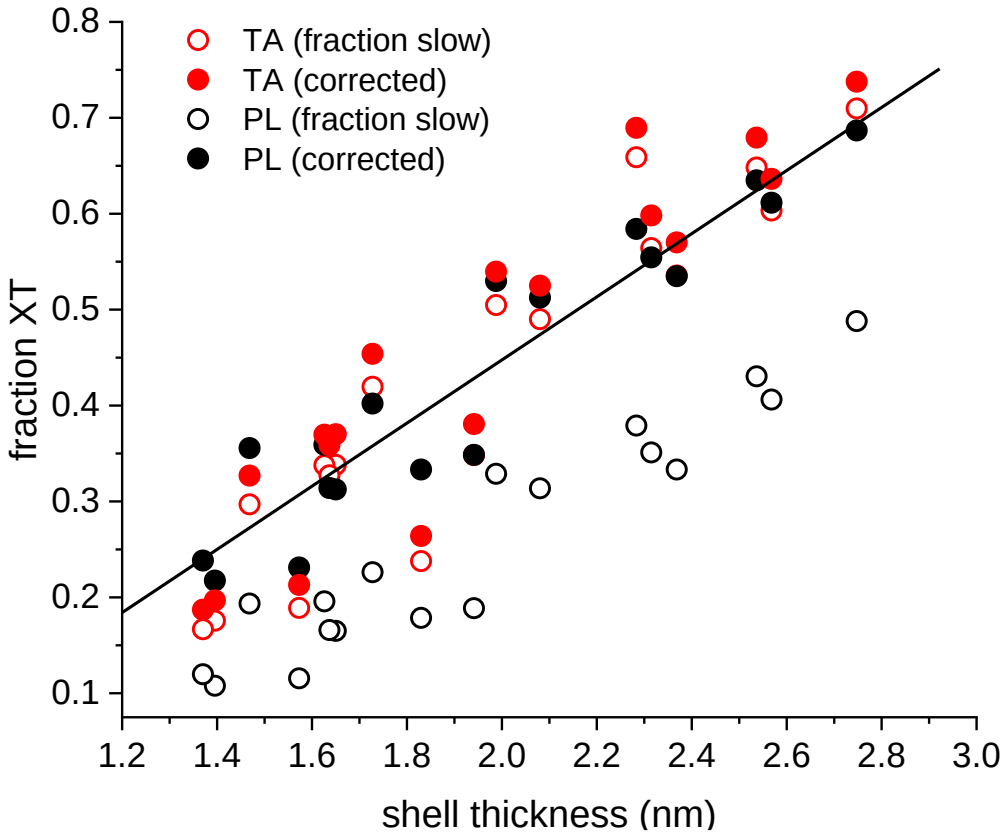

Figure 3.14: Fraction of the biexciton decay that is in the slow component from the TA (open red circles) and PL (open black circles) measurements as a function of shell thickness. The black line is a linear fit to the PL fraction and gives an x-intercept of 0.64 ± 0.08 nm. Evaluating equations 3.11 and 3.12 gives the initial fraction of the population in the XT state from TA (solid red) and from PL (solid black). We conclude that applying these corrections to the TA and PL data brings them into agreement.

A line fit through the photoluminescence data in figure 3.14 suggests that QDs with ZnSe shells thinner than approximately 0.64 nm (equivalent to about two ZnSe monolayers) would have no XT state population. This observation can be explained by considering the penetration of the valence band wavefunction into the shell. It implies that any hole trap within the first two monolayers of the shell is sufficiently coupled to the valence band, preventing the observation of XT states in these QDs.

Comparison of the negative trion and XT times in QDs with smaller core sizes shown in figure 3.13C are consistent with this explanation. The extent to which the hole wavefunction is delocalized into the ZnSe shell decreases with increasing core size and exciton wavelength. Thus, the smaller core QDs have greater valence band extension into the ZnSe shell than the larger core QDs. More quantitatively, the amount of the valence band delocalization into the shell is given by:

$$\text{(Eq. 3.15)} \quad f_h = \int_{r_c}^{r_c+h} \left|\Psi_h\right|^2 4\pi r^2 dr$$

where r_c is the core radius and h is the shell thickness. Calculated values of f_h are 0.0475, 0.0654, and 0.0831 calculated for the 2.9 nm, 2.56 nm, and 2.32 nm diameter cores, respectively, reflecting the observed trend in XT tunneling times.[24]

The observed exciton PL risetimes and the XT → XX relaxation both correspond to trap to valence band hole tunneling. The PL risetimes increase with increasing core size, increasing from ≈ 50 ps for the 2.32 nm core, to ≈ 1 ns for the thickest shell 2.9 nm core QDs.[10,11] These values can be compared to the XT → XX times estimated above (330 ps to ≥ 2 ns), and we note that these times are approximately a factor of 3 – 6 slower. Simple tunneling theory gives charge transfer tunneling rates that vary with the barrier height and width,[28]

$$\text{(Eq. 3.16)} \quad k_{CT} \propto \exp\left(-2\beta x\right), \text{ with } \beta = \sqrt{2m^*V}/\hbar$$

where x is the barrier width, V is the barrier height and m^* is the effective mass of the hole. Thus, for any given barrier width, a smaller barrier height will result in faster tunneling. It is important to note that the height of the barrier above the initial and final hole states depends on the overall energetics. With this consideration, the difference in the hole tunneling rates to form the exciton versus the XX state can be qualitatively understood in terms of the energetics. The energetic difference arises because of differences in the electron-hole and hole-hole Coulombic interactions.[24] The calculated energetic differences reflect the fact that the electron extends far more into the shell than does the hole. In the cases involving trapped holes, the energetics depend on the location of the trap and calculated values are taken as the average over the ZnSe shell. The following Coulombic energies are calculated for a QD having a core diameter of 2.9 nm and a ZnSe shell thickness of 2.5 nm: electron-electron, $E_{e\text{-}e}$ = 62 meV; electron-hole, $E_{e\text{-}h}$ = -80 meV; hole-hole, $E_{h\text{-}h}$ = 143 meV; electron-trapped hole, $E_{e\text{-}th}$ = -35 meV; hole-trapped hole, $E_{h\text{-}th}$ = 20 meV. The energy difference for hole tunneling to form an exciton is given by;
$\Delta E_X = E_{e\text{-}h} - E_{e\text{-}th}$ = -45 meV. By comparison, the XT to XX energy difference is given by

(Eq 3.17) $\Delta E_{XX} = E_{XX} - E_{XT} = (E_{e\text{-}e} + E_{h\text{-}h} + 4E_{e\text{-}h}) - (E_{e\text{-}e} + E_{h\text{-}th} + 2E_{e\text{-}h} + 2E_{e\text{-}th}) = 33$ meV.

The conclusion that comes from this calculation is that the hole tunneling to convert an XT state to an XX state is about 78 meV less energetically favorable than the simple case of hole tunneling to form the exciton. This is primarily because of the large hole-hole repulsion in the XX state. This difference in energetics has the effect of providing a larger tunneling barrier, *V*, in equation 3.16, for the biexciton case, which slows the XT → XX hole tunneling. While this qualitatively agrees with the experimental result, a more quantitative assessment of XT to XX hole tunneling dynamics would require knowing the distribution of trap energies as well as the trapped hole radial distribution and would therefore be speculative.

3.6 Conclusion

This chapter has shown that the InP/ZnSe QDs have complexities that make significant contributions to their spectroscopic properties that have not been documented in previous QD systems. Indium doped into the shell leads to the formation of transient traps that lead to slow rises and delayed emission in the TRPL. This delayed emission significantly lengthens the radiative lifetime of QDs with large trap contributions. TA experiments were performed to determine that the indium-based traps were transiently trapping holes.

The role of biexcitons in the degradation pathways of these QDs was discussed, and this was shown to be largely attributable to the formation of "hot" electrons and holes. The ratio of "hot" electrons and "hot" holes produced by Auger recombination is described by the Auger branching ratio. Control over this ratio is an important factor in producing biexciton stable InP/ZnSe QDs.

Additionally, the indium-based transient traps were shown to contribute to biexciton kinetics. Biexciton states involving a trapped carrier exhibit significant deviations in behavior from their counterparts without a trapped carrier, and these differences allow for synthetic control over the Auger branching ratio. The presence or absence of these transient traps contribute to all aspects of InP/ZnSe photophysics, allowing for modification of properties such as radiative lifetime, and Auger branching ratio. These two properties are core to high flux and electroluminescent device-based considerations.

3.7 Experimental Methods

Transient absorption spectroscopy measurements were performed using a home-built apparatus previously described.[20] Pulses were produced by a Clark CPA 2001 light source, and detection was with a Princeton Instruments LN_2-cooled CCD and a 0.6 m low dispersion spectrograph. Samples were made with 0.3 μM QDs in degassed, anhydrous

octane in rapidly stirred 1-cm pathlength cuvettes. The transient spectra were obtained following a chopped, 387.5 nm, 1 kHz pulsed excitation.

Time-resolved photoluminescence decays were measured using pulses at 1 MHz from a cavity-dumped, frequency-doubled Coherent 900-F MIRA mode-locked Ti:sapphire laser operating at 415 nm. For measurements of biexciton decay kinetics, pulses were focused through a 10X microscope objective into a 1-cm pathlength cuvette containing 0.3 μM QDs in degassed, anhydrous octane with rapid stirring. Buildup of ions is always a concern in high repetition rate experiments. We find that the PL kinetics were independent of the stirring rate at the highest stir rates, which were maintained throughout the biexciton PL studies. The microscope objective was not used, and the ≈ 3 mm diameter excitation beam was unfocussed for measurements of negative trion kinetics. The luminescence was collected in a back-scatter geometry and imaged through a ¼ m monochromator with a 150 groove/mm grating onto a Micro Photon Devices 50μ PDM single photon avalanche detector (SPAD). The time-correlated single photon-counting decays were accumulated using a Becker-Hickl SPC-130 EMN board. Accurate measurement of the biexciton and negative trion kinetics requires the accurate determination of instrument response function (IRF), which was discussed previously.[11] In the present study, IRF was refined further and taken to be a 42 ps full-width-half-maximum (fwhm) Gaussian and a triexponential tail. Specifically, $IRF(t) = \exp(-t^2/635)$ at $t < 0$ and $IRF(t) = (1 - f)\exp(-t^2/635) + f\,[0.06\exp(-t/3\tau_{exp}) + 0.56\exp(-t/\tau_{exp}) + 0.16\exp(-2.5t/\tau_{exp}) + 0.32\exp(-4.0t/\tau_{exp})]$ at $t > 0$. The parameters are taken to be $f = 0.245$ and $\tau_{exp} = 157$ ps at 625 nm and are $f = 0.280$ and $\tau_{exp} = 145$ ps at 600 nm.

Negatively charged QDs were prepared from photoreduction by lithium triethylborohydride, using a similar procedure to that previously reported.[16,27–29] Briefly, about 10 μL of a 0.1 M lithium triethylborohydride in toluene solution was added to an approximately 3 μM QD solution in a mixed solvent of 0.9 mL toluene and 0.1 mL THF, and the solution was loaded into a sealed cuvette in a glove box. The extent of photoreduction was found to reach its steady state after a few minutes of exposure to room light.

3.8 References

(1) Rodina, A. V.; Efros, A. L. Band-Edge Biexciton in Nanocrystals of Semiconductors with a Degenerate Valence Band. *Phys Rev B Condens Matter Mater Phys* **2010**, *82* (12). https://doi.org/10.1103/PhysRevB.82.125324.

(2) Lange, H.; Kelley, D. F. Spectroscopic Effects of Lattice Strain in InP/ZnSe and InP/ZnS Nanocrystals. *The Journal of Physical Chemistry C* **2020**, *124* (41), 22839–22844. https://doi.org/10.1021/acs.jpcc.0c07145.

(3) Strickler, S. J.; Berg, R. A. Relationship between Absorption Intensity and Fluorescence Lifetime of Molecules. *J Chem Phys* **1962**, *37* (4), 814–822. https://doi.org/10.1063/1.1733166.

(4) Kelley, A. M. *Condensed-Phase Molecular Spectroscopy and Photophysics*; John Wiley & Sons, Inc.: Hoboken, NJ, USA, 2012. https://doi.org/10.1002/9781118493052.

(5) Gong, K.; Martin, J. E.; Shea-Rohwer, L. E.; Lu, P.; Kelley, D. F. Radiative Lifetimes of Zincblende CdSe/CdS Quantum Dots. *The Journal of Physical Chemistry C* **2015**, *119* (4), 2231–2238. https://doi.org/10.1021/jp5118932.

(6) Sercel, P. C.; Efros, A. L. Band-Edge Exciton in CdSe and Other II-VI and III-V Compound Semiconductor Nanocrystals - Revisited. *Nano Letters*. American Chemical Society July 11, 2018, pp 4061–4068. https://doi.org/10.1021/acs.nanolett.8b01980.

(7) Sercel, P. C.; Shabaev, A.; Efros, A. L. Photoluminescence Enhancement through Symmetry Breaking Induced by Defects in Nanocrystals. *Nano Lett* **2017**, *17* (8), 4820–4830. https://doi.org/10.1021/acs.nanolett.7b01662.

(8) Berkinsky, D. B.; Proppe, A. H.; Utzat, H.; Krajewska, C. J.; Sun, W.; Šverko, T.; Yoo, J. J.; Chung, H.; Won, Y.-H.; Kim, T.; Jang, E.; Bawendi, M. G. Narrow Intrinsic Line Widths and Electron–Phonon Coupling of InP Colloidal Quantum Dots. *ACS Nano* **2023**, *17* (4), 3598–3609. https://doi.org/10.1021/acsnano.2c10237.

(9) Kuno, M. *Introductory Nanoscience*; Garland Science, 2011. https://doi.org/10.1201/9780429258442.

(10) Cavanaugh, P.; Sun, H.; Jen-La Plante, I.; Bautista, M. J.; Ippen, C.; Ma, R.; Kelley, A. M.; Kelley, D. F. Radiative Dynamics and Delayed Emission in Pure and Doped InP/ZnSe/ZnS Quantum Dots. *J Chem Phys* **2021**, *155* (24). https://doi.org/10.1063/5.0077327.

(11) Nguyen, A. T.; Jen-La Plante, I.; Ippen, C.; Ma, R.; Kelley, D. F. Extremely Slow Trap-Mediated Hole Relaxation in Room-Temperature InP/ZnSe/ZnS Quantum Dots. *The Journal of Physical Chemistry C* **2021**, *125* (7), 4110–4118. https://doi.org/10.1021/acs.jpcc.0c11317.

(12) Houtepen, A. J.; Hens, Z.; Owen, J. S.; Infante, I. On the Origin of Surface Traps in Colloidal II–VI Semiconductor Nanocrystals. *Chemistry of Materials* **2017**, *29* (2), 752–761. https://doi.org/10.1021/acs.chemmater.6b04648.

(13) Sun, H.; Cavanaugh, P.; Jen-La Plante, I.; Bautista, M. J.; Ma, R.; Kelley, D. F. Reversible Interfacial Charge Transfer and Delayed Emission in InP/ZnSe/ZnS Quantum Dots with Hexadecanethiol. *The Journal of Physical Chemistry C* **2022**, *126* (47), 20065–20073. https://doi.org/10.1021/acs.jpcc.2c06203.

(14) Utterback, J. K.; Cline, R. P.; Shulenberger, K. E.; Eaves, J. D.; Dukovic, G. The Motion of Trapped Holes on Nanocrystal Surfaces. *J Phys Chem Lett* **2020**, *11* (22), 9876–9885. https://doi.org/10.1021/acs.jpclett.0c02618.

(15) Sun, H.; Cavanaugh, P.; Jen-La Plante, I.; Bautista, M. J.; Ma, R.; Kelley, D. F. Reversible Interfacial Charge Transfer and Delayed Emission in InP/ZnSe/ZnS Quantum Dots with Hexadecanethiol. *The Journal of Physical Chemistry C* **2022**, *126* (47), 20065–20073. https://doi.org/10.1021/acs.jpcc.2c06203.

(16) Hou, X.; Kang, J.; Qin, H.; Chen, X.; Ma, J.; Zhou, J.; Chen, L.; Wang, L.; Wang, L.-W.; Peng, X. Engineering Auger Recombination in Colloidal Quantum Dots via Dielectric Screening. *Nat Commun* **2019**, *10* (1), 1750. https://doi.org/10.1038/s41467-019-09737-2.

(17) Efros, A. L.; Rosen, M.; Kuno, M.; Nirmal, M.; Norris, D. J.; Bawendi, M. *Band-Edge Exciton in Quantum Dots of Semiconductors with a Degenerate Valence Band: Dark and Bright Exciton States*; 1996.

(18) Ashokan, A.; Mulvaney, P. Spectroelectrochemistry of Colloidal CdSe Quantum Dots. *Chemistry of Materials* **2021**, *33* (4), 1353–1362. https://doi.org/10.1021/acs.chemmater.0c04416.

(19) Wu, K.; Lim, J.; Klimov, V. I. Superposition Principle in Auger Recombination of Charged and Neutral Multicarrier States in Semiconductor Quantum Dots. *ACS Nano* **2017**, *11* (8), 8437–8447. https://doi.org/10.1021/acsnano.7b04079.

(20) Morgan, D. P.; Kelley, D. F. What Does the Transient Absorption Spectrum of CdSe Quantum Dots Measure? *The Journal of Physical Chemistry C* **2020**, *124* (15), 8448–8455. https://doi.org/10.1021/acs.jpcc.0c02566.

(21) Klimov, V. I. Optical Nonlinearities and Ultrafast Carrier Dynamics in Semiconductor Nanocrystals. *J Phys Chem B* **2000**, *104* (26), 6112–6123. https://doi.org/10.1021/jp9944132.

(22) Won, Y.-H.; Cho, O.; Kim, T.; Chung, D.-Y.; Kim, T.; Chung, H.; Jang, H.; Lee, J.; Kim, D.; Jang, E. Highly Efficient and Stable InP/ZnSe/ZnS Quantum Dot Light-Emitting Diodes. *Nature* **2019**, *575* (7784), 634–638. https://doi.org/10.1038/s41586-019-1771-5.

(23) Klimov, V. I. Spectral and Dynamical Properties of Multiexcitons in Semiconductor Nanocrystals. *Annu Rev Phys Chem* **2007**, *58* (1), 635–673. https://doi.org/10.1146/annurev.physchem.58.032806.104537.

(24) Sun, H.; Cavanaugh, P.; Jen-La Plante, I.; Ippen, C.; Bautista, M.; Ma, R.; Kelley, D. F. Biexciton and Trion Dynamics in InP/ZnSe/ZnS Quantum Dots. *J Chem Phys* **2022**, *156* (5), 054703. https://doi.org/10.1063/5.0082223.

(25) Shabaev, A.; Rodina, A. V.; Efros, Al. L. Fine Structure of the Band-Edge Excitons and Trions in CdSe/CdS Core/Shell Nanocrystals. *Phys Rev B* **2012**, *86* (20), 205311. https://doi.org/10.1103/PhysRevB.86.205311.

(26) Vaxenburg, R.; Rodina, A.; Lifshitz, E.; Efros, A. L. Biexciton Auger Recombination in CdSe/CdS Core/Shell Semiconductor Nanocrystals. *Nano Lett* **2016**, *16* (4), 2503–2511. https://doi.org/10.1021/acs.nanolett.6b00066.

(27) Rinehart, J. D.; Schimpf, A. M.; Weaver, A. L.; Cohn, A. W.; Gamelin, D. R. Photochemical Electronic Doping of Colloidal CdSe Nanocrystals. *J Am Chem Soc* **2013**, *135* (50), 18782–18785. https://doi.org/10.1021/ja410825c.

(28) Tsui, E. Y.; Carroll, G. M.; Miller, B.; Marchioro, A.; Gamelin, D. R. Extremely Slow Spontaneous Electron Trapping in Photodoped *n* -Type CdSe Nanocrystals. *Chemistry of Materials* **2017**, *29* (8), 3754–3762. https://doi.org/10.1021/acs.chemmater.7b00839.

(29) Cohn, A. W.; Rinehart, J. D.; Schimpf, A. M.; Weaver, A. L.; Gamelin, D. R. Size Dependence of Negative Trion Auger Recombination in Photodoped CdSe Nanocrystals. *Nano Lett* **2014**, *14* (1), 353–358. https://doi.org/10.1021/nl4041675.

Chapter 4. Role of Zinc Vacancies as Transient Traps in Indium Phosphide Quantum Dots

4.1 Introduction

The present chapter considers several possibilities for the transient traps discussed in the previous chapter and will identify the traps as zinc vacancies in the ZnSe shell lattice being charge compensated by an In^{3+}. This assignment will be done through a combination of experiment and calculation. Density functional theory calculations on small ZnSe clusters containing different indium-associated impurities were used to characterize several possible trapping species. The assignment to the In^{3+}/V_{Zn}^{2-} species is supported by literature precedents and by both experiment and calculation. In addition, this chapter makes and then tests the prediction that it should be possible to increase the trap density by reaction with oleic acid and decrease the trap density by the reaction with zinc oleate or zinc acetate. Raman spectroscopy will be used to characterize the radial distribution of the indium in the shell as a proxy for the location of the In^{3+}/V_{Zn}^{2-} traps in the shell.

This chapter will demonstrate the extent of coupling between the In^{3+}/V_{Zn}^{2-} and the surrounding matrix by use of hexadecanethiol (HDT). HDT is a hole acceptor and will be shown to be able to accept holes from the In^{3+}/V_{Zn}^{2-} traps near the QD surface. It was already shown in the previous chapter that there is an equilibrium formed between traps in the shell and the valence band. This demonstration of traps coupling to the system outside the QD has large implications for electroluminescence devices (ELD). In these devices QDs are not excited by photons, instead an electron is directly injected into the conduction band, and holes are injected into the valence band electrochemically.

4.2 Identity of Indium Based Traps

The dynamics reported in the previous chapter require that the trap species has a lowest energy level close to that of the quantum confined hole, and consideration of these energetics is crucial to assigning the trapping species. Estimates of the InP-ZnSe valence band offset vary over a significant range, from about 0.5 to 1.0 eV. Perhaps the most reliable estimate is from photoemission data, which puts the valence band offset at 0.97 eV.[1] In the case of red-emitting QDs the hole quantum confinement energy is calculated to be 0.22 eV, putting the quantum confined hole energy 0.75 eV above (closer to the vacuum level) the ZnSe valence band edge. If the trap is in thermal equilibrium with the valence band, then the trap energy must be within the Boltzmann distribution at room temperature (26 meV) of this value. The uncertainty of this value is partially determined by the uncertainty of the InP-ZnSe valence band offset. Furthermore, this trap depth is necessarily approximate because the presence of interfacial dipoles which as discussed in chapter 2 shifts the valence band versus trapped hole energies by several tens of milli-electron volts. Apart from its energy, the other characteristic of the hole trap is that radiative recombination with the conduction band electron is nearly or completely forbidden.

In order to determine the chemical species responsible for this trapping behavior density functional theory calculations were conducted by collaborators.[2] These calculations were used to rule out some candidates and provided other candidate species that could be ruled out experimentally. In the core of the QDs, indium exists primarily in

the In^{3+} oxidation state. While In^{3+} could theoretically be considered as a trapping species, it is unlikely to be oxidized further to create reversible traps. The energy levels associated with In^{3+} oxidation would be too high to facilitate reversible hole trapping. One possibility considered was the reduction of indium ions to In^{2+} before their incorporation into the ZnSe shell. In^{2+} ions can act as hole traps in some materials. However, DFT calculations suggested that In^{2+} would be a deep trap, not suitable for reversible hole trapping. The formation of indium dimers in the shell was also considered. However, DFT calculations showed that these dimers would also result in deep trapping levels, making them unsuitable for reversible hole trapping.[2]

Alternatively, the trap might be localized on another species whose presence is enabled by incorporation of indium into the shell. Since many InP/ZnSe syntheses involve the use of $ZnCl^2$, the presence of chloride ions was considered. It was hypothesized that chloride ions might be incorporated into the ZnSe lattice as dopants, possibly in combination with In^{3+}. However, experiments involving rigorously chloride-free QDs demonstrated that the reversible hole traps were not associated with chloride ions. Initially, zinc vacancies (V_{Zn}^{2-}) were considered as potential traps. While DFT calculations shown in figure 4.1 suggest that these vacancies occur at close to the correct energy level, the experimental dependance on indium concentration suggested that the zinc vacancies alone do not act as hole traps. It is only when these vacancies were partially charge-compensated by the presence of an adjacent substitutional In^{3+} that they exhibited trapping behavior. The proposed In^{3+}/V_{Zn}^{2-} species was found to be the most likely candidate for the reversible hole traps in the InP/ZnSe/ZnS QDs due to its energetics, which closely matched the experimentally observed trap energies.

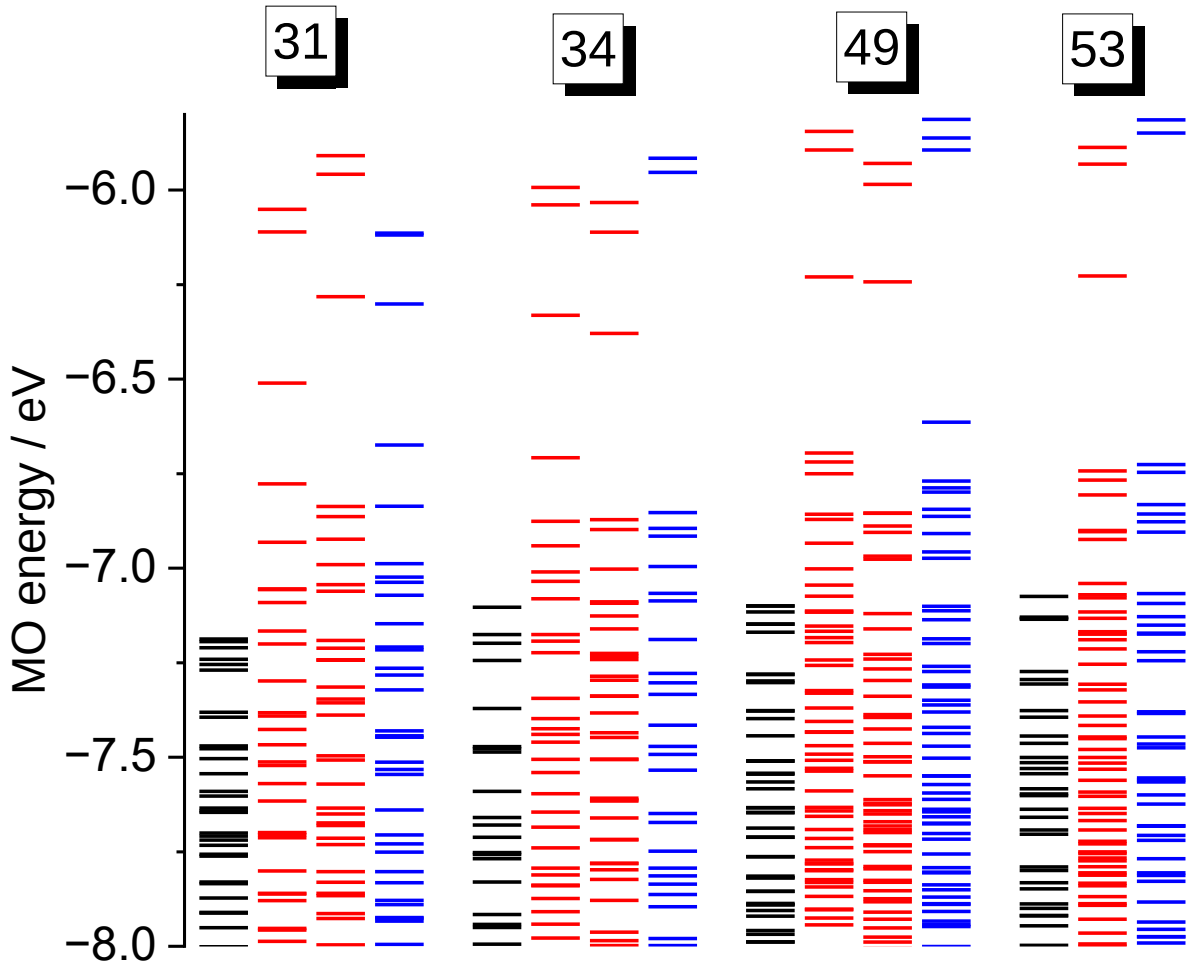

Figure 4.1: Calculated molecular orbital energies for ZnSe clusters of the indicated number of ZnSe subunits with no substitution (black), In^{3+} substitution plus zinc vacancy (red, two different positions for each of the three smallest clusters), and uncompensated zinc vacancy (blue). All calculated orbitals with energies between -8.0 and -2.5 eV are shown, and all of these are doubly occupied. [2]

In bulk ZnSe, optically detected magnetic resonance (ODMR) results show that zinc vacancies with a -2 charge (V_{Zn}^{2-}) give rise to an energy level 0.66 eV above the top of the ZnSe valence band.[3,4] This measured energy is consistent with values recently obtained from DFT calculations, supporting the assignment.[14] Zinc vacancies in bulk ZnSe that are charge compensated by an adjacent (substitutional) In^{3+} ion have also been studied and their energetics determined by transient photocurrent measurements.[5] These measurements put the acceptor energy of the singly charged vacancy adjacent to the In^{3+} (the In^{3+}/V_{Zn}^{-} electron acceptor or In^{3+}/V_{Zn}^{2-} hole acceptor complex) close to that of the zinc vacancy, 0.59 eV above the ZnSe valence band. Localization of the trapped hole results in a strong local electric field which distorts the surrounding lattice. Thus, the trapping energy includes a significant contribution from electron-phonon coupling, as found for surface traps in CdSe and CdS.[6–8] This energy is 0.16 eV lower than that

inferred above for the valence band hole, which is well within the uncertainty of the reported band offsets. It follows from the energetics that the presence of the adjacent In^{3+} stabilizes the doubly negatively charged zinc vacancy and makes it about 70 meV harder to oxidize.

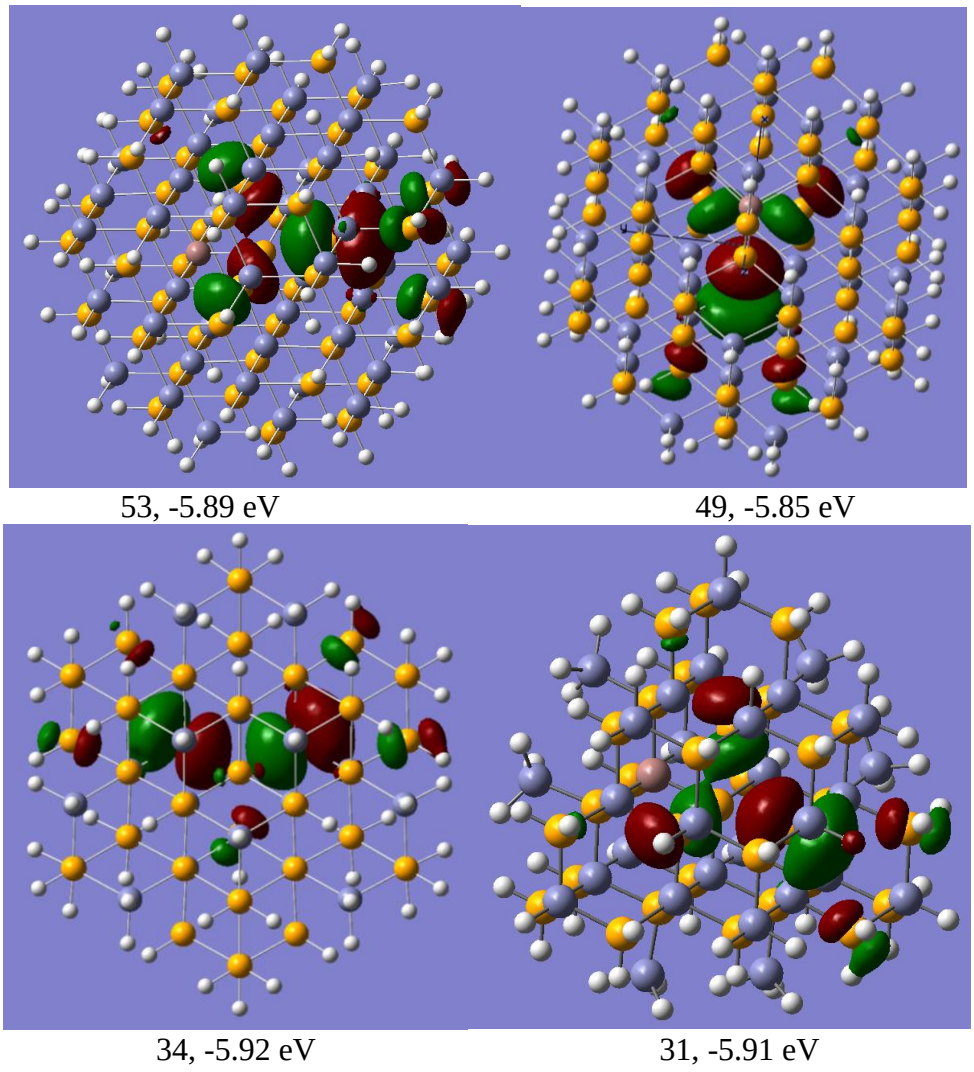

Figure 4.2: The highest energy occupied orbital of the four ZnSe structures having a zinc vacancy and a substitutional indium (atom in brown).[2]

The calculated highest occupied molecular orbital (HOMO) for the compensated vacancies shown in figure 4.2 is composed mainly of p orbitals on the four Se atoms surrounding the vacancy, with only slight participation from other atoms. This hole orbital should have a negligible overlap integral with the electron in the lowest conduction band orbital, which is delocalized over both the InP core and the full ZnSe shell, leading to a negligible rate of radiative recombination. Figure 4.2 also shows that

the HOMO level of the transient trap state occupies only a few unit cells in volume and is in strong agreement with the predicted negligible overlap.

Assignment to an In^{3+}/V_{Zn}^{2-} species is also consistent with several other experimental results. Significant trapping requires the presence of at least a small indium excess.[9] Furthermore, in QDs having an overall indium concentration that exceeds a small excess, the extent of trapping is indium concentration independent. This implies that not all indium dopants are associated with traps and that zinc vacancies, by themselves, either do not occur at significant concentrations or are not hole traps. Two types of experimental results indicate that while in a specific QD ensemble the indium concentration is constant, the vacancy concentration can be varied. These results involve measuring the PL risetime kinetics of the CD-2.72 QDs following reaction with excess zinc carboxylate or excess carboxylic acid. The CD-2.72 QDs are chosen for these studies because prior to any treatment, they exhibit a large, slow risetime component in the PL kinetics that can be easily and accurately measured.[5]

(Eq 4.1) $$2RCOO^- + QD(V_{Zn}^{2-})_n \rightleftharpoons Zn(RCOO)_2 + QD(V_{Zn}^{2-})_{n+1}$$

Addition of alkyl carboxylic acids or zinc carboxylates shifts the reaction equilibrium toward products or reactants, respectively, as one would expect from Le Chatelier's principle. We have performed this reaction with zinc acetate at room temperature and zinc oleate at room temperature and 100 °C. We note that the corresponding reaction with zinc acetate cannot be run at 100 °C; the surface ligands become labile at elevated temperatures and the oleate ligands can be replaced by acetate, resulting in the loss of colloidal stability. Figure 4.3 shows that following treatment at room temperature, the risetimes with zinc oleate and acetate are essentially identical. Figure 4.3 also shows that the reaction with zinc oleate at 100 °C results in a decrease in the risetime that is larger than that obtained at room temperature. This is especially true for the slowest risetime component. Diffusion of the zinc ions through the ZnSe lattice is expected to be faster at elevated temperatures. The temperature dependence of the fraction of vacancies that are filled suggests ion diffusion through the lattice, rather than solution diffusion of the zinc precursor species, is the rate limiting step in this reaction. However, the observed temperature dependence may also reflect a temperature dependence of the equilibrium constant, with incomplete relaxation of the higher temperature equilibrium upon cooling.

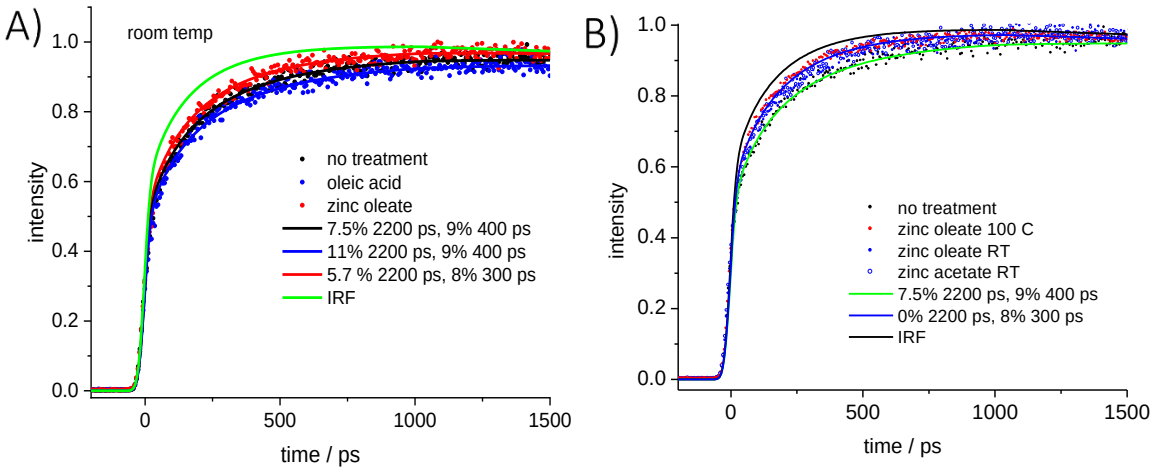

Figure 4.3: Normalized PL kinetics and fits for QDs following A) no treatment, room temperature exposure to excess zinc oleate, and room temperature exposure to excess oleic acid. Also shown is a calculated curve corresponding to an instantaneous risetime (IRF limited) B) Exposure to excess zinc oleate and zinc acetate at room temperature, zinc oleate at 100 ºC, and the PL kinetics before treatment. Also shown is a calculated curve corresponding to an instantaneous risetime (IRF limited).

We note again that much larger slow risetime components are observed in the core-derivatized QDs compared to nonstoichiometric QDs, indicating that the core-derivatized QDs have much higher trap densities.[10] This observation is also consistent with the assignment of the traps to In^{3+}/V_{Zn}^{2-} impurities. The essential difference between these types of QDs is the nature of the core-shell interface. The core-derivatized QDs have had the cores treated with an excess of zinc carboxylate, added to the reaction mixture immediately following core growth. This results in zinc ion adsorption and/or indium-to-zinc ion exchange on the core surface. Thus, we conclude that in the core-derivatized QDs, the core-shell interface has a larger contribution of P-Zn bonding, rather than In-Se bonding. From the model in figure 2.4 it follows that trap to valence band tunneling should be more energetically favorable when the interfaces have more Zn/P character, that is, when PL detection is on the red edge of the PL band. In addition, the P-Zn bonding partially mitigates the lattice strain associated with the mismatch of InP and ZnSe lattice constants. The lattice mismatch expands the ZnSe lattice, and this effect is minimized in the case of the core-derivatized QDs. The DFT calculations show that the presence of a zinc vacancy locally contracts the lattice[2]. Lattice contraction is energetically less favorable when the lattice has been expanded by the presence of the interface with InP. Thus, we suggest that vacancy formation is more energetically favorable near a P-Zn rich interface, and this results in the core-derivatized QDs having greater trap densities than their nonstoichiometric counterparts.

4.3 Raman Spectroscopy for Characterizing Spatial Distribution of In^{3+}/V_{Zn}^{2-}

Probing the location of defects in quantum dots is one of the most challenging aspects of QD spectroscopy. Raman experiments provide valuable insights into the vibrational modes associated with the electronic states of quantum dots and allow for the investigation of the core-shell interface, which is crucial for understanding and tailoring the interfacial properties of these QDs as discussed in prior sections. In a Raman experiment, the incident light is tuned to match the energy of an electronic transition in the sample of interest. By doing so, the Raman scattering efficiency is greatly enhanced for certain vibrational modes that are associated with the resonantly excited electronic states. The optical phonons of bulk InP and bulk ZnSe span the regions 300−350 and 200−260 cm^{-1}, respectively[11,12]. The Raman spectra of pure InP nanocrystals are dominated by the longitudinal optical (LO) phonon at 349 cm^{-1} and what is generally assigned as the transverse optical (TO) phonon at 306 cm^{-1}.[13] Resonance Raman spectra of InP nanocrystals of widely varying sizes and qualities show peaks fairly close to these bulk frequencies plus the overtones of these modes.

Excitation into the lowest energy transition of the QD produces an electron-hole pair that is primarily localized in the InP core and therefore gives the largest resonance enhancement to the InP phonon modes. However, at wavelengths near the first transition, the Raman spectrum is dominated by fluorescence, which is many orders of magnitude more intense than the Raman scattering. To overcome this challenge in most QD systems, quenching with thiols or amines is performed to minimize this fluorescence. However, in the case of InP/ZnSe QDs, the ZnSe shell provides strong confinement to the hole and prevents fast quenching. As a result, Raman studies of InP/ZnSe are limited to transitions far enough above the band edge where fluorescence is minimal, allowing for better examination of the phonon modes. Excitation at 501.7 nm is slightly above the fluorescent region and produces excitons that are mostly core localized, but significantly spill out into the first few monolayers of shell. At this wavelength, the ZnSe and InP phonons have comparable intensities. The result is that excitation in this region is diagnostic of the core-shell interfacial phonon modes. As the excitation energy is tuned further blue to 457 nm and then to the 400 nm region it becomes resonant with transitions increasingly delocalized into the ZnSe shell and leads to resonance enhancement of primarily ZnSe phonon modes. The difference in phonon intensities and line-shape as the excitation wavelength is varied are apparent in figure 4.4.

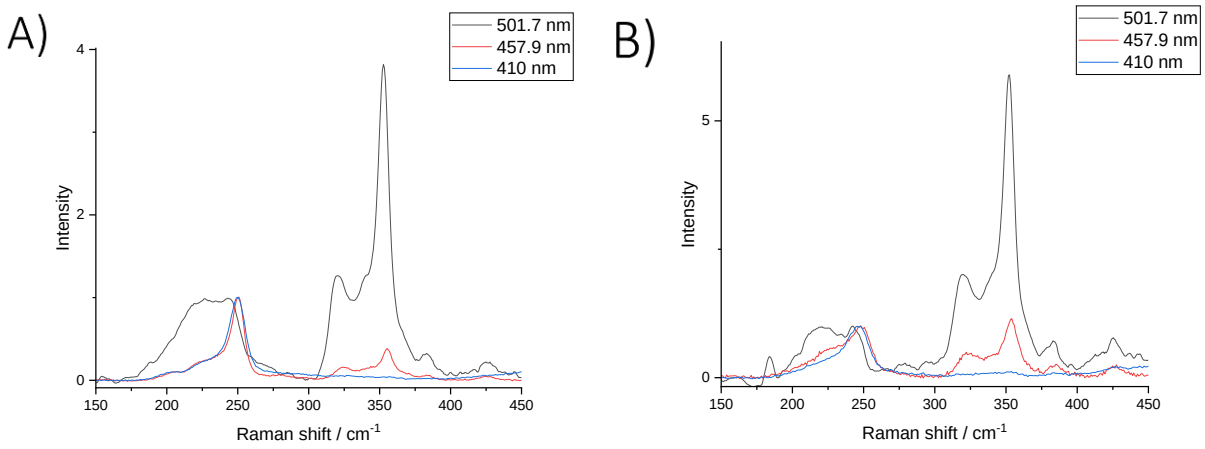

Figure 4.4: A) S-2.51 and B) NS-1.68 at 3 wavelengths (501.7, 457.9, and 410 nm) with the intensity normalized at the ZnSe LO phonon peak at ~257 cm^{-1}. These show the effect of varying the excitation wavelength on the Raman spectrum.

Comparing the spectra of any given structure at 410, 457.9, and 501.7 nm, there are two obvious trends. First, the intensities of the ZnSe modes increase relative to those of the InP modes as the excitation is tuned to shorter wavelengths. This is a straightforward consequence of the considerations that were just discussed. Second, the lower-frequency component of the ZnSe feature becomes relatively weaker as the excitation is tuned from 501.7 to 410 nm. This strongly suggests that the lower-frequency component of the ZnSe phonon modes is dominated by motions of ZnSe groups at or very near the interface with the InP core, as the lowest-energy excitons extend only slightly into the shell.

The shift to higher wavenumbers of the higher frequency ZnSe component by 2−6 cm^{-1} at bluer excitation wavelengths also supports this observation. A similar phenomenon was observed in previously studied CdSe/CdS core/shell quantum dots.[14] In that case, the frequency of the CdS LO phonon peak decreased from 301 cm^{-1} to 285−290 cm^{-1} as the excitation wavelength was tuned from 5000 cm^{-1} above the lowest, core-localized excitonic transition to resonance with that lowest exciton. This shift indicated that the CdS modes at the interface with the CdSe core were of lower frequency than the CdS modes in the bulk shell. This behavior can be explained as the result of elastic expansion of the shell due to the larger lattice constant of the core along with a contribution from the mixing of lower-frequency CdSe phonon modes with the CdS modes near the interface. This interpretation gains further support from the spectra of InP/ZnSe core/shell quantum dots with varying shell thicknesses.

As mentioned in chapter 1, the synthesis of core-derivatized QDs includes treating the InP cores with $Zn(OA)_2$ prior to purification and shell growth. This results in the core surface being preferentially Zn-terminated and/or having a very thin zinc phosphide surface layer, which is less prevalent in the case of the stoichiometric and nonstoichiometric QDs. As a result of the change in interfacial bonding, the spectrum obtained for the CD-2.55 QDs shown in figure 4.5 has similarities and differences when

compared to the S-2.51 and NS-2.25 spectra. The CD-2.55 spectrum shows the same reduced intensity in the 210-235 cm^{-1} region as does the S-2.51, indicating the lack of indium at the core-shell interface. Instead, it is likely that the core-shell interface has zinc-phosphorous bonding formed by ion exchange upon core derivatization. The core-derivatized spectrum shows additional intensity at approximately 252 cm^{-1}, causing the peak maximum to shift from 247.8 to 249.5 cm^{-1} and broaden from 12.0-14.5 cm^{-1} FWHM. We tentatively assign this high frequency feature to interfacial modes associated with interfacial zinc-phosphorous bonding.

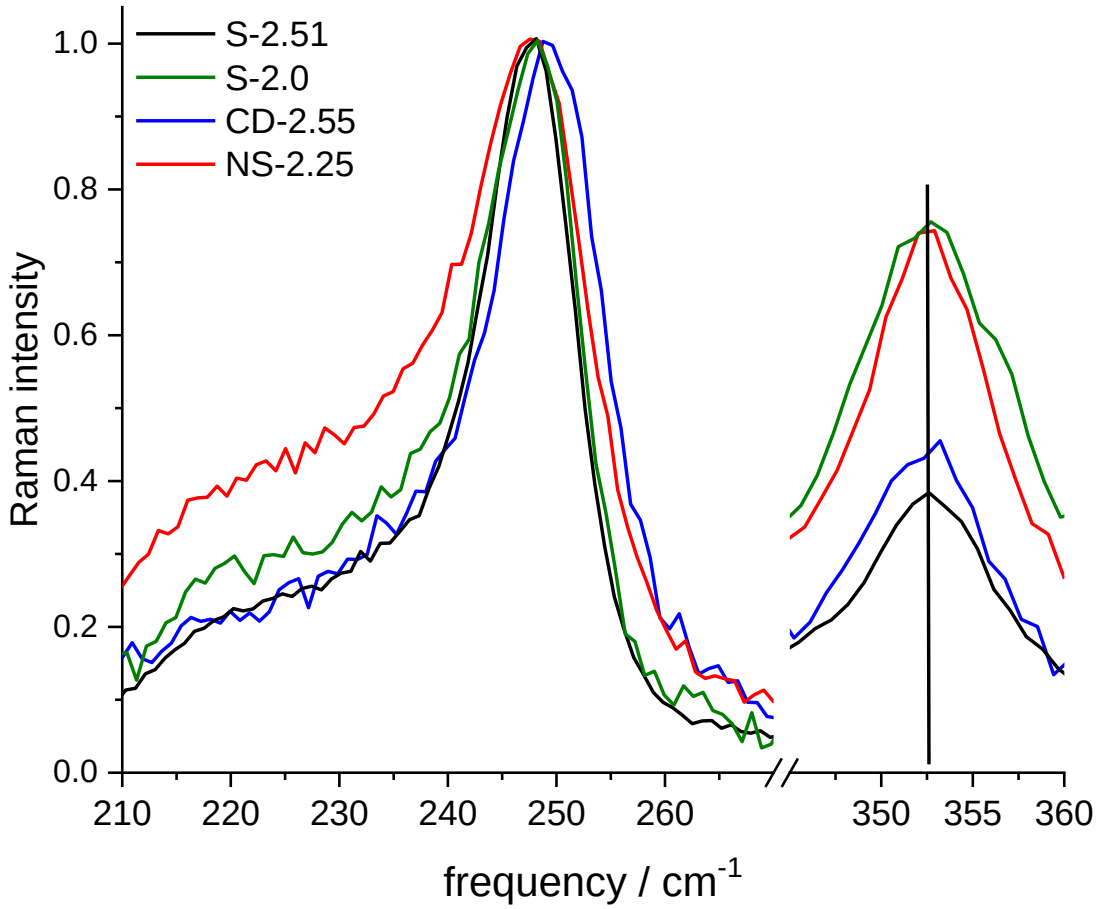

Figure 4.5: Raman spectra of the ZnSe and InP phonon regions excited at 457.9 nm of S-2.51, CD-2.55 and NS-2.25 QDs. Also shown is the spectrum for the S-2.51 QDs following correction for the compression caused by the presence of the thicker ZnS. This correction shifts the spectrum 2.7 cm^{-1} to lower frequencies. See experimental methods for the correction method.

The difference in interfacial bonding affects the lattice strain in the shell. The presence of comparatively long In-Se bonds increases the strain on the proximal ZnSe lattice. Conversely an intermediate layer having P-Zn bonds can result in relatively close packed zinc ions partially mitigating the lattice strain on the ZnSe side of the InP-ZnSe interface. The expansion of the ZnSe lattice due to In-Se interfacial bonding leads to a more favorable environment near the core/shell interface for doping the relatively large indium ions. This results in an increased indium concentration near the core-shell interface. Conversely, we predict the opposite behavior at P-Zn rich interfaces. Closely packed zinc ions counteract the tendency for excess indium atoms to accumulate at the core-shell interface. Consequently, in QDs with core-derivatized structures, the distribution of indium dopants is observed further out in the ZnSe shell.

This is supported by the risetimes observed in core-derivatized and nonstoichiometric QDs as seen in chapter 3. Nonstoichiometric QDs showed significantly faster rise times at similar shell volumes. This suggests that the indium-based traps are nearer to the core than in their core-derivatized counterparts. Taken together these two datapoints suggest that the solubility of these traps in the ZnSe shell is largely governed by strain forces. This also shows that interfacial bonding has a significant impact on the extent of trapping.

4.4 Coupling of In^{3+}/V_{Zn}^{2-} to the Environment

This section analyzes the PL risetime and the subsequent decay kinetics of QDs with and without an adsorbed hole acceptor, HDT. HDT is used in this study because its hole acceptor energetics are such that holes can form an equilibrium between being on the HDT, in hole traps, or in the core-localized valence band. Other hole acceptors were considered, but were either unreactive, or like methylbenzene thiol (MBT) were too good of a hole acceptor leading to irreversible hole transfer. These kinetics are strongly dependent on the nature of the core–shell interface and the thickness of the ZnSe shell. As discussed in the previous chapter long risetimes and delayed emission are most significant in core-derivatized QDs and are not seen in stoichiometric and to a much lesser extent in nonstoichiometric QDs. Similarly, we find that treatment with HDT results in much smaller effects on the PL kinetics when applied to nonstoichiometric and no effect when applied to stoichiometric particles. Because of these considerations, the present study focuses on core-derivatized QDs.

The addition of HDT results in small changes in the overall PL quantum yield. The CD-2.72 QDs shown in figure 4.6 exhibit a 10–20% decrease in quantum yield that is fully reversible upon ligand exchange with zinc oleate. This drop in PL QY is probably due to the formation of surface carrier traps upon ligand exchange with HDT. However, the possibility of some fraction of the HDT ligands acting as irreversible hole acceptors cannot be excluded.

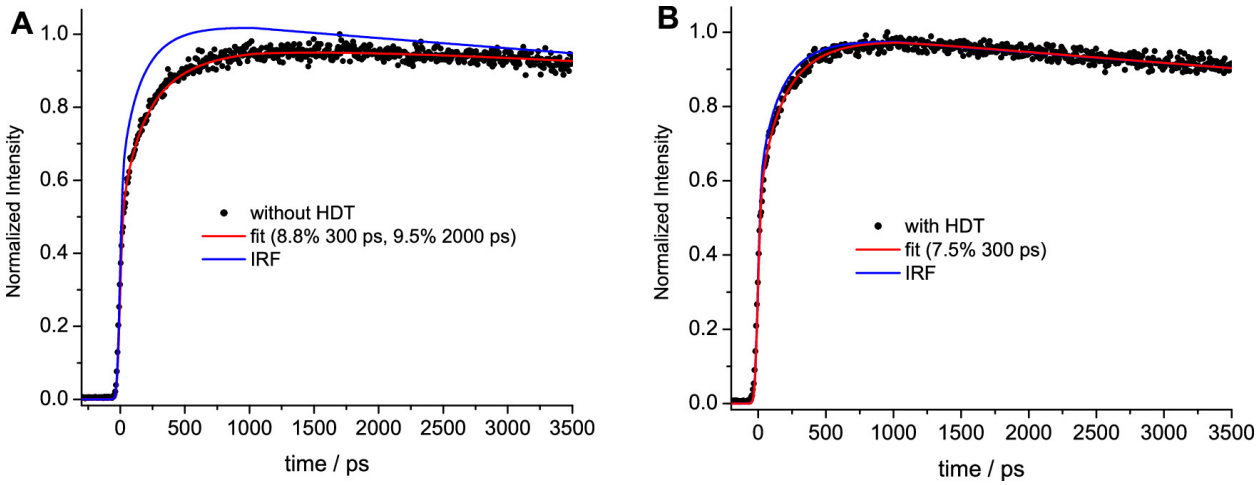

Figure 4.6: PL risetime kinetics for CD-2.72 A) without and B) with HDT. Also shown are fit curves (red) and curves corresponding to the instrument response function convolved with a fast rise and 32 ns decay (blue).

Finite PL risetimes are assigned to holes being transiently localized in shell traps before relaxing to the valence band. As shown in figure 4.6 prior to the addition of HDT, the CD-2.72 QDs exhibit an obvious slow PL risetime that can be fit to a biexponential. This biexponential has approximately 300 ps and 2.0 ns components having roughly comparable amplitudes, each making up ~9% of the total PL intensity. The addition of HDT dramatically reduces the amplitude and timescale of the risetime. The magnitude of the short component is slightly reduced (from 8.8 to 7.5%), and the long-risetime component is essentially eliminated. This is because a sufficiently rapid interfacial charge transfer equilibrium is established such that hole transfer from the outermost shell-localized traps efficiently competes with tunneling to the QD core, resulting in a loss of much of the slow PL risetime.

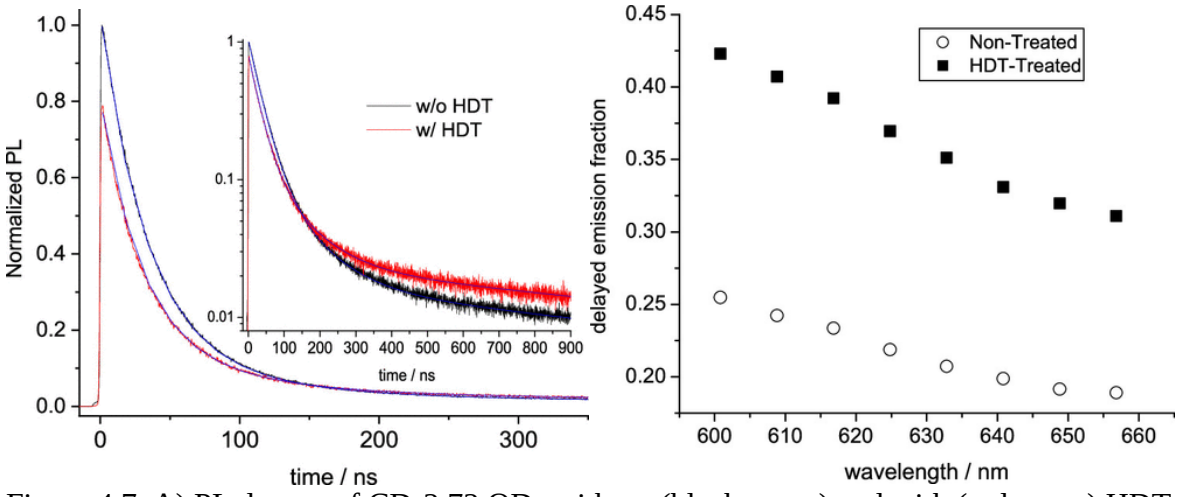

Figure 4.7: A) PL decays of CD-2.72 QDs without (black curve) and with (red curve) HDT. The inset shows the same data and fits, extended to longer times, on a log scale. The decays are normalized such that the areas under the decays are proportional to the intensity in the static PL spectrum. Also shown are fit (blue) curves corresponding to 33.2 ns (87.3%), 97 ns (11.4%), and 800 ns (1.33%) for the QDs without HDT and 27.5 ns (73.3%), 75 ns (24%), and 800 ns (2.7%) for the QDs with HDT. B) Fraction of the total PL that occurs as delayed emission as a function of detection wavelength for the CD-2.72 QDs.

Delayed emission also involves the same traps, specifically thermal population of the traps diminishes the hole population in the valence band, thereby slowing the rate of band edge luminescence. As mentioned previously, these traps do not act as recombination centers, and although their presence alters the PL kinetics, they do not affect the overall quantum yield. This produces an equilibrium between the thiols and the valence band. The population of the shell-localized traps corresponds to a reservoir of hole states that eventually tunnel to the core-localized valence band, resulting in delayed emission. The amount of delayed emission is increased by the additional reservoir which is created by the presence of HDT ligands.

The PL decays shown in figure 4.7A obtained with and without HDT show a large amplitude, relatively short decay followed by smaller amplitude, and much longer decay components. The radiative lifetime for InP/ZnSe/ZnS QDs having these dimensions and no In^{3+}/V_{Zn}^{2-} transient traps is about 30 ns, and these decay curves show minor differences in the shorter-lived (~30 ns) component. This larger amplitude short decay represents prompt band edge emission without the formation of an equilibrium. The small amplitude longer decay has components on the order of hundreds of nanoseconds and represents the contribution of HDT to the trap equilibrium.

Figure 4.7B also shows that the delayed emission is an increasing fraction of the total PL decay as the observation wavelength is moved from the red to the blue edge of the PL spectrum. This can be understood in terms of the model discussed in chapter 2 and diagramed in figure 2.4 in which position of the valence band is controlled by core–shell interfacial dipoles. This model predicts that the bluer QDs with more In/Se rich interfaces would have a valence band at higher energy than the P/Zn rich interfaces. This would

shift the equilibrium towards the HDT ligands in the first case, and away in the latter case as is seen in figure 4.7.

This delayed emission is not observed in stoichiometric QDs. This is because without In^{3+}/V_{Zn}^{2-} transient traps the ZnSe shell provides too great of a potential barrier to allow for the hole to transfer. This in turn suggests that the presence of these traps can allow for holes to be electrochemically injected into the valence band through equilibrium dynamics at much lower potentials than would be required to deposit them through the ZnSe shell. This decrease in required overpotential is a twofold benefit for ELD applications, increasing energy efficiency and lowering the voltage requirements of the surrounding matrix.

4.5 Conclusions

Numerous possibilities regarding the chemical/structural identity of the reversible traps observed in the PL dynamics of InP/ZnSe/ZnS QDs have been considered. Through a combined approach involving experimental data and calculations, it has been shown that these traps are associated with zinc vacancies (V_{Zn}^{2-}) that are partially charge-compensated by substitutional In^{3+} ions. Density functional theory (DFT) calculations have indicated that zinc vacancies can produce states with energies and orbital characteristics suitable to serve as traps. This assignment is supported by the proximity of the experimentally inferred trap energies to the energy level of the defect assigned to a zinc vacancy/substitutional indium complex in indium-doped bulk ZnSe. Additionally, it was demonstrated that traps can be added or removed by exposing the QDs to excess zinc carboxylate or carboxylic acid, further reinforcing the proposed identification.

Raman spectroscopy was used to probe the structural characteristics of the QD and to elucidate the position of excess indium in the QD. In a nonstoichiometric synthesis, where interfacial chemistry is not well controlled, indium was found to accumulate near the core shell-interface. Changes in the core-shell interface, such as treatment with zinc oleate before shelling, were shown to modulate the position of the traps in the shell, which in turn affects the time it takes for a hole to tunnel back into the core.

Additionally, it was shown that the In^{3+}/V_{Zn}^{2-} transient traps allow for the formation of an equilibrium with hole acceptors near the surface leading to delayed emission. This delayed emission is not observed in stoichiometric QDs. Without the presence of In^{3+}/V_{Zn}^{2-} transient traps the ZnSe shell provides too great of a potential barrier to allow for the hole to efficiently transfer. This in turn suggests that the presence of these traps can allow for holes to be electrochemically inserted into the valence band through equilibrium dynamics at much lower potentials than would be required to deposit them through the ZnSe shell.

4.6 Experimental Methods

TRPL methods in this chapter are the same as those discussed in the previous chapter. For information on how DFT calculations were performed see Reference 2.

Raman experiments were performed with samples contained in 1 mm fused silica cuvettes, and the Raman scattering was collected in a backscattering geometry Excitation at 501.7 and 457.9 nm was obtained from an argon-ion laser. Excitation at 410 nm was obtained from a frequency-doubled Ti:sapphire laser producing 1−2 ps pulses at 82 MHz. The wavenumber axes were calibrated by using the 801 cm^{-1} cyclohexane line. The excitation beam was focused onto the sample by using a 10× microscope objective at an average power of about 0.75 mW, and typically a signal was accumulated for 60 min on each sample.

The Raman spectra of the stoichiometric S-2.51 QDs provide a good comparison to both the core-derivatized and nonstoichiometric particles. However, the S-2.51 particles have a relatively thick ZnS outer shell that is lacking in the core-derivatized and nonstoichiometric particles. This causes compression of both the InP core and the ZnSe inner shell, shifting both types of peaks in the Raman spectra to higher frequencies[15]. The magnitude of ZnSe phonon shift can be accurately calculated and this correction can be applied to the spectra. This calculation uses the shift of the InP LO phonon peak as a calibration of the internal pressure to calculate the shift of the ZnSe phonon peak. In determining the internal pressure and applying this correction, the calculation uses the respective Grüneisen parameters (γ = 1.24 InP, 1.55 ZnSe), bulk moduli (K = 71 GPa for InP and 62.4 GPa for ZnSe) and LO phonon frequencies of InP and ZnSe (352 cm^{-1}, 248 cm^{-1}).

$$\text{Eq 4.2} \quad \gamma = \frac{\Delta\omega}{\omega}\frac{V}{\Delta V} = \frac{\Delta\omega}{\omega}\frac{P}{K}$$

P is the pressure due to the ZnS shell. Combining this expression for the InP core and the ZnSe shell and taking the pressure on both to be the same we get:

$$\text{Eq 4.3} \quad \frac{\Delta\omega_{ZnSe}}{\Delta\omega_{InP}} = \frac{\gamma_{ZnSe}K_{InP}\omega_{ZnSe}}{\gamma_{InP}K_{ZnSe}\omega_{InP}}$$

This ratio is 1.002, which means that to within a few hundredths of a wavenumber, simply shifting the entire spectra by the amount required to align the InP LO phonon peaks will also correct for any ZnS compression effects in the ZnSe peaks. We note that this is not true of most materials and is purely coincidental in the InP/ZnSe system. The corrected spectrum of the S-2.51 QDs is shown in figure 4.5.

4.8 References

(1) Stevanović, V.; Lany, S.; Ginley, D. S.; Tumas, W.; Zunger, A. Assessing Capability of Semiconductors to Split Water Using Ionization Potentials and Electron Affinities Only. *Physical Chemistry Chemical Physics* **2014**, *16* (8), 3706. https://doi.org/10.1039/c3cp54589j.

(2) Kelley, A. M.; Cavanaugh, P.; Sun, H.; Wang, X.; Bautista, M. J.; Jen-La Plante, I.; Ippen, C.; Kelley, D. F. Identity of the Reversible Hole Traps in InP/ZnSe Core/Shell Quantum Dots. *J Chem Phys* **2022**, *157* (17), 174701. https://doi.org/10.1063/5.0123956.

(3) Jeon, D. Y.; Gislason, H. P.; Watkins, G. D. Optical Detection of Magnetic Resonance of the Zinc Vacancy in ZnSe via Magnetic Circular Dichroism. *Phys Rev B* **1993**, *48* (11), 7872–7883. https://doi.org/10.1103/PhysRevB.48.7872.

(4) Rong, F. C.; Barry, W. A.; Donegan, J. F.; Watkins, G. D. Vacancies, Interstitials, and Close Frenkel Pairs on the Zinc Sublattice of ZnSe. *Phys Rev B* **1996**, *54* (11), 7779–7788. https://doi.org/10.1103/PhysRevB.54.7779.

(5) Qidwai, A. A.; Woods, J. Defect Levels in Indium and Gallium Doped Zinc Selenide. *J Cryst Growth* **1982**, *59* (1–2), 217–222. https://doi.org/10.1016/0022-0248(82)90327-X.

(6) Mooney, J.; Krause, M. M.; Kambhampati, P. Connecting the Dots: The Kinetics and Thermodynamics of Hot, Cold, and Surface-Trapped Excitons in Semiconductor Nanocrystals. *The Journal of Physical Chemistry C* **2014**, *118* (14), 7730–7739. https://doi.org/10.1021/jp502102a.

(7) Mack, T. G.; Jethi, L.; Kambhampati, P. Temperature Dependence of Emission Line Widths from Semiconductor Nanocrystals Reveals Vibronic Contributions to Line Broadening Processes. *The Journal of Physical Chemistry C* **2017**, *121* (51), 28537–28545. https://doi.org/10.1021/acs.jpcc.7b09903.

(8) Krause, M. M.; Mooney, J.; Kambhampati, P. Chemical and Thermodynamic Control of the Surface of Semiconductor Nanocrystals for Designer White Light Emitters. *ACS Nano* **2013**, *7* (7), 5922–5929. https://doi.org/10.1021/nn401383t.

(9) Nguyen, A. T.; Jen-La Plante, I.; Ippen, C.; Ma, R.; Kelley, D. F. Extremely Slow Trap-Mediated Hole Relaxation in Room-Temperature InP/ZnSe/ZnS Quantum Dots. *The Journal of Physical Chemistry C* **2021**, *125* (7), 4110–4118. https://doi.org/10.1021/acs.jpcc.0c11317.

(10) Cavanaugh, P.; Sun, H.; Jen-La Plante, I.; Bautista, M. J.; Ippen, C.; Ma, R.; Kelley, A. M.; Kelley, D. F. Radiative Dynamics and Delayed Emission in Pure and Doped InP/ZnSe/ZnS Quantum Dots. *J Chem Phys* **2021**, *155* (24). https://doi.org/10.1063/5.0077327.

(11) Borcherds, P. H.; Alfrey, G. F.; Woods, A. D. B.; Saunderson, D. H. Phonon Dispersion Curves in Indium Phosphide. *Journal of Physics C: Solid State Physics* **1975**, *8* (13), 2022–2030. https://doi.org/10.1088/0022-3719/8/13/011.

(12) Hennion, B.; Moussa, F.; Pepy, G.; Kunc, K. Normal Modes of Vibrations in ZnSe. *Phys Lett A* **1971**, *36* (5), 376–378. https://doi.org/10.1016/0375-9601(71)90267-2.

(13) Bedel, E.; Landa, G.; Carles, R.; Redoules, J. P.; Renucci, J. B. Raman Investigation of the InP Lattice Dynamics. *Journal of Physics C: Solid State Physics* **1986**, *19* (10), 1471–1479. https://doi.org/10.1088/0022-3719/19/10/004.

(14) Lin, C.; Gong, K.; Kelley, D. F.; Kelley, A. M. Electron–Phonon Coupling in CdSe/CdS Core/Shell Quantum Dots. *ACS Nano* **2015**, *9* (8), 8131–8141. https://doi.org/10.1021/acsnano.5b02230.

(15) Vlaskin, V. A.; Janssen, N.; van Rijssel, J.; Beaulac, R.; Gamelin, D. R. Tunable Dual Emission in Doped Semiconductor Nanocrystals. *Nano Lett* **2010**, *10* (9), 3670–3674. https://doi.org/10.1021/nl102135k.

Supporting Information

Table 1. Characterization of Samples

QD Name	Core Diameter / nm	Shell Thickness / nm	In/P ratio	Risetime / ps	Percent Rise	Radiative lifetime / ns
S-1.0	3.0	1.0	0.97	-	0.0	32.1
S-2.0	3.0	2.0	1.04	430	3.6	31.6
S-2.51	3.05	2.51	0.99	360	2.4	28.1
NS-1.65	2.9	1.65	1.16	480	6.0	32.3
NS-1.68	2.9	1.68	1.54	355	8.2	33.5
NS-2.25	2.9	2.25	1.63	375	12.4	33.4
NS-2.01	3.04	2.01	1.52	330	8.4	32.0
CD-1.52	2.76	1.52	1.14	590	3.5	38.9
CD-1.79	2.76	1.79	1.17	660	3.8	37.8
CD-2.34	2.76	2.34	1.17	700	12	38.2
CD-2.54	2.76	2.55	1.13	60, 1040	12.0, 13.5	42.3
CD-1.31	2.9	1.31	1.26	610	1.8	33.4
CD-1.34	2.9	1.34	1.28	302	0.8	33.8
CD-1.41	2.9	1.41	1.22	-	0.0	36.3
CD-1.58	2.9	1.58	1.27	-	0.0	36.7
CD-1.59	2.9	1.59	1.35	507	1.2	36.5
CD-1.95	2.9	1.95	1.28	351	6.5	36.7
CD-2.28	2.9	2.28	1.44	89, 844	14.4, 9.1	43.0
CD-2.51	2.9	2.51	1.37	85, 1050	13.2, 9.8	43.2
CD-2.72	2.9	2.72	1.31	162, 1750	13.6, 9.0	47.7

Table 2. Dimensions and PL Decay / TA Bleach Kinetics

Sample	core diameter / nm	QD volume / nm^3	XX time / ps	XT time / ps	Fraction slow (PL)	Fraction slow (TA)	Negative trion time / ps
NSY-1.22[a]	2.32	56.5	20	115	-	0.37	130
NSO-1.85[b]	2.56	128.4	55	200	0.31	-	230
CD-1.31	2.9	88.2	66	276	0.12	0.17	290
CD-1.33	2.9	90.7	65	285	0.11	0.18	275
CD-1.41	2.9	98.4	64	290	0.19	0.3	289
CD-1.52	2.76	102.4	70	310	0.12	0.12	275
CD-1.58	2.9	116.3	69	300	0.2	0.34	287
CD-1.59	2.9	117.5	76	319	0.17	0.33	290
NS-1.6	2.9	119.2	70	315	0.17	0.34	287
NS-1.68	2.9	128.8	74	340	0.23	0.42	280
CD-1.79	2.76	133.2	72	330	0.18	0.24	275
NS-1.9A	2.9	157.9	80	355	0.14	0.32	282
NS-1.9B	2.9	157.9	75	335	0.19	0.35	290
CD-1.95	2.9	164.8	80	355	0.33	0.5	305
CD-2.04	2.76	168.4	80	360	0.31	0.49	280
NS-2.25	2.9	212.7	84	365	0.38	0.66	295
CD-2.34	2.76	215.7	90	380	0.33	0.54	310
CD-2.28	2.9	218.3	85	365	0.35	0.56	290
CD-2.54	2.76	253.1	95	385	0.41	0.6	320
CD-2.51	2.9	260.4	90	370	0.43	0.65	320
CD-2.72	2.9	305.1	100	380	0.49	0.71	330

[a] the yellow QD photon cross section was too small to obtain PL biexciton kinetics.
[b] the orange QDs are insufficiently stable to obtain reliable TA kinetics.

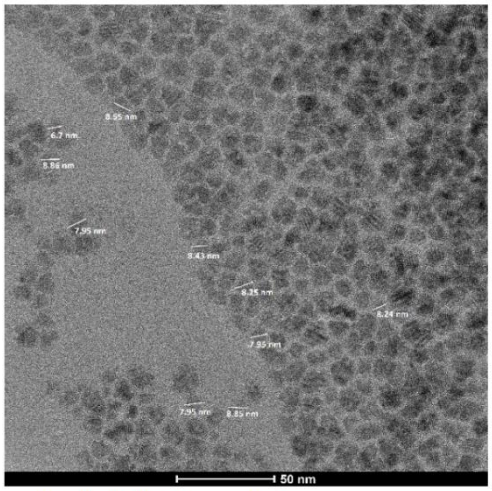

Figure S1 A: CD 2.72 W/O HDT. Average Size 8.17 ± 0.38 nm

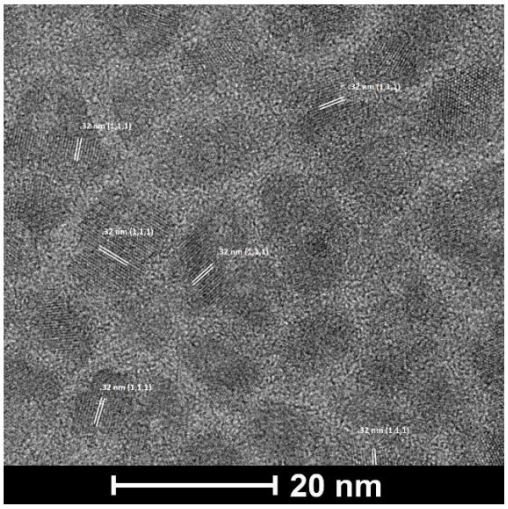

Figure S1 B: CD 2.72 W/O HDT Lattice Fringes

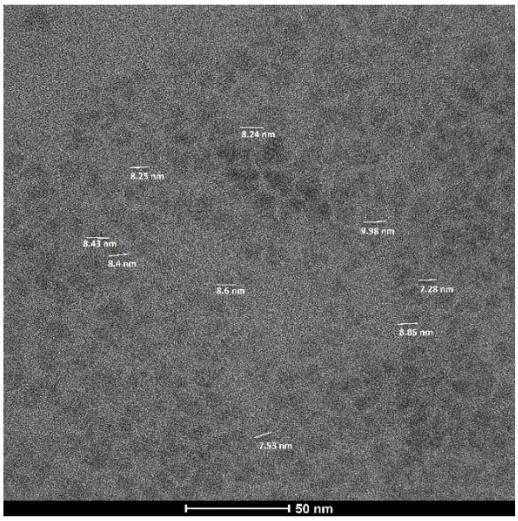

Figure S1 C: CD 2.72 W/ HDT. Average Size 8.4 ± 0.77 nm

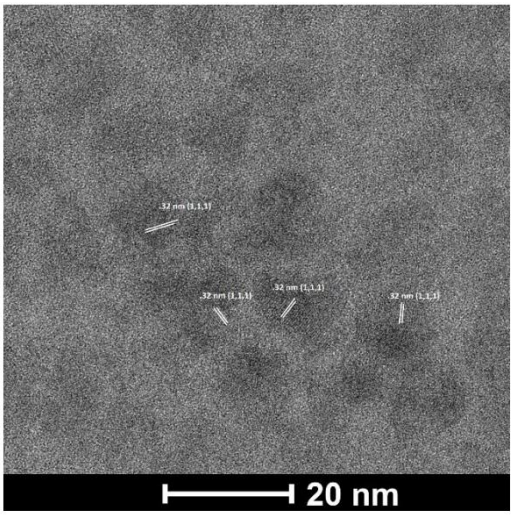

Figure S1 D: CD 2.72 W/ HDT Lattice Fringes

Figure S1: TEM images of CD 2.72 showing size distributions and lattice fring**es.**